

**Lift Distributions on Low Aspect Ratio Wings at
Low Reynolds Numbers**

by

Sagar Sanjeev Sathaye

A Thesis

Submitted to the Faculty of

WORCESTER POLYTECHNIC INSTITUTE

in partial fulfillment of the requirements for the

Degree of Master of Science

in

Mechanical Engineering

by

May 2004

Approved:

Professor David J Olinger, Thesis Advisor

Professor Hamid Johari, Committee Member

Professor William Durgin, Committee Member

Professor John Sullivan, Graduate Committee Representative

Abstract

The aerodynamic performance of low aspect ratio wings at low Reynolds numbers applicable to micro air vehicle design was studied in this thesis. There is an overall lack of data for this low Reynolds number range, particularly concerning details of local flow behavior along the span. Experiments were conducted to measure the local pressure distributions on a wing at various spanwise locations in a Reynolds number range $3 \times 10^4 < Re < 9 \times 10^4$. The model wing consisted of numerous wing sections and had a rectangular planform with NACA0012 airfoil shape with aspect ratio of one. One wing section, with pressure ports at various chordwise locations, was placed at different spanwise locations on a wing to effectively obtain the local pressure information. Integration of the pressure distributions yielded the local lift coefficients. Comparison of the local lift distributions to optimal elliptic lift distribution was conducted. This comparison showed a sharply peaked lift distribution near the wing tip resulting in a drastic deviation from the equivalent elliptic lift distributions predicted by the finite wing theory. The local lift distributions were further analyzed to determine the total lift coefficients vs angle of attack curves, span efficiency factors and the induced drag coefficients. Measured span efficiency factors, which were lower than predictions of the elliptic wing theory, can be understood by studying deviations of measured lift from the elliptic lift distribution. We conclude that elliptic wing theory is not sufficient to predict these aerodynamic performance parameters. Overall, these local measurements provided a better understanding of the low Reynolds number aerodynamics of the low aspect ratio wings.

Acknowledgements

I would like to thank my advisor Professor Olinger for all the guidance, kindness and belonging he has given me over the last two years. He had envisaged the idea of making a wing in sections and using it for pressure measurements in such an innovative and simple way. I am glad to be a part of his imagination becoming a reality. I would also like to thank Professor Bill Weir here for his continued support and encouragement and his fabulous participation in making the wing. Right from day one Professor Weir's interest and involvement in the manufacturing of the wing was incredible. I sincerely thank Professor Olinger and Professor Weir for successful completion of my research. I would also like to thank Professor Johari for all the discussions and timely advice over the course of this research. I also thank Professor Durgin and Professor Sullivan for serving as my defense committee members.

I thank Abhijeet, Siju, Elham, Gana and Ian for their support and affection without whom the last two years wouldn't have been so enjoying and fulfilling. I thank Ryan and Shang for sharing all the hilarious moments, which made my stay at WPI a lot comfortable. I thank Jim Johnston whom I bothered till the last day of my research, without ever being denied a helping hand.

Last and definitely not the least I am really grateful to my parents who have been my inspiration and strength over all these years and Mugdha and Sarang for being so supportive and encouraging, and being there for me when I needed.

To Aai – Baba

Table of Contents:

List of Figures	iii
List of Tables	v
Nomenclature	vi
1. Introduction	1
1.1 Background.....	1
1.2 Previous work.....	3
1.3 Thesis Objectives.....	8
2. Methods	10
2.1 Theory behind the analysis.....	10
2.2 Experimental set-up.....	16
2.2.1 Wind tunnel.....	16
2.2.2 Pressure Transducer.....	17
2.2.3 Wing Model.....	17
2.2.4 Sting arm/ Angle of attack control mechanism.....	23
2.2.5 Lift measurement set-up using force balance.....	23
2.3 Tygon tube out-gassing.....	24
2.4 Velocity Distribution across wind tunnel.....	25
2.5 Experimental Procedure.....	27
2.6 Error analysis.....	28
3. Results	29
3.1 Local Pressure measurements.....	29
3.2 Spanwise Lift Distributions.....	47

3.3 Fourier Coefficients.....	59
3.4 Span efficiency factor.....	63
3.5 Lift coefficient curve vs angle of attack.....	68
3.6 Induced drag coefficients.....	73
4. Conclusions.....	77
5. Suggestions for future work.....	81
References.....	84
Appendix A Pressure distributions.....	86
Appendix B MATLAB Codes.....	109
Appendix C Fourier Coefficients.....	114
Appendix D Sample Error calculation.....	117

List of Figures:

<u>Figure 2.1</u> Exploded view of the low aspect ratio test wing (NACA0012).....	19
<u>Figure 2.2</u> Numbering scheme for spanwise locations for the pressure section.....	19
<u>Figure 2.3</u> Chord wise locations of ports on the pressure section.....	20
<u>Figure 2.4</u> Numbering scheme for the ports.....	21
<u>Figure 2.5</u> Experimental set-up (schematic).....	22
<u>Figure 2.6</u> Velocity distributions across wind tunnel.....	26
<u>Figure 3.1</u> C_p vs x/c plots for $Re = 35966$, $\alpha = 15^\circ$	34
<u>Figure 3.2</u> C_p vs x/c plots for $Re = 35966$, $\alpha = 6^\circ$	35
<u>Figure 3.3</u> Flow visualization from Torres and Mueller [17]	36
<u>Figure 3.4</u> C_p vs x/c plots for $Re = 30218$, $\alpha = 15^\circ$	37
<u>Figure 3.5</u> C_p vs x/c plots for $Re = 30218$, $\alpha = 6^\circ$	38
<u>Figure 3.6</u> C_p vs x/c plots for $Re = 84122$, $\alpha = 15^\circ$	39
<u>Figure 3.7</u> C_p vs x/c plots for $Re = 84122$, $\alpha = 6^\circ$	40
<u>Figure 3.8</u> C_p vs x/c plots for $Re = 49345$, $\alpha = 15^\circ$	41
<u>Figure 3.9</u> C_p vs x/c plots for $Re = 49345$, $\alpha = 6^\circ$	41
<u>Figure 3.10</u> Effect of variation of α on C_p distribution for $Re = 43615$	43
<u>Figure 3.11</u> Effect of variation of Re variation on C_p distribution for $\alpha = 6^\circ$	44
<u>Figure 3.12</u> Effect of variation of Re variation on C_p distribution for $\alpha = 15^\circ$	45
<u>Figure 3.13</u> C_p vs x/c plots at $\alpha = 0^\circ$ for Pos 1.....	46
<u>Figure 3.14</u> Local lift coefficient distribution at $\alpha = 15^\circ$	51
<u>Figure 3.15</u> Local lift coefficient distribution at $\alpha = 6^\circ$	52

<u>Figure 3.16</u> Approximate Wing tip vortex core location	53
<u>Figure 3.17</u> Local lift distribution at $\alpha = 15^\circ$	54
<u>Figure 3.18</u> Local lift distribution at $\alpha = 6^\circ$	55
<u>Figure 3.19</u> Normalized lift distributions for Rectangular wings with varying AR.....	56
<u>Figure 3.20</u> Local lift coefficient distribution for various angles of attacks.....	57
<u>Figure 3.21</u> Local lift coefficient distribution for $Re = 30218$ at $\alpha = 15^\circ$	58
<u>Figure 3.22</u> Span efficiency factor vs No. of coefficients used for analysis.....	62
<u>Figure 3.23</u> Variation of span efficiency factor with Reynolds number.....	65
<u>Figure 3.24</u> Variation of span efficiency factor with angle of attack.....	66
<u>Figure 3.25</u> Spanwise lift distribution for $Re = 43615$	67
<u>Figure 3.26</u> Lift vs angle of attack curve at $Re = 43615$	71
<u>Figure 3.27</u> Lift vs angle of attack curve at $Re = 84122$	72
<u>Figure 3.28</u> Induced drag coefficients with varying α	75
<u>Figure 3.29</u> Induced drag coefficients with varying Re	76
<u>Figure 5.1</u> Adjusted chord distribution.....	83

List of tables:

Table 2.1: Spanwise distances from the wing tip for pressure section.....20

Table 2.2: Chordwise locations of ports as percent chord (x/c).....21

Table 2.3: Experimental matrix.....27

Nomenclature:

AR = aspect ratio of the wing.

α = angle of attack

A = Axial Force

b = span of the wing.

c = chord length of the wing.

c_a = local axial coefficient.

c_d = local drag coefficient

C_D = total drag coefficient.

C_{D_0} = parasitic Drag coefficient.

C_{D_i} = induced drag coefficient

c_f = shear stress coefficient.

c_l = local lift coefficient

C_L = total lift coefficient.

c_n = local normal coefficient.

C_p = pressure coefficient.

D = Drag.

e = span efficiency factor.

Γ = circulation

l = lower surface quantity

L = lift.

L' = lift per unit span (local lift)

μ = Absolute Viscosity of air (1.79×10^{-5})

N = Normal force.

P = pressure.

P_∞ = static pressure.

q_∞ = dynamic pressure.

Re = Reynolds number.

ρ_∞ = free stream density (1.19 kg/m^3)

τ = shear stress distribution.

u = upper surface quantity

V_∞ = free stream velocity.

x = co-ordinate axes along the wing chord.

y = co-ordinate axes along the wing span.

1. Introduction

1.1 Background

Aircraft design has been of interest for over a century. Military and civil aircrafts, which fly at Reynolds numbers of 10^6 and above, have usually been studied. The flow behavior over airfoils in this range of Reynolds number is well understood.

The aerodynamics in the Reynolds number range below that of commercial aircraft has gained attention from the research community over the last few years. These Micro Air Vehicles (MAV's) have a variety of potential applications ranging from military and civil missions to use in planetary explorations. These may include surveillance missions, detection of chemical or biological agents, placement of acoustic sensors on the outside of a building during a hostage rescue and other search and rescue operations. The advancement in micro-fabrication techniques and miniaturization of electronics is the main driving force behind this development.

Micro-air vehicles (MAV's) are the smallest class of uninhabited air vehicles (UAV's). Current MAV's generally have maximum dimensions of less than 25 cm , fly at approximately 10 m/s , and have low aspect ratios $AR \cong 1$ (where $AR = \text{wing span/wing chord}$), yielding Reynolds numbers of $10^5 < Re < 10^6$. The final aim for these projects is to develop an MAV of the size less than 8 cm , total weight less than 30 g and flying at the speeds of less than 10 m/s . Future MAV's are expected to decrease in size by an additional order of magnitude compare to current models, placing them in the Reynolds number range of the work in this thesis.

The function of any wing is to generate lift. There is a drag associated with this lift generation know as the induced drag, is in addition to the parasitic drag produced on

the wing. The aerodynamic effectiveness of an airfoil is judged by the lift –drag ratio. This ratio decreases dramatically, at low Reynolds numbers and results in deterioration of performance of the airfoils. Other investigators have concentrated on reducing the drag and improving the lift-drag ratio of MAV's. This thesis has the same overall goal and should be helpful in providing some important information about the aerodynamics of the flow in the Low Reynolds number range of $10^4 < Re < 10^6$.

Birds and insects are found to fly in this range of Reynolds numbers. The study of aerodynamics of the flow over the wing of these birds and insects is another aspect of MAV development. As MAV's become smaller and smaller, they may need to mimic certain aspects of bird and insect flight. Typical features of bird wings such as notches on the trailing edges and cambered airfoil shapes have been studied by biologists as well as aerodynamicists [21].

In the next section we will discuss observations and conclusions made so far by various researchers in this low Reynolds number regime. This is not a complete summary but a brief review of the studies carried out relevant to the present work. The main emphasis is on the aerodynamic flow phenomenon occurring over the low aspect ratio wings at low Reynolds number. Section 1.3 will outline the scope of work in the thesis and other objectives of the study.

1.2 Previous work

Very limited aerodynamic data exists for airfoils and low aspect ratio wings in the Reynolds number 10^4 - 10^5 range. Previous numerical simulations have often focused on two-dimensional airfoil flow and primarily concentrated on design and analysis of new airfoil shapes for these low aspect ratio wings. (Kunz and Kroo [1] and Selig [2]).

However, the aerodynamics of the flow over MAV wings is inherently three-dimensional and is dominated by wingtip vortices. The three-dimensional nature of the flowfield along the wingspan in the case of low aspect ratio wings at low Reynolds numbers has remained largely unstudied in experiments. Monttinen et.al. [3] have solved the Navier Stokes equations for low chord Reynolds number flows. They have used finite element approximations and unstructured meshes with adaptive refinement to model the flow over various airfoils at Reynolds numbers as low as 4×10^3 . Although they have tried to model three-dimensional flows and the extension of their fluid solver to three dimensions has been straightforward, experimental verification of these results has not been conducted

The flow over these wings is laminar and hence viscous effects become a governing factor. A very complex phenomenon takes place here within a short distance on the MAV wing. Carmichael [4] has explained this phenomenon for various flow regimes for the low Reynolds number airfoils in details. For Reynolds number range of $10^3 < Re < 10^4$, flow is found to be laminar in the boundary layer and it is very difficult to cause transition to turbulent flow. It is very difficult to generate turbulent boundary layers artificially. The boundary layer remains laminar even in the range $10^4 < Re <$

3×10^4 . But the lift coefficients are of the order of 0.5 or less. Use of artificial methods to generate higher lift coefficients results in a separated laminar boundary layer without reattachment. Apparently, in the range $3 \times 10^4 < Re < 7 \times 10^4$ the laminar separation with transition to turbulent flow is observed. But for a Reynolds number below 5×10^4 , laminar separation does not transition in time, to turbulent flow for the boundary layer time to reattach. A laminar separation bubble is found on the upper surface of most of the airfoils at Reynolds numbers above 5×10^4 . It is known that these bubbles become larger with reducing Reynolds numbers and as a result causes a rapid deterioration in the performance. Typically, adding so-called 'turbulators' can artificially control this laminar separation bubble and transition. These include wires, tape strips, grooves, bleed through holes and so on. However, the appropriate positions and practical effects of these turbulators have not yet been studied in details. At a Reynolds number higher than 7×10^4 a laminar flow can be obtained but the separation bubble may still be present for a particular airfoil. This flow separation is the main reasons for stalling of the wings. Gad-el-Hak [5] has further explained the aerodynamics behind the separation bubble formation on a wing in detail. The study presented in this thesis concentrates on the range $3 \times 10^4 < Re < 9 \times 10^4$, which encompasses the region detailed in Carmichael [4]. Carmichael discusses the flow over 2-D airfoils, however 3-D effects such as the wing tip vortices dominate the flow over a finite MAV wing, which drastically alters the flow over the wing.

McCullough and Gault [6] have established that the airfoil stall could be classified through three types of stall, trailing edge stall, leading edge stall and thin airfoil stall. The trailing edge stall results because of movement of the turbulent boundary layer

separation point forward from the trailing edge with increasing angle of attack. Leading edge stall involves flow separation near the leading edge without subsequent reattachment.

This abrupt separation is caused due to bursting of the separation bubble at stall and results in sharp reduction in the lift. The thin airfoil stall is primarily due to flow separation at the leading edge with reattachment, which progressively moves downstream with increasing angle of attack. Their observations suggest that the stall can be a combination of any or all of these stall types. Broeren and Bragg [7] have carried out experiments on various airfoil shapes at $Re = 3 \times 10^5$ to study the unsteady effect in these stall types. They observed that the laminar separation bubble was a common feature in the airfoil flowfields for both, thin airfoil stall and trailing edge separation stall. The elimination of the separation bubble caused a significant reduction in the unsteady behavior of lift near the stall.

Studies on low aspect ratio wings have often focused on theoretical treatments at higher Reynolds numbers [8], [9] and delta wing shapes [10]. Delta wings used in modern fighter aircrafts have been studied extensively. Although delta wings are normally studied at relatively higher aspect ratios ($AR \approx 2$ to 3) and higher Reynolds numbers, studies suggest that delta wings are also prone to separation from the outboard leading edge and have lift distributions strongly deviating from the theoretical predictions [11].

The study by Hoerner [12], [13] indicates that the lift on wings of $AR=1$ or less is composed of two sources, linear and non-linear. The linear part of the lift is similar to that observed in high AR wings associated with the circulation around the airfoil. The

non-linear part of the lift is due to formation of low-pressure cells on the wing's top surfaces by the tip vortices, such as that observed in delta wings at high angle of attack. A pair of wing tip vortices is formed above and parallel to the lateral edges. Two different schemes have been suggested by various authors [14], [15], as a reason behind this non-linear lift. One suggests that the lateral edges of a small aspect ratio (rectangular) wing are assumed to have an effect similar to end plates having a height proportional to the angle of attack. The other proposes that the size of the fluid stream tube deflected by the wing is increased by a component, which is proportional to the angle of attack. Study further predicts that this non-linear part of the lift is responsible for higher stall angles for the low AR wings.

Mueller and Pelletier [16] have performed experiments on various thin flat/cambered plate, low aspect ratio rectangular wings in a Reynolds number range of $6 \times 10^4 < Re < 1.7 \times 10^5$ to investigate the effects of camber, trailing edge geometry, leading edge geometry on the aerodynamic performance of those airfoils. They have carried out experiments on thin airfoil wings of aspect ratios $0.5 < AR < 3$. Their observations suggest that with reducing aspect ratio the angle of attack for stall increased. They also clearly observed a thin separation region on the suction surface near the trailing edge at low angles of attack during flow visualization carried out with hydrogen bubbles in a water tunnel in a similar range of Reynolds numbers. This separation region increased to more than 50% of the chord after an angle of 8° . They have also discussed cambered airfoils in detail and conclude that cambered airfoils (with 4% camber) offer better aerodynamic performance than a flat-plate wing for a given Reynolds number and aspect ratio.

Torres and Mueller [17] have presented their observations on various wing planform shapes in the range $7 \times 10^4 < Re < 1.4 \times 10^4$. Although these experiments were carried out at Reynolds number lower than used by Hoerner [12], [13] the aerodynamic theory still holds. Their study included wind tunnel experiments as well as flow visualizations which further supports the theory predicted by Hoerner [12], [13] and McCullough et al. [6]. They clearly observed a separation bubble, typical in low Reynolds number flows. They conclude that a laminar free-shear layer forms and is highly unstable if the Reynolds number exceeds some critical value. Small perturbations in the flow cause transition to turbulent flow in this layer. This turbulent flow energizes the flow near the airfoil surface and sometimes reattaches as turbulent boundary layer. Their observations show the width of this separation bubble ranges to be from a small percent of the chord to 30% of the chord.

This separation bubble was limited to inner sections of the wing as the wing tip vortices energize the flow and the separation is eliminated near the wing tip. Their wind tunnel measurements along with some numerical simulations for lift and drag suggest that the angle of attack for stall increases as aspect ratio becomes smaller. The lift curve becomes increasingly nonlinear with reduction in aspect ratio. They also observed span efficiency factors, e defined by

$$C_D = C_{D_0} + \frac{C_L^2}{\pi e AR} \quad (1)$$

in the range of $0.6 < e < 0.7$ for Re between 7×10^4 and 1×10^5 at aspect ratios $AR < 2$. These e values are lower than typical values found on high aspect ratio wings at high Re, which are normally between 0.8-0.9.

1.3 Thesis Objectives

Previous studies have essentially concentrated on understanding the overall aerodynamic performance of low AR wing shapes, or determining optimum airfoil shapes at low Reynolds numbers so as to improve the wing performance in MAV designs. As a result there is a lack of any experimental data for local behavior of the flow over these wings. We seek to measure spanwise pressure and lift distributions in order to understand the local behavior of the flow on the wing. Tests are performed on a low aspect ratio rectangular wing ($AR = 1$) in the Reynolds number range $2.5 \times 10^4 < Re < 8.5 \times 10^4$ at various angles of attack. The local lift distribution is obtained through surface pressure measurements at various locations along the span of the wing. The pressure distribution along the chord at each spanwise location is studied to understand the local aerodynamics in these highly three-dimensional flows. The pressure data is analyzed to validate the separation phenomenon observed in earlier studies. Prandtl's lifting line theory forms the basis of most of the aerodynamic research carried out on any wing or airfoil. To the best of our knowledge, a specially modified theory hasn't been suggested to date for the optimum lift distribution over low Aspect Ratio ($AR = 1$) wings at low Reynolds numbers. Hence the analysis in this thesis is based on Prandtl's lifting line theory. An overall goal of the present study is to determine if this theory can accurately predict total lift coefficients, local lift distribution and induced drag on low AR wings at low Reynolds numbers. The span efficiency factor, introduced before, is dependent on the spanwise circulation (lift) distribution over the wing. A general lift distribution on a wing can be expressed in terms of a Fourier sine series. The Fourier coefficients for this series can yield the span efficiency factor, 'e', if relations from Prandtl's lifting line theory are

applied. This relation is discussed in detail in Section 2.1. Prandtl's lifting line theory shows that the value of 'e' for an elliptic lift distribution is 1. With any deviation of the lift from this elliptic shape the span efficiency tends to reduce. We seek to determine the Fourier coefficients for the measured lift distributions and then obtain the span efficiency factors. The span efficiency factor is directly related to generated induced drag through Prandtl's lifting line theory. We also seek to determine the physical cause behind lower values of 'e' observed by Mueller [17] through careful study of the measured spanwise lift distributions. We will also undertake an independent study of lift on low AR wings using force balance methods in order to further confirm our findings. Our study will also address the issue of whether an optimal planform shapes for MAV wings can be designed based on the observed local lift distributions. The measurements in this study could also eventually prove useful in understanding loadings and deformations on low AR wings with possible application to future flapping-wing MAV's if certain quasi-static assumptions are applied.

The thesis is organized as follows. In chapter 2, we discuss the theory used in the study. We will also discuss here, details of the experimental set-up for pressure and the lift measurements. In chapter 3 we discuss the results obtained during the experiments. This includes discussion of the pressure distributions over the wing at various Reynolds numbers and angles of attacks, local lift and lift coefficient distributions, lift curve slopes at various Reynolds numbers and the span efficiency factor at various Reynolds numbers and angles of attacks. In chapter 4 we describe the conclusions made on the basis of results obtained during this research. Chapter 5 describes the future work that needs to be done to further understand the low Reynolds number flow regime.

2. Methods

In this chapter we first review the aerodynamic theory used in the present study. The focus is mainly on the pressure distribution over an airfoil, finite wing theory, Prandtl's lifting line theory, which leads to discussion of induced drag and span efficiency factor. We then discuss the experimental set up for the two types of experiments carried out, pressure measurements and force balance measurements. Fabrication of the model wing, pressure measurement set-up and instrumentation issues are then discussed. This chapter also discusses issues related to experimental error such as velocity variations in the test section and pressure tubing out-gassing. A brief summary of the experimental procedure is discussed at the end of this chapter.

2.1 Theory behind the analysis

Application of momentum conservation laws shows that the forces and moments on an airfoil or a wing are due to two sources:

1. Pressure Distribution on the surface of the body.
2. Shear stress distribution over the surface of the body.

The pressure forces act normal to the surface of the airfoil whereas the shear stress acts tangential to the surface of the airfoil. The integration of these two distributions over the surface of the airfoil yields a resultant force and a moment. This resultant force can be divided into two components, one perpendicular to the chord line, the normal force (N) and other parallel to the chord line, the axial force (A). The relation between these forces and the pressure and stress distribution in terms of non-dimensional coefficients is given as:

$$c_n = \frac{1}{c} \left[\int_0^c (C_{p,l} - C_{p,u}) dx + \int_0^c (c_{f,u} \frac{dy_u}{dx} + c_{f,l} \frac{dy_l}{dx}) dx \right] \quad (2)$$

$$c_a = \frac{1}{c} \left[\int_0^c (C_{p,u} \frac{dy_u}{dx} - C_{p,l} \frac{dy_l}{dx}) dx + \left(\int_0^c (c_{f,u} - c_{f,l}) dx \right) \right] \quad (3)$$

The suffixes u and l indicate the upper and lower surface respectively.

The pressure coefficient and the shear stress coefficients are given as:

$$C_p = \frac{P - P_\infty}{q_\infty} \quad (4)$$

$$c_f = \frac{\tau}{q_\infty} \quad (5)$$

The resultant force can be split up into two other components, Lift (L) which is in the direction perpendicular to the flow direction and drag (D) in the direction of the free stream velocity. The geometric angle of attack (α) for the airfoil is the angle made by the chord line with the flow direction. These various components of the resultant force are related by:

$$L = N \cos \alpha - A \sin \alpha \quad (6)$$

$$D = N \sin \alpha + A \cos \alpha \quad (7)$$

This leads us to the following non-dimensional coefficients.

$$c_l = c_n \cos \alpha - c_a \sin \alpha \quad (8)$$

$$c_d = c_n \sin \alpha + c_a \cos \alpha \quad (9)$$

For small angles of attack the lift coefficient can be approximated as equal to the normal coefficient. So from equation (2) and (8) we have

$$c_l = \left(-\frac{1}{c} \int_0^c (C_{p,u} - C_{p,l}) dx \right) \cos \alpha \quad (10)$$

This is only if $c_a \ll c_n$, e.g. viscous shear stresses are considered negligible. The average value of c_a based on a laminar flow assumption was of the order of 1-2% of c_n in the Reynolds number range under consideration in this study. Hence neglecting the viscous shear stress has an insignificant effect on the lift coefficient. This equation shows that if the pressure distribution on the surface of the airfoil is measured the lift coefficient can be determined. The observations made in the thesis are based on this assumption.

The parameter c_l is a local (or two-dimensional) lift coefficient, which may vary along the span of the airfoil so that $c_l(z)$. To obtain this lift distribution, pressure measurements were carried out at various spanwise locations on an airfoil. Measurements were made with 22 different pressure ports with one port at the leading edge, 11 on the upper surface and 10 on the lower surface of the airfoil.

Figure 2.4 gives the numbering scheme for the pressure ports. The construction of the airfoil and the details about these pressure ports will be discussed in Section 2.6. The reference pressure for these pressure measurements was the static pressure in the wind tunnel. The dynamic pressure was measured using the same pressure transducer (explained in Section 2.8). Using equation (4) and the pressures recorded, pressure coefficients at various chord wise locations were obtained. Using a modified version of equation (8) the local lift coefficients were calculated. The equation used is based on a normalized chord length and given as follows:

$$c_l = \left(\int_0^1 (C_{pl} - C_{pu}) d\left(\frac{x}{c}\right) \right) \cos \alpha \quad (11)$$

The set up allowed pressure measurements at various spanwise locations leading to measurement of lift coefficients at those different locations, i.e. the spanwise lift coefficient distribution.

The spanwise lift coefficients can be converted to a local lift distribution using the relation:

$$L' = \frac{1}{2} \rho_{\infty} V_{\infty}^2 c c_l \quad (12)$$

where L' is the lift per unit span.

The Kutta-Joukowski relates the circulation and the lift generated as follows:

$$\Gamma = \frac{L'}{\rho_{\infty} V_{\infty}} \quad (13)$$

It is well known that a general circulation distribution along any arbitrary finite wing can be approximated using a Fourier Sine series as follows:

$$\Gamma(\theta) = 2bV_{\infty} \sum_1^N A_n \sin n\theta \quad (14)$$

Here θ is a transformation variable given by

$$\theta = \cos^{-1} \left(-\frac{2z}{b} \right) \quad (15)$$

with $0 \leq \theta \leq \pi$.

This acts as a new transformed co-ordinate system that is used to build up the circulation distribution $\Gamma(\theta)$. The coefficients A_n 's are the Fourier coefficients. By applying equations (11) - (15) to our pressure measurements, we can obtain the circulation distribution in equation (14) at various spanwise locations along the transformed co-ordinates. Then the A_n 's are the only unknowns in the equation (14). Depending on the number of θ co-ordinates used, say N , we will have N independent equations and N unknowns. So equation (14) becomes a system of linear equations to be solved for those N unknowns.

The Fourier coefficients are determined from the circulation distribution obtained through pressure measurements. The total lift coefficient can be obtained from the local lift coefficient distribution as:

$$C_L = \int_{-b/2}^{b/2} c_l(z) dz \quad (16)$$

This total lift coefficient is also based on the leading coefficient A_1 of A_n . The relation is given as:

$$C_L = A_1 \pi AR \quad (17)$$

Further the induced drag produced on the wing is also a function of these Fourier coefficients and is given as

$$C_{D,i} = \pi AR A_1^2 \left[1 + \sum_2^N n \left(\frac{A_n}{A_1} \right)^2 \right] \quad (18)$$

This can be further modified using equation (17) to give:

$$C_{D,i} = \frac{C_L^2}{\pi e AR} \quad (19)$$

The coefficient 'e' in this equation is known as the span efficiency factor, which was introduced earlier in section 1. This factor 'e' is hence given as

$$e = \frac{1}{\left[1 + \left(\sum_2^N n \left(\frac{A_n}{A_1} \right)^2 \right) \right]} \quad (20)$$

The span efficiency factor is a measure of the induced drag, as the span efficiency factor decreases the induced drag increases. The span efficiency factor $e = 1$ for an elliptic lift distribution. For a general lift distribution this number is lower. Prandtl's lifting line theory applied to rectangular wings with $AR \rightarrow 0$ gives an elliptic lift distribution. This

results in a span efficiency factor very close to 1 ($e = 0.9969$). These equations form the basis of the assumptions made in this research.

Further more the lift curve slope for an elliptic wing is also based on the Fourier coefficients. This is given as:

$$\frac{dC_L}{d\alpha} = a = \frac{a_0}{1 + \frac{a_0}{\pi \cdot AR}} \quad (21)$$

where a = lift curve slope for a elliptic planform wing

$$a_0 = \text{lift curve slope for a 2-D airfoil} = 2 \cdot \pi$$

This equation gets modified for a finite wing with rectangular planform as follows:

$$a = \frac{a_0}{1 + \frac{a_0}{\pi \cdot AR} \cdot (1 + \tau)} \quad (22)$$

The additional term τ is a function of the first coefficient of the Fourier sine series A_1 and is related through

$$(1 + \tau) = \frac{4 \cdot AR}{a_0} \cdot \left(\frac{4 \cdot AR \cdot \alpha}{a_0 \cdot A_1} - \frac{\pi}{4} \right) \quad (23)$$

where α = angle of attack under consideration.

Hence by determining the leading term of the Fourier coefficients A_1 the lift curve slope for a wing with rectangular planform can be determined. For an elliptic wing with $AR = 1$, $a = (2 \cdot \pi / 3)$.

The fundamental equation of Prandtl's lifting line theory, which gives the relation between the geometric angle of attack, the induced angle of attack and the effective angle of attack, is as follows:

$$\alpha(\theta_o) = \frac{2b}{\pi c(\theta_o)} \sum_1^n A_n \cos n\theta_o + \alpha_{L=0}(\theta_o) + \sum_1^n nA_n \frac{\sin n\theta_o}{\sin \theta_o} \quad (24)$$

where α = geometric angle of attack.

This equation was used to calculate the lift distribution for a rectangular wing with varying aspect ratios. This issue is discussed later in Section 3. Equations (1)-(22) and (24) are from Anderson [25] and equation (23) from Glauert [26].

Analysis required for the experiments was carried out using MATLAB software. The equations (11) - (23) formed the basic framework of all this analysis. Typically, built-in solvers and programs from MATLAB were used to avoid uncertainties in programming. The MATLAB codes are attached in [Appendix B](#).

2.2 Experimental set up

2.2.1 Wind tunnel

Measurements were performed in WPI's closed circuit wind tunnel. This is a low speed re-circulating wind tunnel with a contraction ratio of 6:1 with test section dimensions 61 cm (width) x 61 (height) cm x 240 (length) cm. The free stream velocity in the test section can be varied from 1 m/s to 55 m/s. This corresponds to a Reynolds number of 1.2×10^4 to 6.2×10^5 . The free stream velocity was determined by measuring the dynamic pressure in the wind tunnel using a pressure transducer, explained later in section 2.2.2.

The turbulence intensity in the wind tunnel is about 0.8 % in the range of velocities considered for the measurement. The free stream turbulence measurements are from Popp [22]. The wind tunnel is equipped with a copper tubing water-cooled heat exchanger. The

temperature of the air inside the wind tunnel was maintained at $73^{\circ} F$ for all the measurements to avoid inaccuracies due to temperature variations.

2.2.2 Pressure Transducer

A Setra Make C264, ± 0.1 inches of water bidirectional pressure transducer was used for all the measurements. The transducer was connected to a Setra make Datum 2001 display, which displayed the pressure in inches of water. It had an accuracy of ± 0.25 % FS or 0.0005 in of Water. The transducer calibration was verified against an inclined manometer in the 0.1 ” range.

2.2.3. Wing Model

All tests were carried out on a blunt-end rectangular wing with $AR = 1$ with a NACA 0012 airfoil shape. A NACA 0012 shape was chosen because substantial information exists on its aerodynamic performance at high Reynolds numbers. The 12% thickness of the airfoil also facilitated the internal pressure tubing. Future study should extend the present work to other optimized airfoil shapes at these lower Reynolds numbers. The span and chord of the wing were both 20.32 cm in length. The wing was fabricated in the WPI HAAS CNC facility out of PVC plastic. The accuracy of the manufacturing was maintained at about $\pm .00127$ cm (± 0.005 ”). The wing was built in 1.27 cm thick sections each with identical airfoil sections. The final wing consisted of 14 of these 1.27 cm thick sections and a 2.54 cm central section (Fig.2.1).

The wing was constructed in sections to achieve the purpose of measuring local pressure distributions along the span of the wing. These sections were assembled together with a $\frac{1}{4}$ ” threaded rod with nuts on both the ends to tightly hold all the sections

and the central section together. Two $1/8$ " guiding dowell pins on each section aligned each section with the one next to it.

Twenty-two surface pressure taps, each 0.1 cm in diameter, were drilled on one of the sections (hereafter, referred to as the pressure section). The data points in Fig. 2.3 show the locations of the pressure taps along the chord line on the pressure section. One of these ports was at the leading edge, 11 ports were on the upper surface and 10 were on the lower surface. Fig. 2.4 explains the numbering scheme for the ports on the pressure section. The positions 1-7 shown in (Fig.2.2) indicate various spanwise locations of the pressure section used to measure the local pressure distributions. Table 2.1 presents the spanwise distances of these positions from the wing tip. It was assumed that the measured spanwise pressure distributions and resulting lift distributions are symmetric about the wing centerline located at the central span section. Therefore pressure distributions were measured over half of the wing span only.

The schematic for the overall experimental set-up is shown in Fig. 2.5. Internal holes, 0.1 cm in diameter, were drilled through the remaining 6 sections. Tygon tubing passed through these holes carried the pressure information from the pressure taps to the central section. The tygon tubing eliminated the possibility of any leakage between wing sections. Tygon tubing used was of 0.1 cm ID and 0.3175 cm in OD. The tubing passed out of the central section through an opening on the lower surface, and then was guided along the sting balance out of the wind tunnel. Care was taken to ensure the effect of tube bundle on the flowfield around the wing was minimized. The 22 tubes were connected to the pressure transducer through a pressure tube selector mechanism. Only one tube at a time would connect to the transducer.

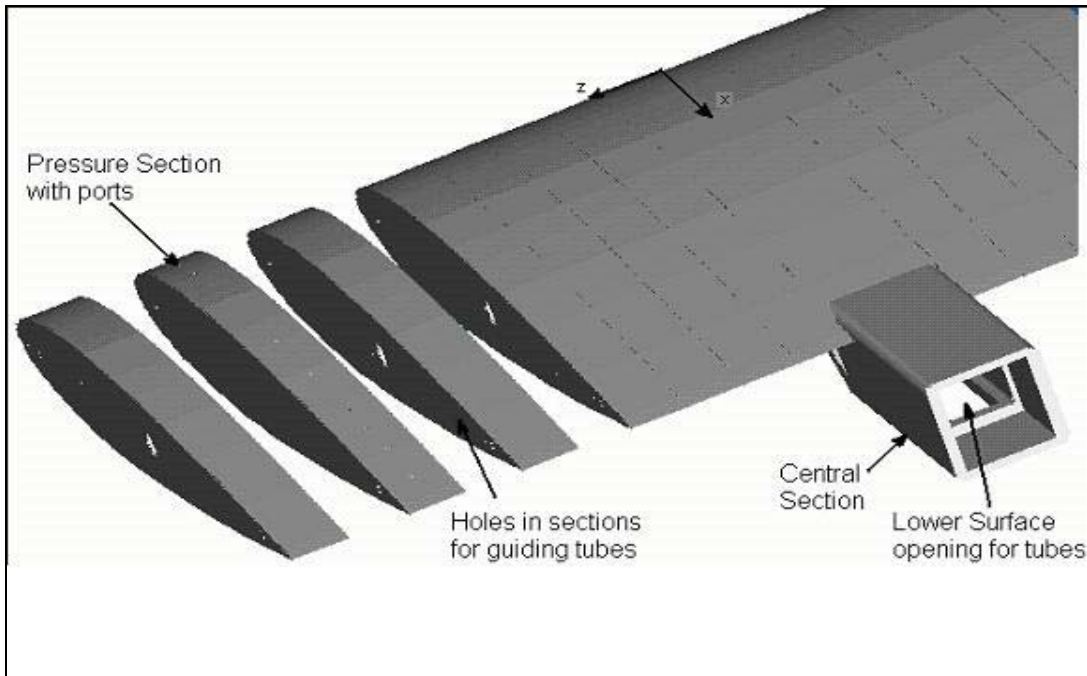


Fig. 2.1 Exploded view of the low aspect ratio wing (NACA 0012)

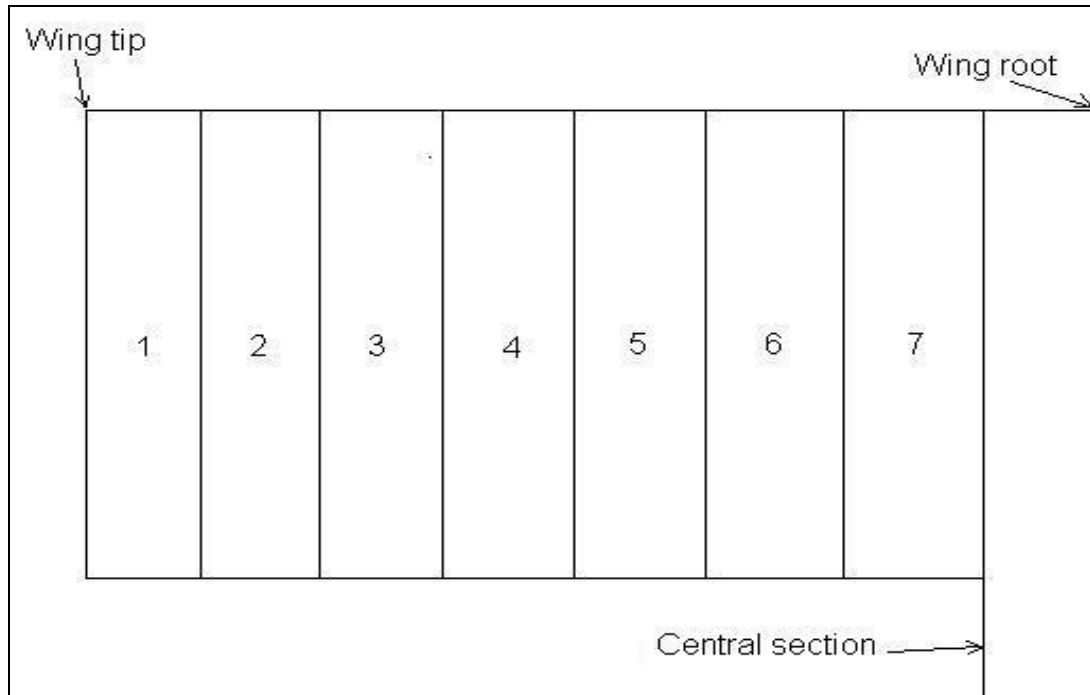


Fig. 2.2. Numbering scheme for various spanwise positions.

Position	Normalized spanwise location
1	0.9375
2	0.8125
3	0.6875
4	0.5625
5	0.4375
6	0.3125
7	0.1875

Table 2.1: Spanwise distances from the wing tip for pressure section

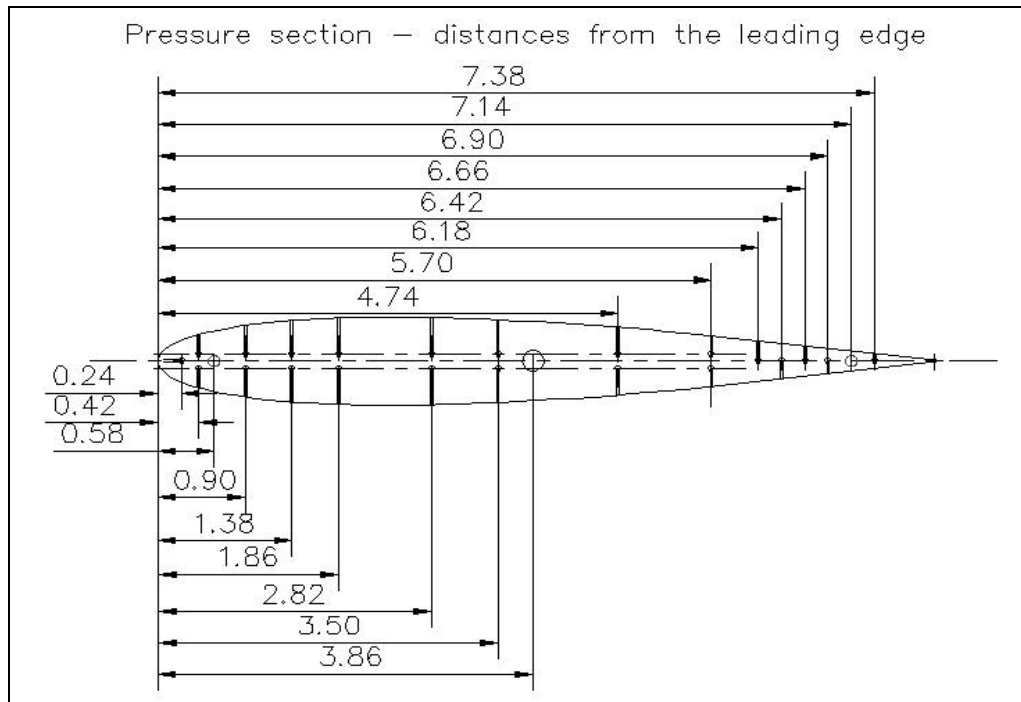


Fig. 2.3. Location of ports on the Pressure section (All dimensions in inches)

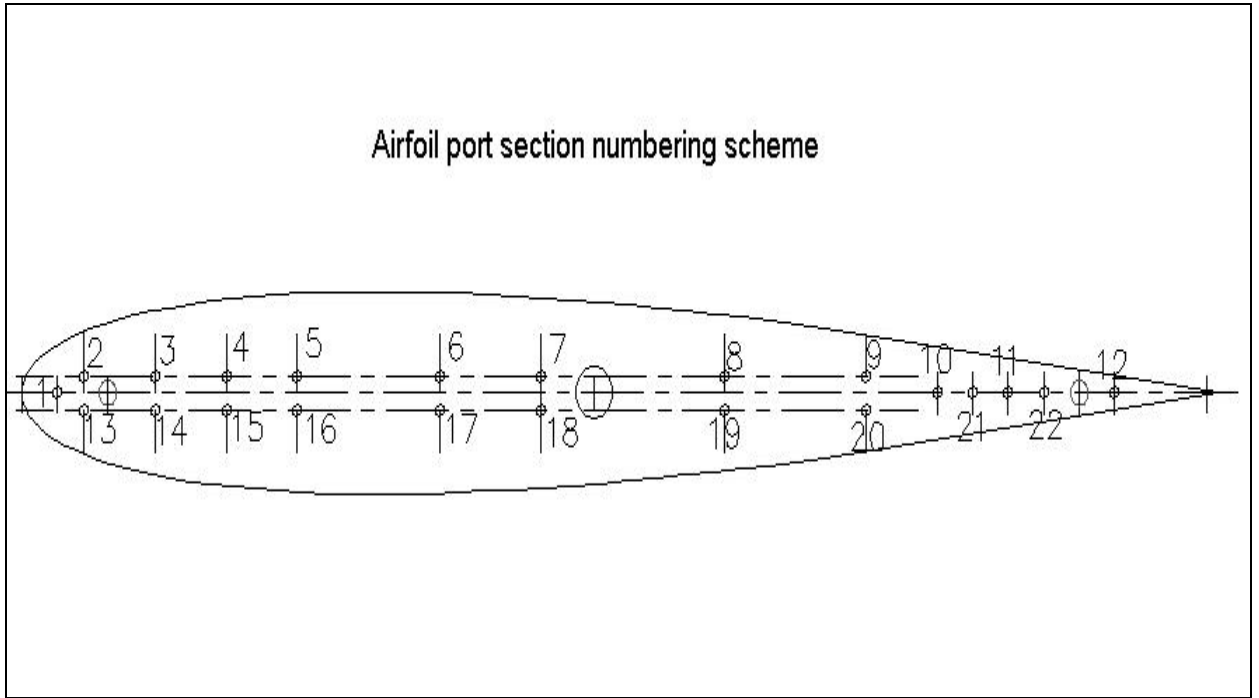


Fig. 2.4. Numbering scheme for the ports.

Port Number	x/c Location	Port Number	x/c Location
1	0	12	0.9225
2	0.0525	13	0.0525
3	0.1125	14	0.1125
4	0.1725	15	0.1725
5	0.2325	16	0.2325
6	0.3525	17	0.3525
7	0.4375	18	0.4375
8	0.5925	19	0.5925
9	0.7125	20	0.7125
10	0.7725	21	0.8025
11	0.8325	22	0.8625

Table 2.2: Chordwise locations of ports as percent chord (x/c)

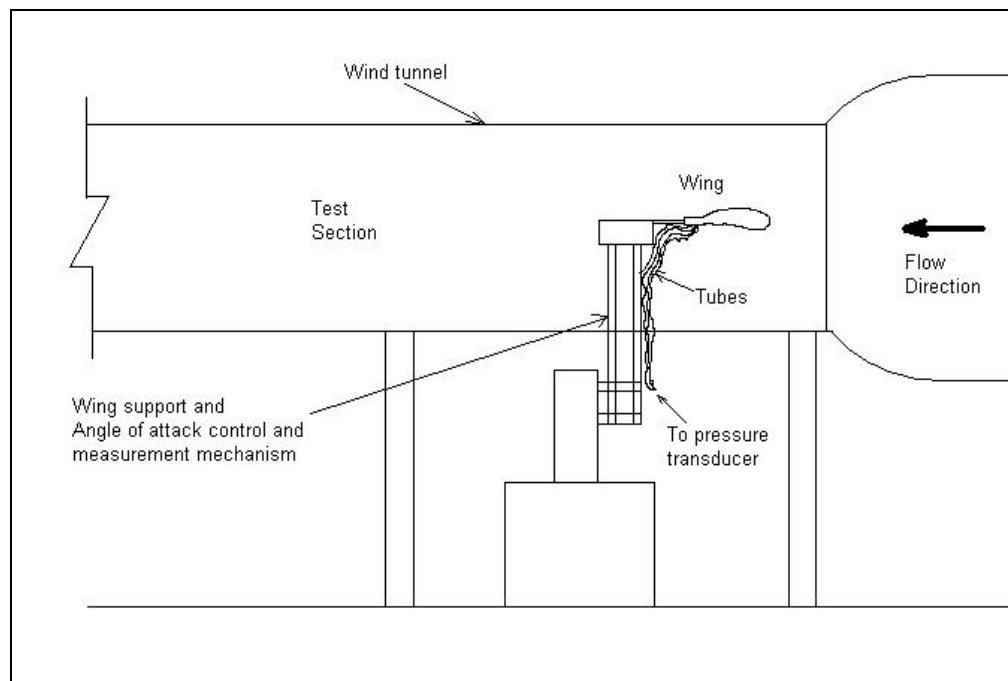


Fig. 2.5 Experimental set-up (schematic)

2.2.4 Sting balance / Angle of attack control mechanism

A commercial sting arm support from Aerolab Inc. was used to mount the wing in the wind tunnel. This set-up has an in-built mechanism to adjust the angle of attack. The angle of attack was varied between range of $0^\circ \leq \alpha \leq 18^\circ$ for the experiments. The error on the angle of attack measurement is $\pm 0.05^\circ$.

2.2.5 Lift measurement set-up using force balance

A second set of experiments was carried out in the same wind tunnel described earlier. This set of experiments consisted of lift measurements on a wing made of foam with $AR = 1$ and $c = 0.2032\text{ m}$, with a NACA 0012 airfoil shape. The wing model used for pressure measurements could not be used for these experiments because of the load range of the force balance used for the measurements. Care was taken to smoothen the surface of the airfoil by applying a smooth adhesive Mono-kote surface on the foam wing. The wing was fabricated using a hot wire with the HASS machined airfoil sections (same as used in pressure measurements) as templates.

The set up consisted of a sting support mounted on a weighing balance, Acculab Model C2400, with a range of $0\text{-}2400\text{ g}$. The weighing balance has an accuracy of $\pm 0.1\text{ g}$. The wing was mounted on the sting arm that has a provision for adjusting the angle of attack. The angles of attack were measured using a digital readout protractor. This angle-measuring device has an accuracy of $\pm 0.1^\circ$.

The repeatability of the set-up was found to be very good with no drift. The calibration slope has an error of about 2%, which was confirmed using calibration weights. The measurements recorded are adjusted for this error. All measurements were

carried out at a temperature of $73^{\circ} F$ to be consistent with the tests carried out during the pressure measurements and to avoid inaccuracies due to temperature variations.

2.3 Tygon tube out-gassing issue

Tygon tubing used for high-resolution pressure measurements can introduce errors in the measurements due to out-gassing issues. (Cimbala et.al. [23]). They observed while measuring pressures at low Reynolds numbers that the new plastic Tygon tubing out-gassed the gas trapped in during the manufacturing process. This apparently increased the density of the air inside the pressure tubing by about 25%. Although no confirmation of the presence of out-gassing was made in our study, there were certain inherent characteristics of our set-up, which would have reduced the effect of out-gassing. Cimbala et.al. [23] suggest that using a brand new tube for local pressure measurement, and an older tube (or no tube at all), for reference pressure measurements, induces the error. Our reference, as well as the measured pressures, were connected to the transducer with similar tubing which should nullify the effect of this out-gassing.

Another issue Cimbala et.al. [23] discuss is that with change in position of the transducer with respect to the position of the reference pressure port (height difference change) their pressure reading changes. This occurs only if out-gassing in the tubes is an issue. The reason behind this in their case was that they were measuring pressures with reference to the atmospheric pressure with substantial height difference between the measured and reference port locations. We have confirmed that our pressure readings do not change with change in height (location) of the pressure transducer thus showing any out-gassing effects are negligible. In our case the reference pressure port (pitot-static

probe) and measurement port (wing surface) are at essentially the same elevation inside the wind tunnel, thereby minimizing the effect.

2.4 Velocity Distribution across wind tunnel

Measurements were carried out to verify the variation of velocity (dynamic pressure) across the axes of the wind tunnel test section. The dynamic pressure measurements were carried out at a speed of around 3.65 m/s , yielding a Reynolds number of about $Re = 50000$. The measured data is shown in Figure 2.6. As seen from this figure, the velocity distribution remains fairly constant over about 70% of the test section on both sides of the origin. The model wing spanned only the central 30% section of the wind tunnel. This confirms the presence of constant velocity over the model wing in the region where experiments were carried out in the wind tunnel test section.

The variation of velocity at the walls can be associated with the boundary layer developed on the wall. Assuming a laminar boundary layer, we have the thickness of the boundary layer, δ given as,

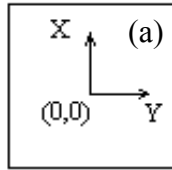
$$\delta = x \cdot \frac{5}{\sqrt{Re_x}}$$

where x = distance at which the boundary layer thickness is measured = 45 cm from the test section inlet and Re = Reynolds number based on this length = 109415 .

(x and Re are based on the position where velocity measurements were carried out).

This gives a boundary layer thickness of $\delta = 0.2678 \text{ in}$, which is of the order of distance from the test section walls where a large variation in speed is observed. So this velocity variation can be attributed to the boundary layer development on the test section walls.

For a turbulent boundary layer, boundary layer thickness will be smaller.



Test section

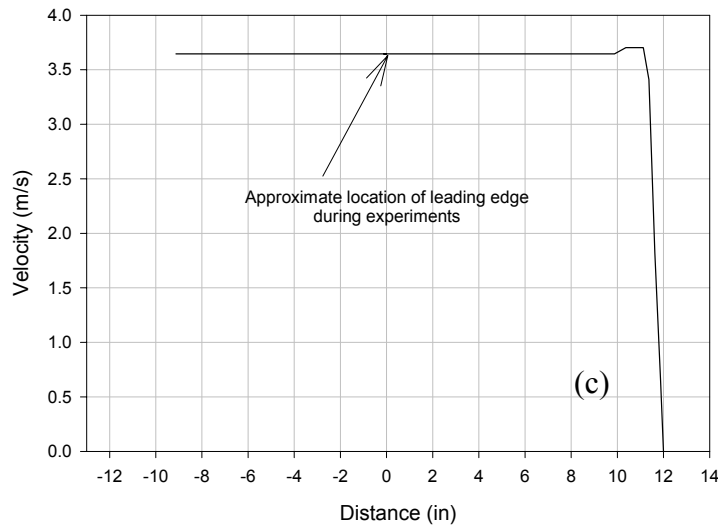
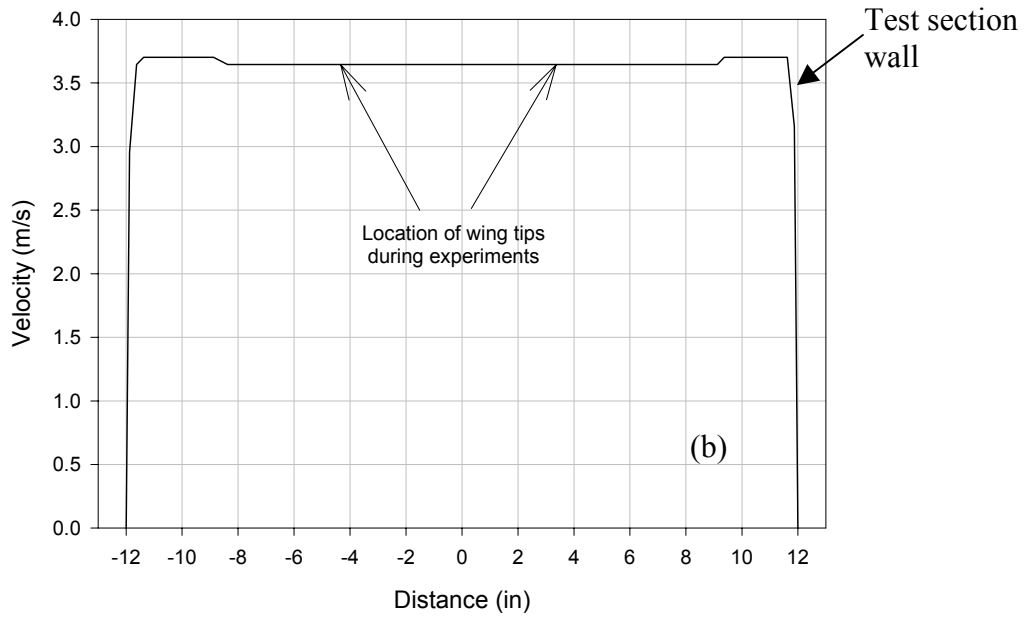


Fig. 2.6 Velocity Distribution across wind tunnel
 (a.) Axes terminology, (b.) Y-axis distribution (c.) X-axis distribution
 (Data for x-axes plotted for ' $Y \geq -9$ ' due to limitations in set-up)

2.5 Experimental Procedure

After setting the wing at the desired angle of attack, the wind tunnel was set to the desired free stream velocity. Measurements were then taken for all 22 ports. This was repeated for the remaining angle of attacks and Reynolds numbers for that particular spanwise location before moving the pressure section to a new spanwise location. This was done because the relocation of the pressure section was the major time consuming part of the experiments. To confirm that this procedure led to repeatable measurements, a second set of experiments was carried out at a fixed angle of attack and fixed Reynolds number, with the pressure section moved sequentially to the various spanwise locations. Identical results were obtained for both methods of data collection. The earlier mentioned method led to the most efficient scheme of data collection.

Measurements were carried out with the temperature of the free stream flow maintained at $73^{\circ} F$ using a water cooled heat exchanger in-built in the wind tunnel. The experimental matrix in Table 2.3 presents angles of attacks and Reynolds number combinations at which the measurements were carried out.

Velocity	Reynolds Number	Angle of attack, α
(m/s)		(degrees)
2.23	30218	0,6,15
2.66	35966	0,6,15
3.22	43615	0,3,6,9,12,15,18
3.65	49345	0,6,15
6.21	84122	3,6,9,12,15,18

Table 2.3. Experimental Matrix

2.6 Error analysis

The accuracy of the pressure transducer used introduces an error in the measurements. This accuracy, as informed by the manufacturer is $0.25\% FS$ (0.0005 in of water). We have used the Root sum of squares method for the error analysis. The maximum error was found for the data at $Re=30218$ where the dynamic pressure (q) values were lowest, resulting in higher error in the pressures measured. This maximum error in the pressure coefficients was found to be of the order of $\pm 3.5\%$. Error bar will be presented on later pressure coefficient curves in the Results section. This results in an error in the calculated local lift coefficient on the order of $\pm 1\%$. Error in the total lift coefficient obtained from the pressure measurements was about $\pm 1.2\%$. Errors in other readings were found to be lower than these. The error on the angle of attack measurement for the pressure measurement set up is $\pm 0.05^\circ$. The error in angle of attack measurements for the lift measurements using force balance is $\pm 0.1^\circ$. Sample error calculations for pressure coefficients and the local lift coefficient are shown in Appendix D.

3. Results

This section will describe the various results obtained in this research. This section will also include the discussion of these results. The result section will consist of pressure coefficient distributions for various Reynolds numbers and angles of attacks. The pressure coefficients are integrated to determine the local (spanwise) lift coefficients. This section will also discuss the lift curve slope at two Reynolds numbers and the span efficiency factor at various Reynolds numbers and angles of attacks.

3.1 Local Pressure measurements

The pressure measurements were carried out for the complete experimental matrix described in Section 2.4. The results from these measurements are discussed in this section. Typical pressure distribution curves and plots are presented.

Fig 3.1 (a-g) shows the pressure coefficient curves for the upper (C_{pu}) and lower surface (C_{pl}) of the wing, plotted against the percent chord (x/c) for $Re=35966$ at $\alpha = 15^\circ$. Fig 3.2 presents the same plots for $Re = 35966$ at $\alpha = 6^\circ$. The $Re = 35966$ case is a moderate Re in the middle of our studied Reynolds numbers range. Fig 3.1 and 3.2 will serve as representative C_p distributions, in order to first discuss the overall features of other measured C_p distributions. Later we will present C_p distributions at other Re and α combinations needed to discuss additional observed phenomenon. Pressure distributions for complete experimental matrix are shown in [appendix A](#). From equation 11 in Section 2.1, the area between the upper and lower surface C_p curves is a measure of the lift coefficient. Figures 3.1 and 3.2 indicate that the lift coefficient varies along the span. The spanwise lift coefficient curves, based on these C_p plots are presented and discussed later

in this section. The pressure coefficient plots ‘a-g’ are plotted for pressure section at Positions 1-7 (explained earlier) respectively.

Three distinct types of pressure distributions can be observed in Fig. 3.1 by focusing on the upper surface. Near the wing tip (Fig. 3.1a) a low-pressure region (where C_p values decrease dramatically to larger negative values) appears to exist for $0.2 < x/c < 0.4$. In Fig. 3.1 b for Pos 2, this low-pressure region disappears. For the remaining Figs. 3.1 c - 3.1 g nearer to the central span region the pressure coefficient values do not reach the large negative values around the mid-chord region as in the case of wing tip distributions. A separation region exists for all these positions characterized by a plateau in the pressure distribution for $0.15 < x/c < 0.2$. The effect of the laminar separation bubble on the outer flow is to increase the velocity, resulting in this plateau shape of the pressure distribution [27]. We observe that the width of this plateau (separation region) remains fairly constant near the central span region for Figs. 3.1 c – 3.1 g, but is reduced in size near the wing tip in Fig. 3.1 b. The sudden decrease in the pressure coefficients (towards lower negative values) also suggests the presence of the separation bubble in the plateau region. This decrease in pressure can be associated with the increase in velocity at the separation bubble.

Torres & Mueller [17] have observed separation regions in the same location in their flow visualization studies. Fig 3.3 shows a reproduction of their flow visualization for a wing with $AR = 1$ at $Re = 7 \times 10^4$. These plots clearly show the separation bubble for $\alpha = 5^\circ$, with no separation at the wing tips. The reader can refer to Fig. 31 from [17] for additional results. They suggest, “The tip vortices energize the flow and eliminate the presence of the separation bubble”. Our results seem to be consistent with their findings;

in our case the energized flow from the wing tip vortex eliminates the separation bubble, and creates a low-pressure region. Torres & Mueller have stressed that low pressure cells on the wing's upper surface can be formed by the wingtip vortices at low AR, leading to the so-called 'nonlinear lift' which occurs in addition to the linear lift due to fluid circulation.

Figure 3.2 (a-g) shows similar pressure coefficient plots at the same Reynolds number and at $\alpha = 6^\circ$. Comparing Figure 3.1 and 3.2 we observe that the plateau region disappears for Figs. 3.2 c – 3.2 g. This indicates that the separation bubble is absent for lower angles of attack. A fairly constant C_p distribution can be observed for Figs 3.2 a – 3.2 g in the region $0.2 < x/c < 0.8$, indicating an attached laminar flow over the wing. This flow is further confirmed with the overall lower values of pressure coefficients in this region.

Fig 3.4 shows the pressure distribution plots for $Re = 30218$ and $\alpha = 15^\circ$. Fig 3.5 shows these plots at same Re and at $\alpha = 6^\circ$. This is the lowest Reynolds number at which measurements are carried out in this research. The velocity range of the wind tunnel limited the lowest Reynolds number reached. Fig 3.6 shows the pressure distribution plots for $Re = 84122$ and $\alpha = 15^\circ$. Fig 3.7 shows these plots at $Re = 84122$ and at $\alpha = 6^\circ$. This is the highest Reynolds number for which pressure measurements are carried out. The range of the pressure transducer limited this highest Reynolds number reached. Comparing the C_p distributions for $Re = 35966$ with those for $Re = 30218$ and $Re = 84122$, we observe that the overall trend of the C_p plots remains the same. The magnitudes of the pressure coefficients are found to be different. A very wide plateau region can be observed in Fig 3.4 g as compared to other C_p plots for Pos 7 at $\alpha = 15^\circ$.

Figs 3.8 and 3.9 show pressure distributions at $Re = 49345$ at $\alpha = 15^\circ$ and $\alpha = 6^\circ$ respectively. This Reynolds number is a point of transition in the behavior of the flow over the low AR wings. Earlier investigators have observed typical trends at this Reynolds number. The low-pressures for the upper surface in Fig. 3.7a and 3.8a are higher as compared to those observed for other Reynolds numbers. This hints on some, yet unknown, but peculiar phenomenon occurring at this Reynolds number.

Figs 3.4 a-g also show the error bars on the pressure coefficient plots. We present the error bars only for this Reynolds number to demonstrate the typical values of error involved in these measurements. As explained earlier the error analysis is based on RSS type uncertainty. The error involved in other C_p measurements is of the same order or lower than the error at this Reynolds number.

Fig. 3.10 shows the pressure coefficient plots for a Reynolds number of $Re=43615$, to summarize the effect of variation of α on C_p distribution curves. Fig 3.10-a is plotted for the pressure section being at the tip (Pos 1), at different α values. It can be observed in Fig. 3.10-a that the upper surface pressure coefficients drastically change to higher negative values with increasing angle of attack. The pressure coefficients for $\alpha = 18^\circ$ are much higher (negative) than those seen for $\alpha = 3^\circ$. The wing tip vortices become stronger with increase in angle of attack and the flow is further energized. This leads to lower pressures at the wing tips and the resultant drop in pressure coefficients.

Fig. 3.10-b shows the pressure coefficient plots for Pos 4, which is approximately quarter span length distance away from the wing tip. The gradually developing plateau region with increase in angle of attack for the upper surface curve can be clearly seen in

Fig 3.10b. The plateau region is absent for $\alpha = 3^\circ$, but a clearly developed plateau can be seen for $\alpha = 18^\circ$. Measurements at various angles of attack in this range show that the separation bubble gradually develops with increase in the angle of attack.

Figs. 3.11a-3.12a plot the pressure coefficients at various Reynolds numbers at $\alpha = 6^\circ$ and $\alpha = 15^\circ$ respectively for Pos 1. Figs 3.11b – 3.12b plots the C_p distribution for the same Reynolds numbers and angles of attack for Pos 6. It can be observed from the Fig. 3.11 that the C_p 's, for both the upper surface and the lower surface, remained fairly constant for all the Reynolds numbers shown. No fixed trend is observed in the C_p distributions here. Fig 3.12a shows the changes in the low-pressure region with the Reynolds number. For $Re = 49345$ the upper surface pressure coefficients are higher as compared to those for $Re = 30218$ and $Re = 84122$. The low-pressure region for Pos 1 and the plateau region for Pos 6 show the development of separation bubble. Fig. 3.12 shows for Pos6 the trends for C_p distributions are fairly monotonic with lowest pressures reached decreasing with Reynolds numbers. The increase in pressure behind the separation bubble has a reversed trend with the pressure increase being inversely proportional to Reynolds number.

Figs 3.13 a – 3.13 b show the pressure coefficient plots for $Re = 30218$ and $Re = 49345$ at $\alpha = 0^\circ$. These figures illustrate that no lift is generated at zero angle of attack as is expected from a symmetric airfoil. The zero lift was also observed for other positions and other Reynolds numbers. The existence of zero lift also validates the pressure measurement set up and ensures the accuracy of the readings obtained for other angles of attack.

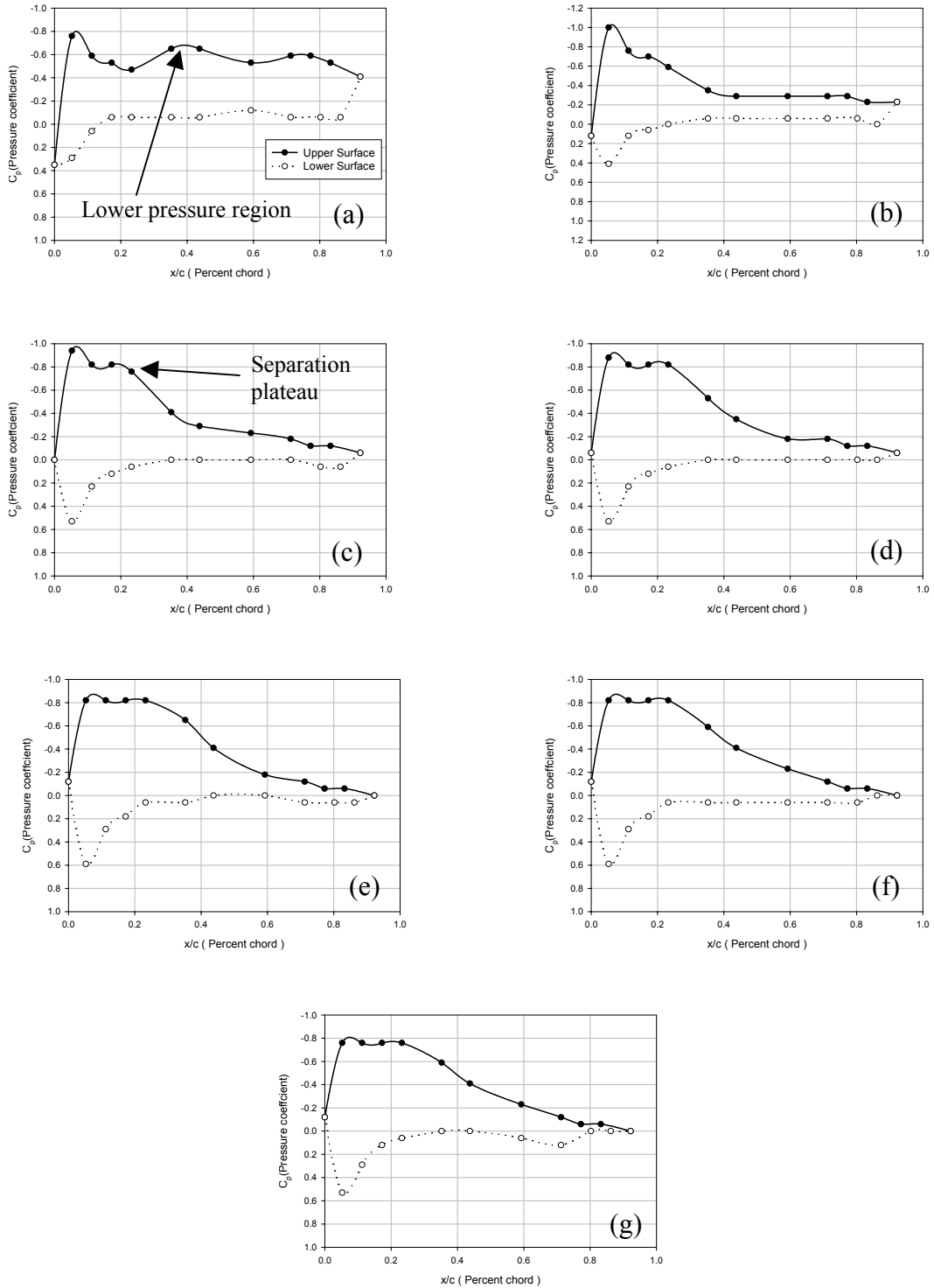


Fig. 3.1 C_p vs x/c plots for $Re = 35966$, $\alpha = 15^\circ$; (a) Pos 1, (b) Pos 2, (c) Pos 3, (d) Pos 4, (e) Pos 5, (f) Pos 6, (g) Pos 7.

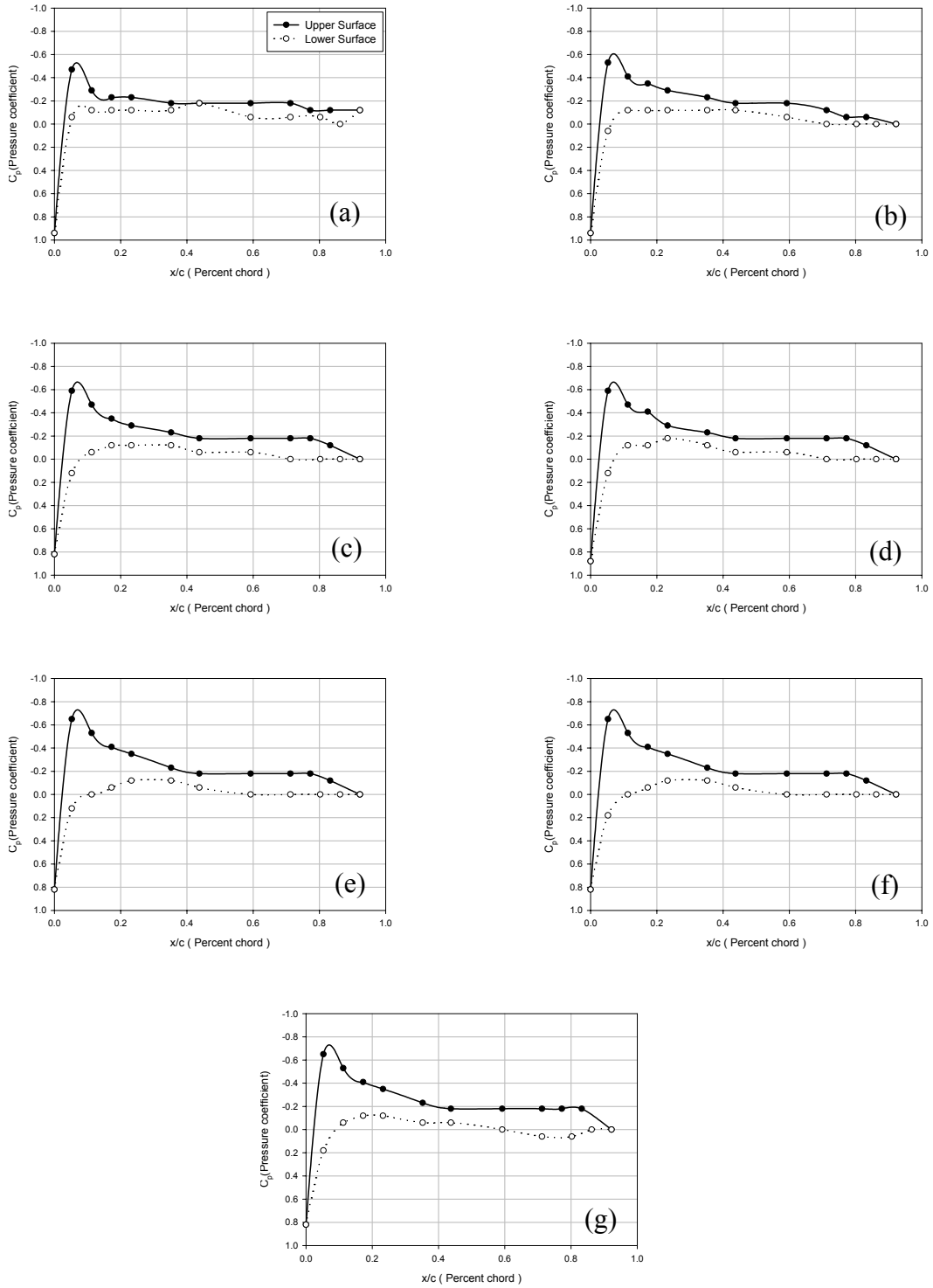


Fig. 3.2 C_p vs x/c plots for $Re = 35966$, $\alpha = 6^\circ$; (a) Pos 1, (b) Pos 2, (c) Pos 3, (d) Pos 4, (e) Pos 5, (f) Pos 6, (g) Pos 7.

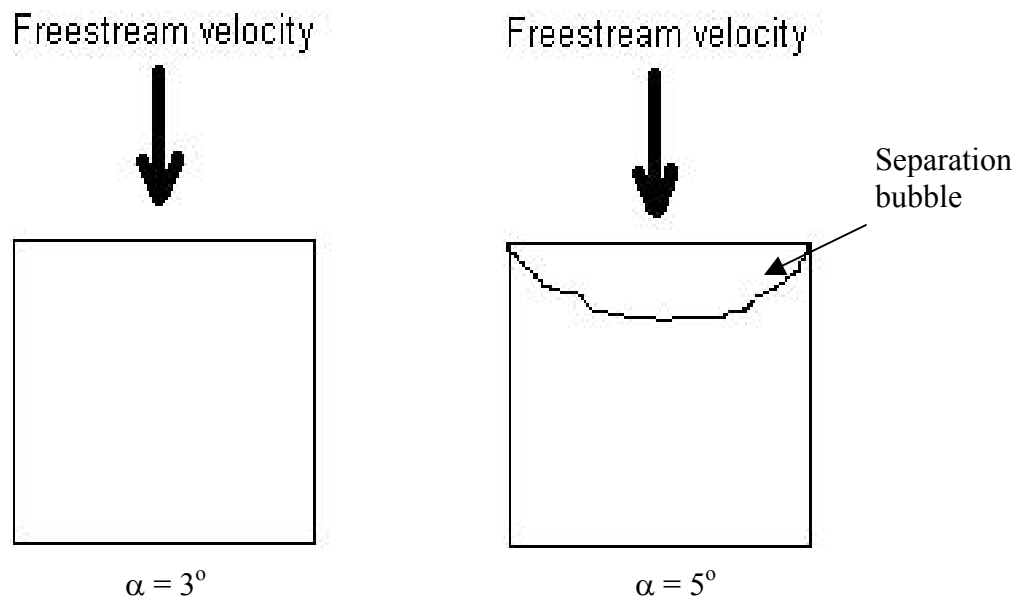


Fig 3.3 Reproduction of Flow visualization observed by Torres and Mueller [17]
for AR = 1, Re = 70000
(Separation bubble labels have been added)

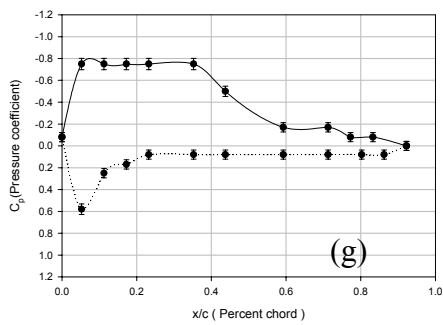
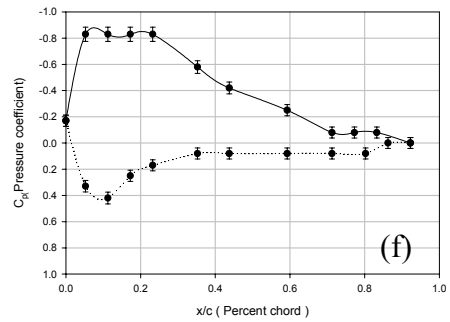
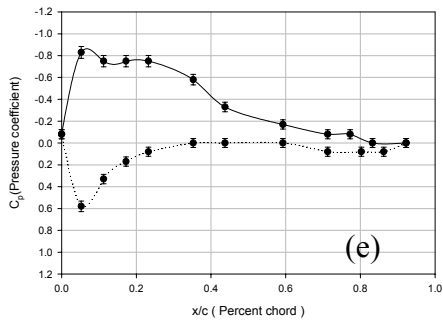
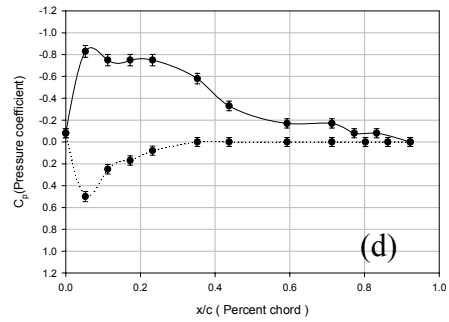
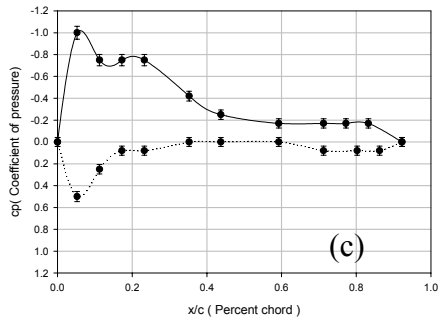
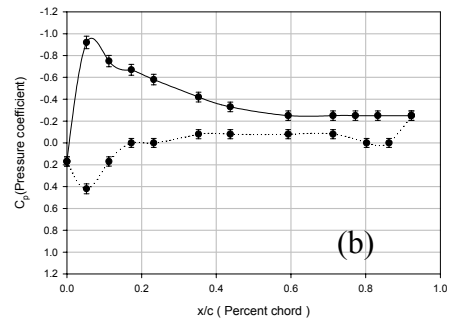
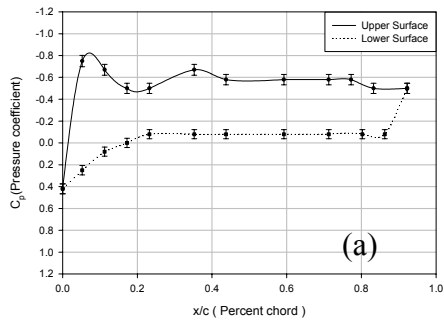


Fig. 3.4 C_p vs x/c plots for $Re = 30218$, $\alpha = 15^\circ$, with error bars; (a) Pos 1, (b) Pos 2, (c) Pos 3, (d) Pos 4, (e) Pos 5, (f) Pos 6, (g) Pos 7.

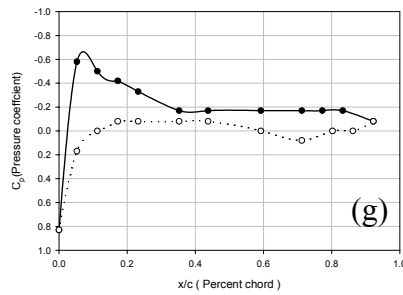
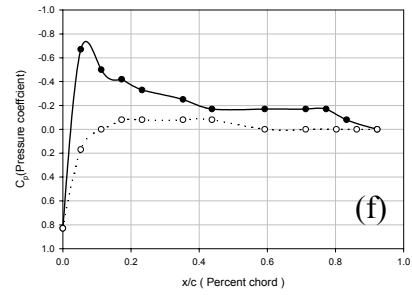
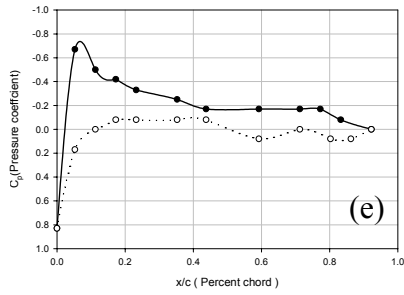
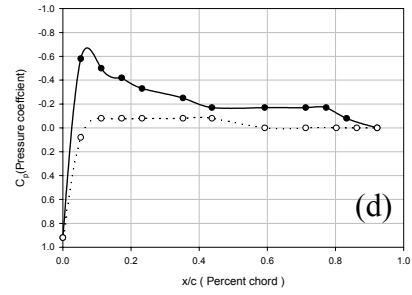
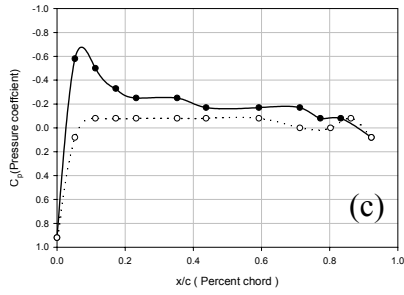
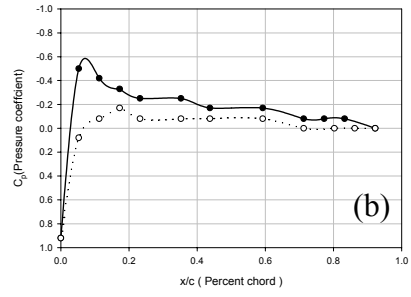
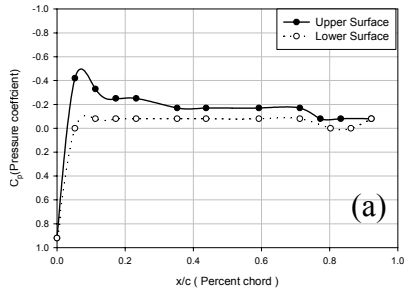


Fig. 3.5 C_p vs x/c plots for $Re = 30218$, $\alpha = 6^\circ$; (a) Pos 1, (b) Pos 2, (c) Pos 3, (d) Pos 4, (e) Pos 5, (f) Pos 6, (g) Pos 7.

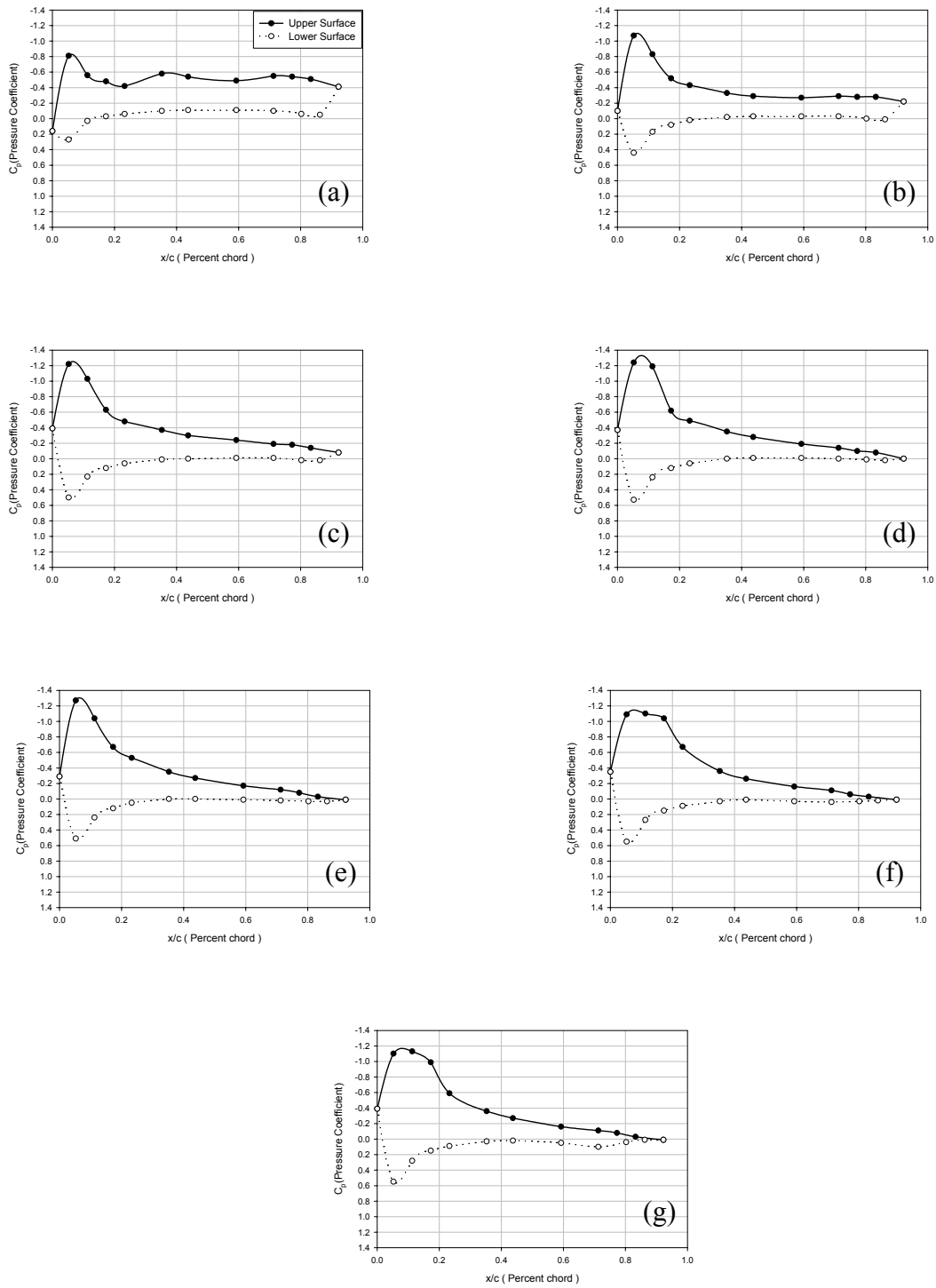


Fig. 3.6 C_p vs x/c plots for $Re = 84122$, $\alpha = 15^\circ$; (a) Pos 1, (b) Pos 2, (c) Pos 3, (d) Pos 4, (e) Pos 5, (f) Pos 6, (g) Pos 7.

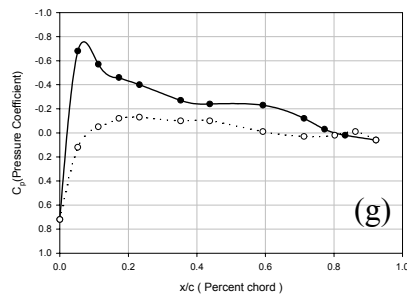
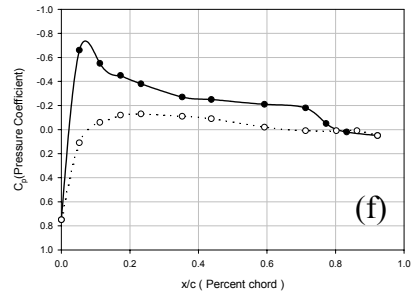
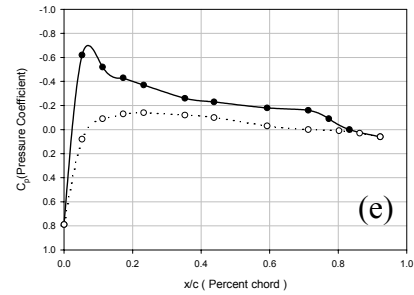
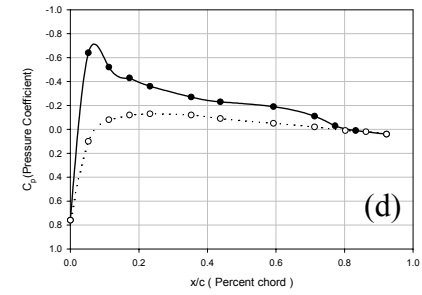
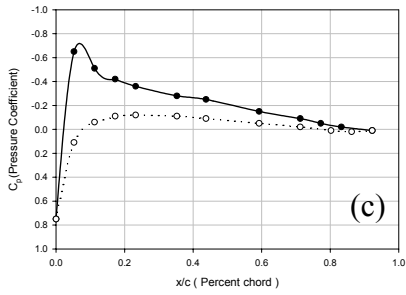
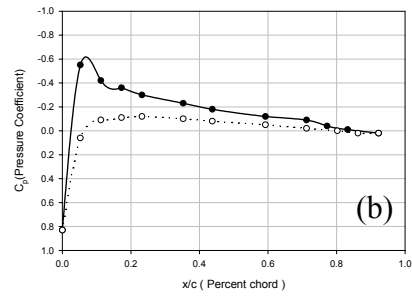
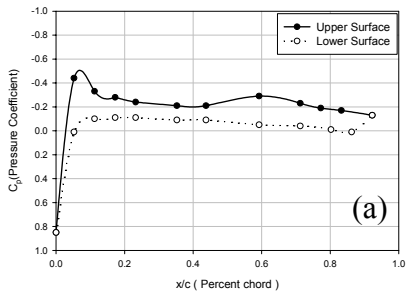


Fig. 3.7 C_p vs x/c plots for $Re = 84122$, $\alpha = 6^\circ$; (a) Pos 1, (b) Pos 2, (c) Pos 3, (d) Pos 4, (e) Pos 5, (f) Pos 6, (g) Pos 7.

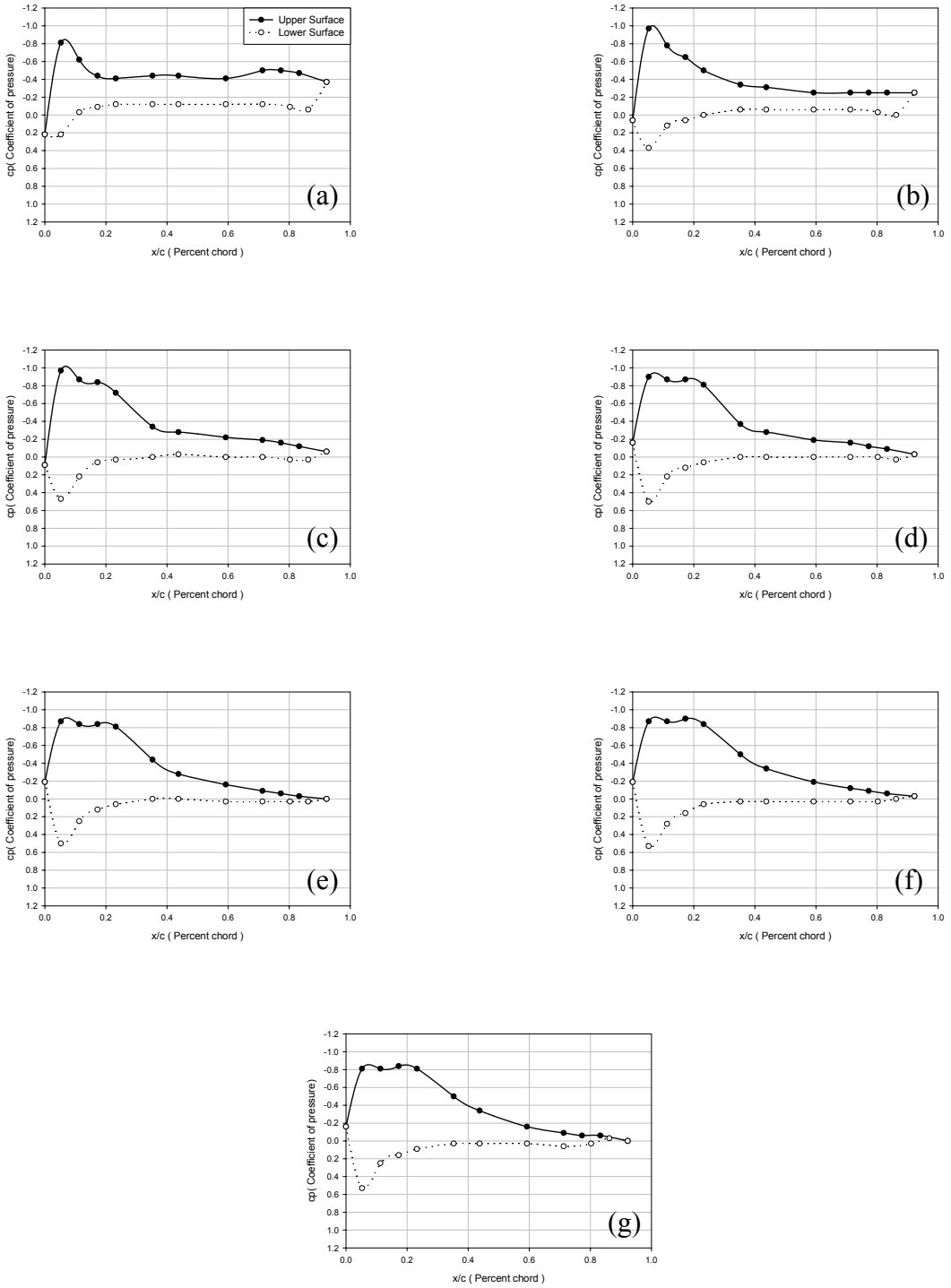


Fig. 3.8 C_p vs x/c plots for $Re = 49345$, $\alpha = 15^\circ$; (a) Pos 1, (b) Pos 2, (c) Pos 3, (d) Pos 4, (e) Pos 5, (f) Pos 6, (g) Pos 7.

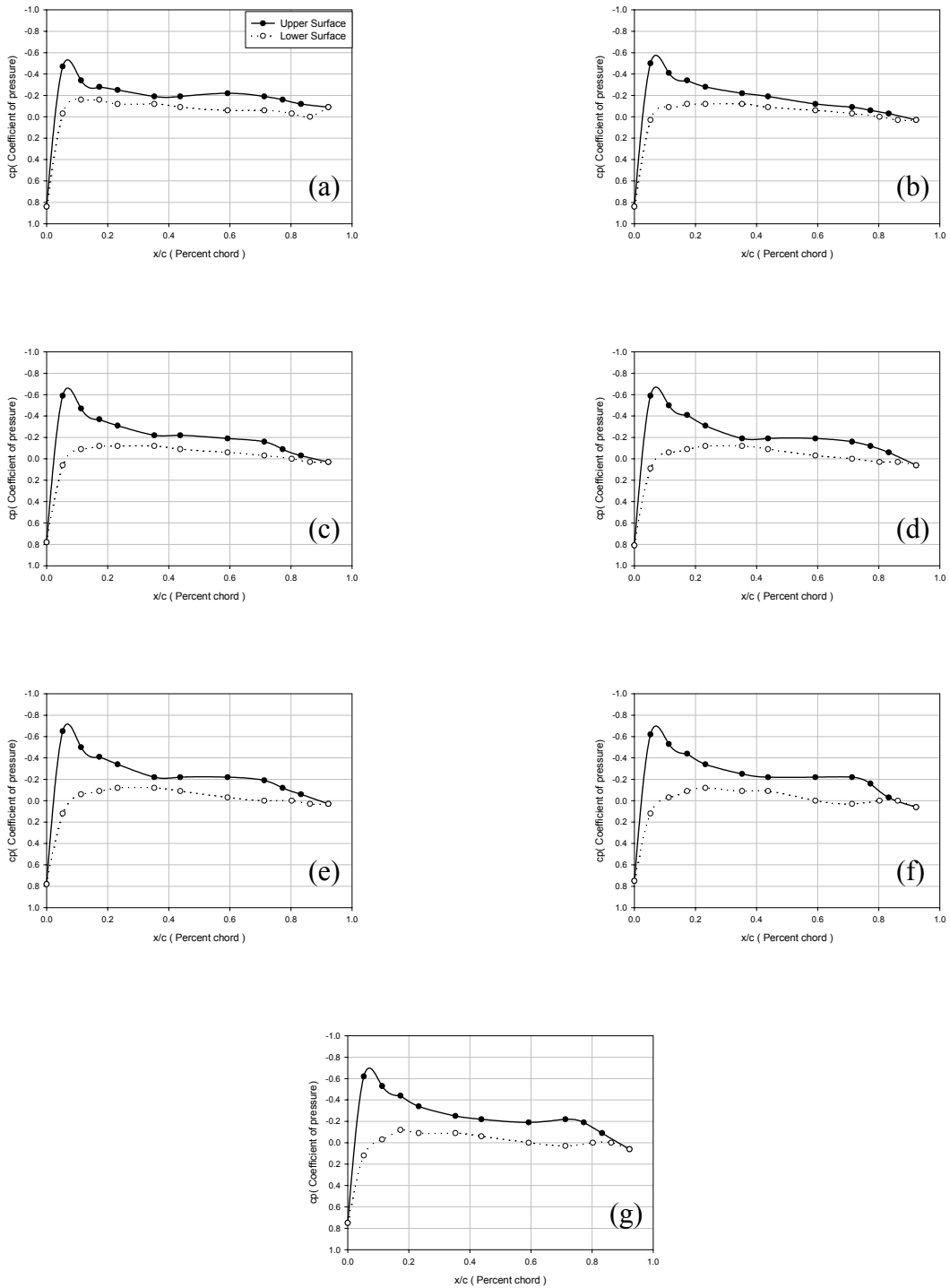


Fig. 3.9 C_p vs x/c plots for $Re = 49345$, $\alpha = 6^\circ$; (a) Pos 1, (b) Pos 2, (c) Pos 3, (d) Pos 4, (e) Pos 5, (f) Pos 6, (g) Pos 7.

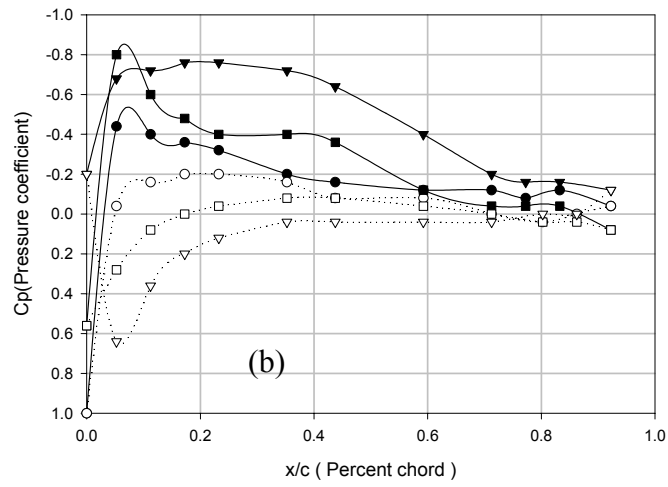
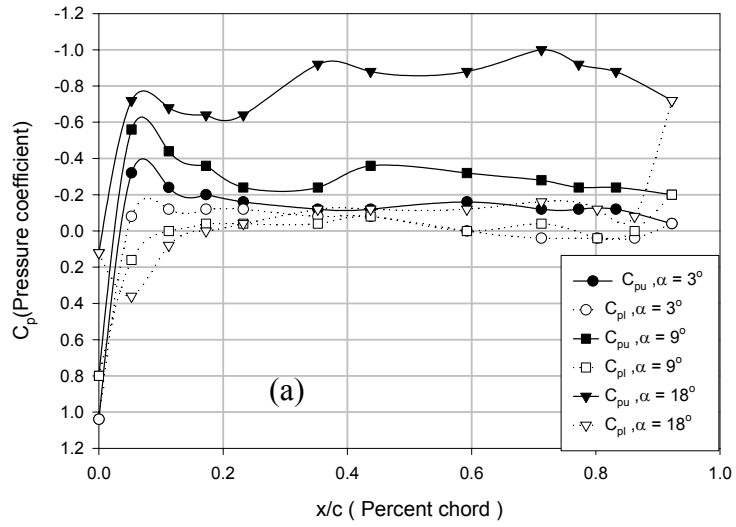


Fig. 3.10 Effect of variation of α on C_p distribution for $Re = 43615$; (a) Pos 1 (b) Pos 4

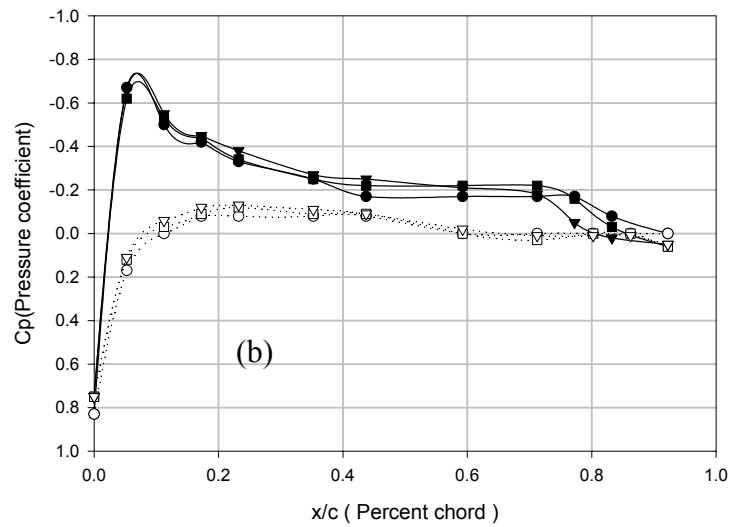
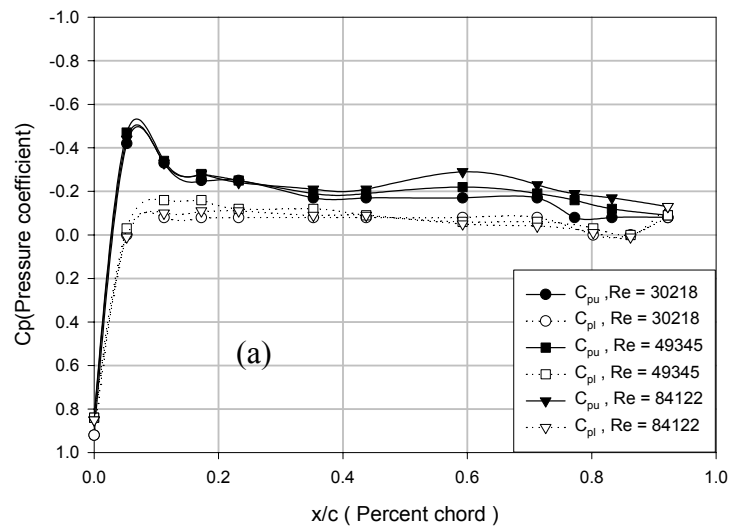


Fig. 3.11 Effect of variation of Re on Cp distribution for $\alpha = 6^\circ$; (a) Pos 1 (b) Pos 6

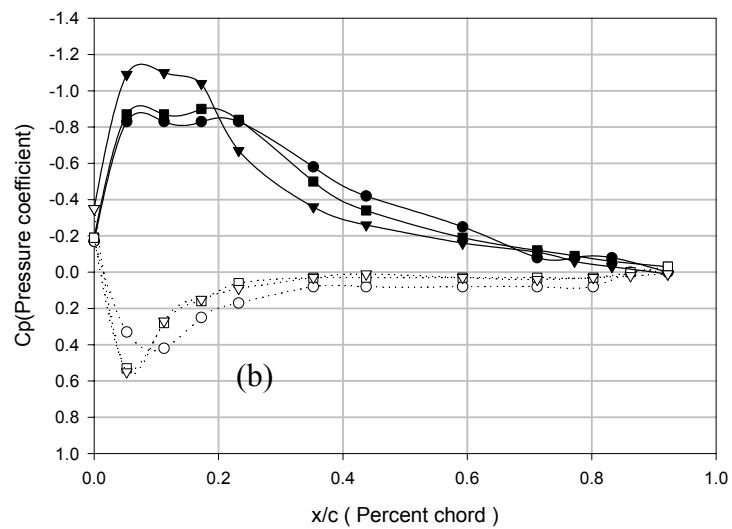
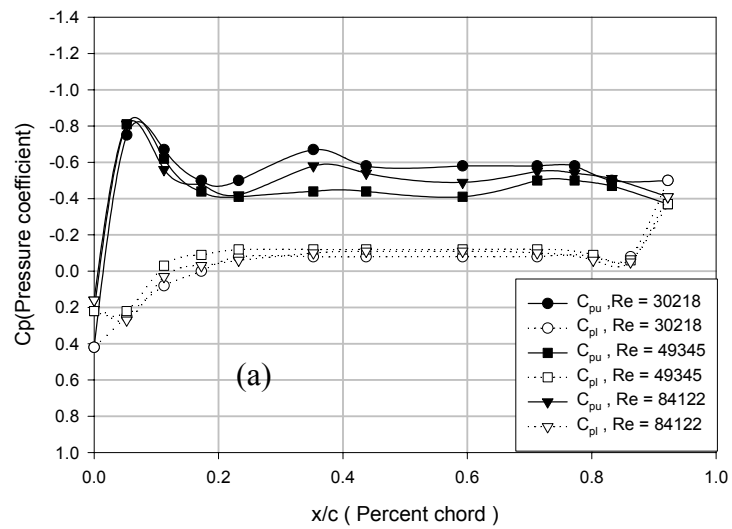


Fig. 3.12 Effect of variation of Re on Cp distribution for $\alpha = 15^\circ$; (a) Pos 1 (b) Pos 6

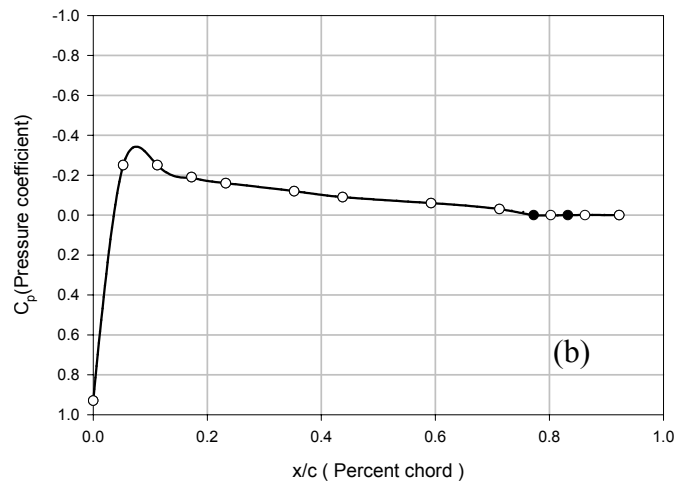
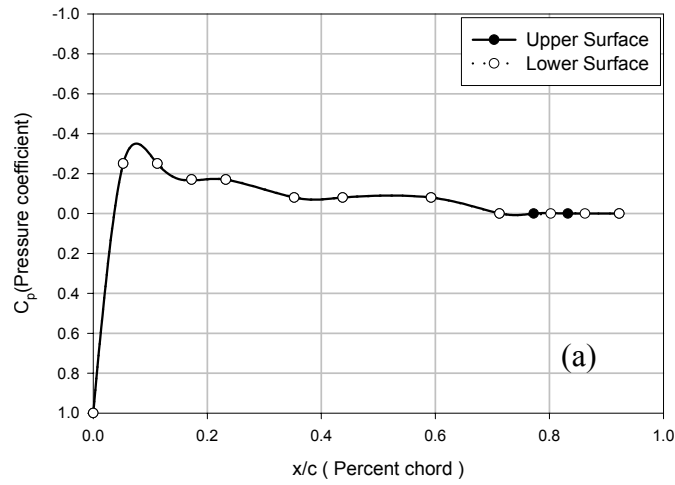


Figure 3.13 C_p vs x/c plots at $\alpha = 0^\circ$ for Pos 1; (a) $Re = 30218$, (b) $Re = 49345$

3.2 Spanwise Lift Distributions

Integration of the area under pressure coefficient curves such as those presented in the last section yields local lift coefficient values. Figures 3.14 and 3.15 show the local lift coefficient distributions for $3 \times 10^4 \geq Re \geq 8.5 \times 10^4$ at $\alpha = 15^\circ$ and 6° respectively. The variations in area under the pressure coefficients curve yield varying spanwise lift coefficients. Although the local lift coefficients appear to be in the same range for all the Reynolds number at a given spanwise location, the total lift generated increases with increase in Reynolds number. Comparing Fig 3.14 with Fig 3.15 we observe that there is an increase in the magnitude of the local lift coefficient at a given spanwise location for the two angles of attack resulting in increase in lift at higher angle of attack.

The most striking feature of Fig 3.14 and 3.15 is the presence of a peaked lift region near the wing tip at $z/(b/2) \approx 0.9$. The low-pressure region in the C_p curves (see Fig. 3.1), results in a large increase in area under the C_p vs x/c curve compared to the other positions. This results in a dramatic increase (peak) in the lift coefficient near the wing tip. Although it varies in magnitude, this peak can be observed for all the Reynolds numbers and for both angles of attacks presented here. This peak is less prominent at $\alpha = 6^\circ$ except for $Re = 84122$ case. No fixed trend was found for the nature of this peak, but at $\alpha = 15^\circ$ and at the critical Reynolds number of $Re = 49345$ there is a drop in this peak. The location of the peak is at approximately $z/(b/2) = 0.9$ over our measured range of Re . This corresponds to the wingtip vortex core location measured by Desabrais and Johari [20] on a rectangular NACA 0012 wing at $Re = 6.8 \times 10^4$. Table 1 from [20] lists the locations of vortex core from their study. Fig 3.16 shows the approximate location of the wing tip vortex core on a wing. We surmise that the high velocity core region induces the

low-pressure region on the upper surface near the wingtip. Although no actual measurements were taken, a data point at the wing root has been added in all c_l vs $z/(b/2)$ plots, assuming a linear trend beyond measurement for Pos 7. This was necessary to calculate the total lift coefficient for the wing.

Figs 3.17 a- 3.17c and 3.18 a- 3.18c show the comparison of the measured lift distributions with an elliptical lift distribution. It can be clearly observed that the measured lift distributions are deviating significantly from an elliptic lift distribution. This deviation from the elliptic distribution affects the total lift generated and the induced drag on the wing. These issues will be discussed in further details later in this section. The elliptical lift distribution is determined by keeping the area under the lift coefficient curve the same as that obtained for the measured lift distribution, since comparison of lift distributions with same amount of generated lift is appropriate. Although the elliptical lift distribution is obtained on a wing with elliptical planform and the wing used for the experiments in this thesis is a rectangular wing, the comparison was made since an elliptic lift distribution ensures minimum induced drag. For an optimum MAV performance the desired lift distribution would be elliptic, hence comparison of the measured lift distribution with this ideal lift distribution will further help in understanding the design of the wing planform shape.

Furthermore we carried out tests using equation (24), the fundamental equation of finite wing theory, to determine the lift distribution for a rectangular wing with a given aspect ratio. Fig. 3.19 shows the results obtained. As can be clearly seen from the Figure as the AR increases the lift distribution becomes more and more rectangular. At $AR = 1$ the lift distribution is nearly elliptical. Schlichting, H [11] shows that as AR approaches

zero the lift distribution becomes elliptic. Fig 3.19 demonstrates this fact. Hence the comparison of the measured lift distribution with an elliptic lift distribution becomes a close approximation to comparing the measured lift distributions with a lift distribution for a rectangular wing with $AR = 1$.

Comparing all the plots in Figs 3.17 and 3.18 we observe that the measured lift distribution clearly deviates from the elliptic lift distribution. This results in a deterioration of the wing performance. The value of span efficiency factor discussed earlier in Section 2.1 reduces to a value lower than 1. Other investigations (Torres and Mueller [17] etc) have observed dramatic reduction in the wing performance, e.g. low 'e' values and high induced drag for low AR wings in this Reynolds number range. This issue will be addressed in detail later in this section.

It can be clearly seen from all these figures that the lift distribution differs drastically from the elliptic distribution at the peak near the wing tip. On rest of the wing, near the central span region, the lift distribution is fairly close to desired. We surmise that this peak could be a major factor for the dramatic increase in induced drag on low AR wings. Comparing Figs 3.17a-b and 3.18a-b we observe that at lower angle of attack of $\alpha = 6^\circ$, the deviation from the elliptic distribution is less than that for $\alpha = 15^\circ$.

Fig 3.20 shows variation of lift coefficients at two different Reynolds numbers with varying angles of attack. We observe a monotonic trend for both the Reynolds numbers. The magnitude of local lift coefficients increases with increasing angle of attack indicating increase in overall lift. The peaked lift region near the wing tip exists for almost all the angles of attack for both the Reynolds numbers, but the sharpness of the peak tends to increase with increasing angle of attack. Fig 3.21 shows the typical error

bars for the local lift distribution curves for $Re = 30218$ at $\alpha = 15^\circ$. This was calculated based on the error involved in the C_p measurements discussed earlier. The error involved in these calculations is small, hence the presence of peaked lift near the tip can be concluded to be an actual peak and not an effect of error involved in the C_p measurements.

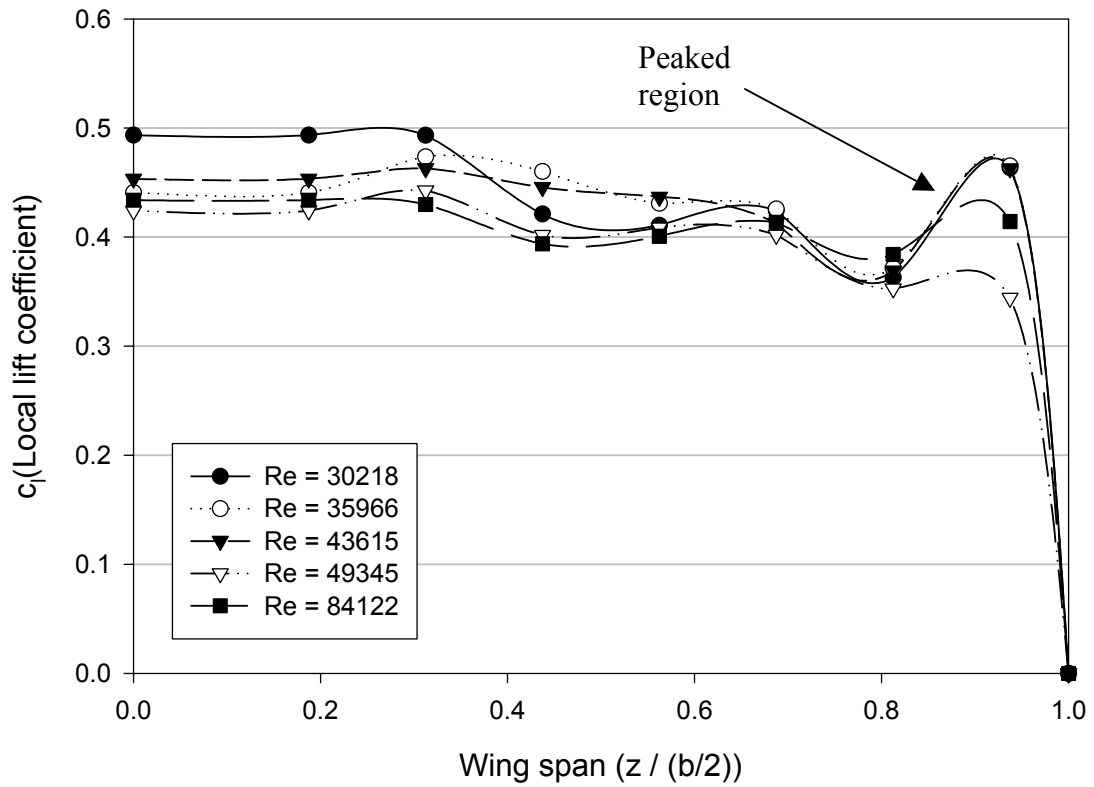


Figure 3.14 Local lift coefficient distribution for various Reynolds numbers at $\alpha = 15^\circ$, Spline curve fits through the data are shown.

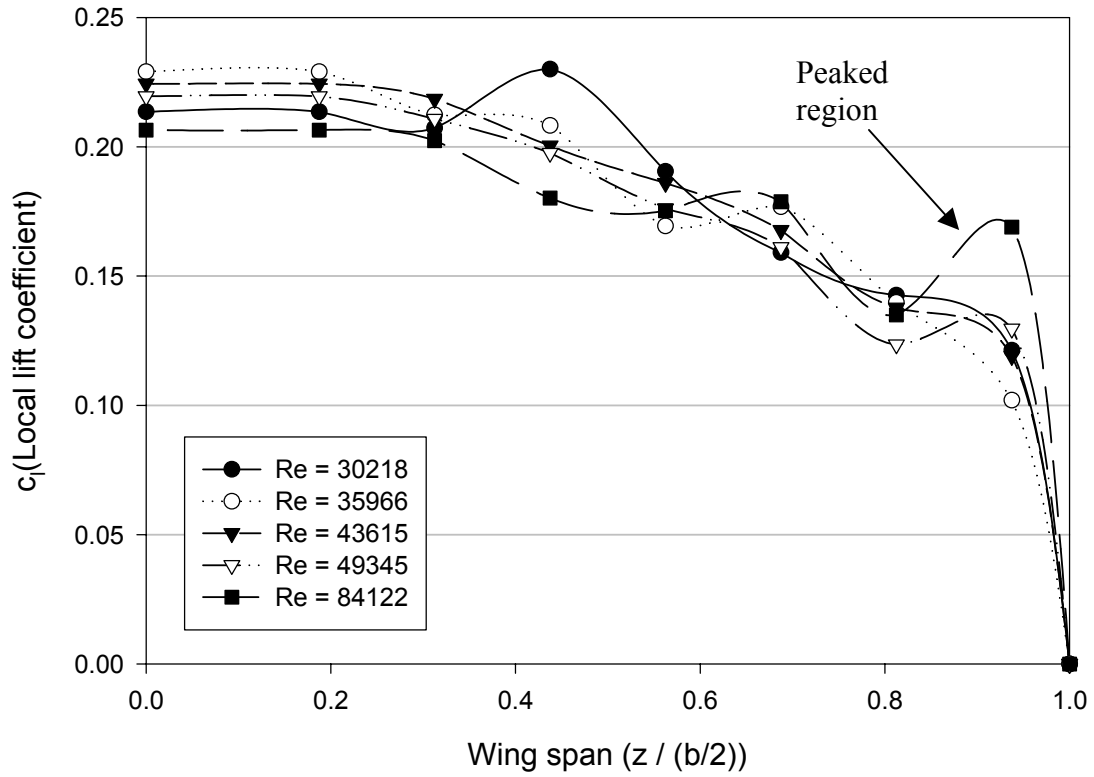


Figure 3.15 Local lift coefficient distribution for various Reynolds numbers at $\alpha = 6^\circ$, Spline curve fits through the data are shown.

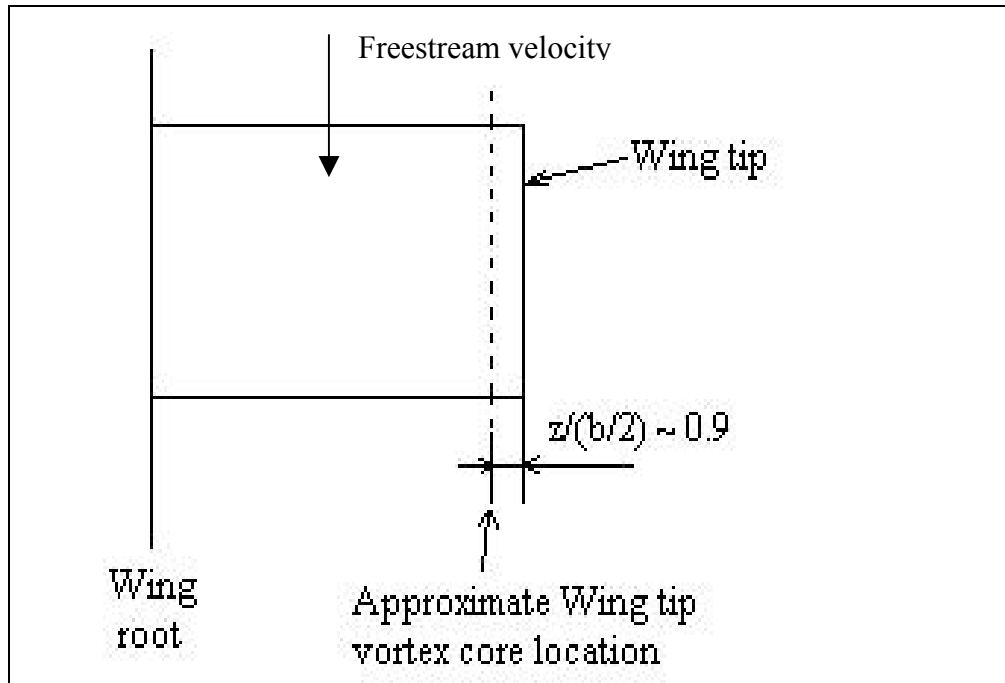


Fig 3.16. Approximate Wing tip vortex core location
(A semi-span wing is shown)

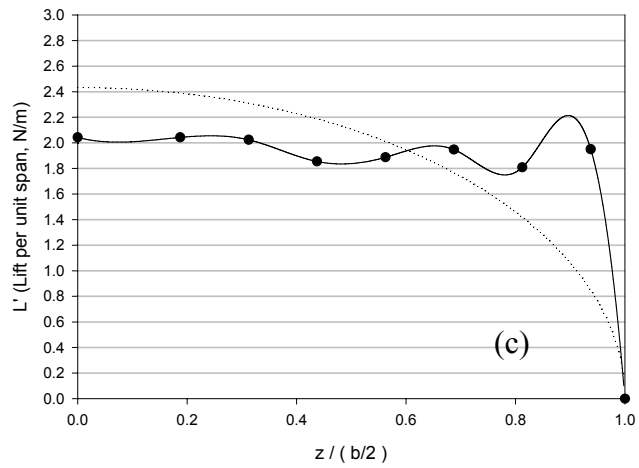
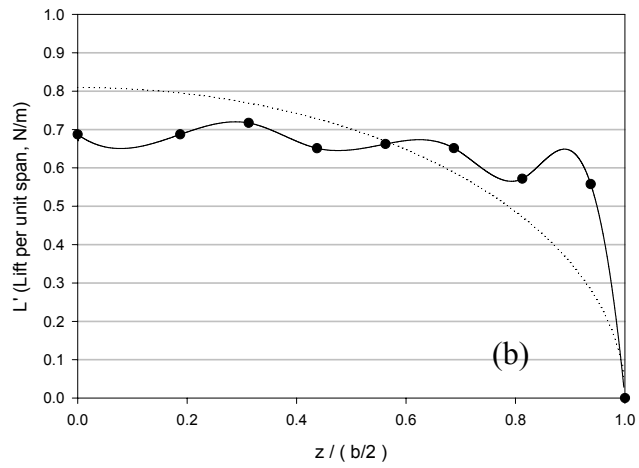
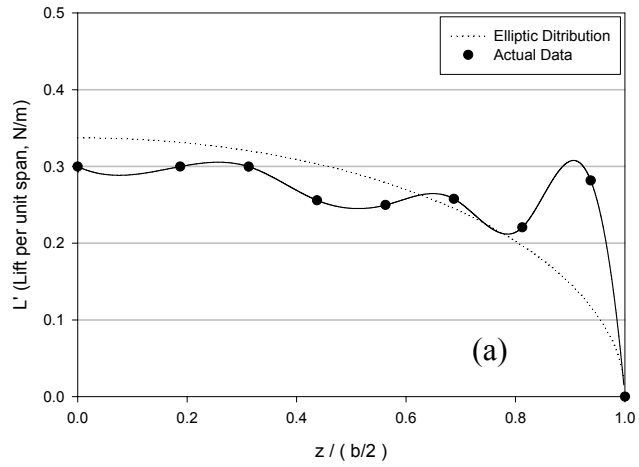


Figure 3.17 Local lift distribution at $\alpha = 15^\circ$; (a) $Re = 30218$, (b) $Re = 49345$, (c) $Re = 84122$

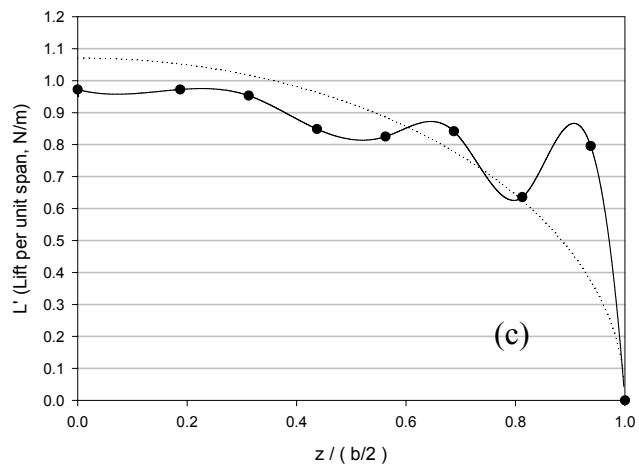
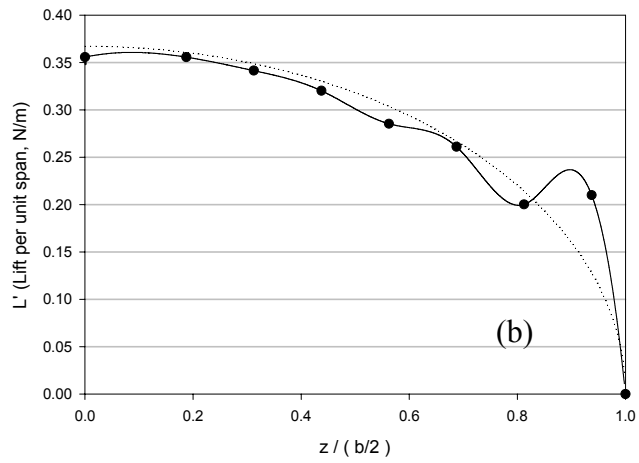
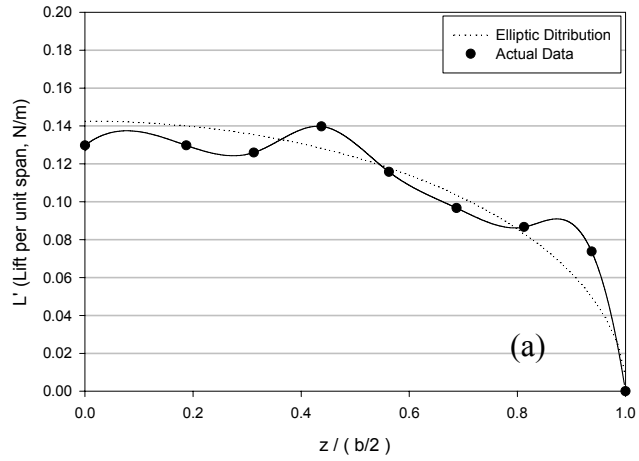


Figure 3.18 Local lift distribution at $\alpha = 6^\circ$; (a) $Re = 30218$, (b) $Re = 49345$, (c) $Re = 84122$

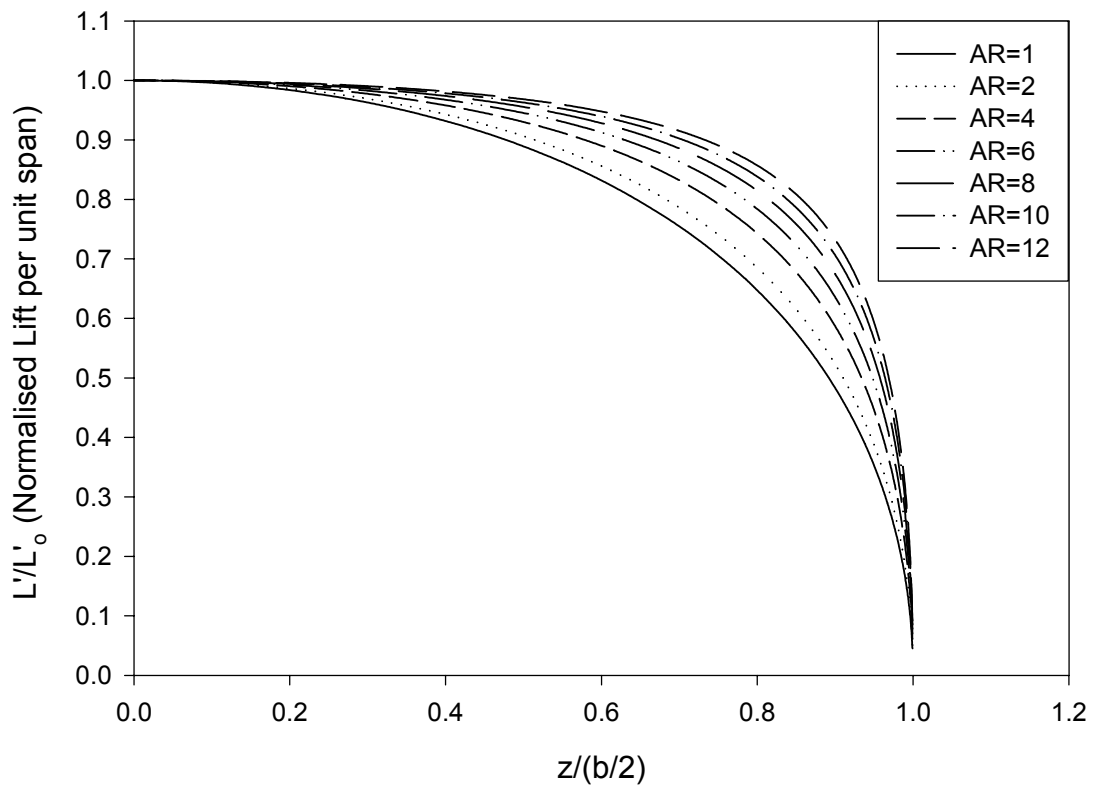


Fig. 3.19 Normalized lift distributions for Rectangular wings with varying AR.

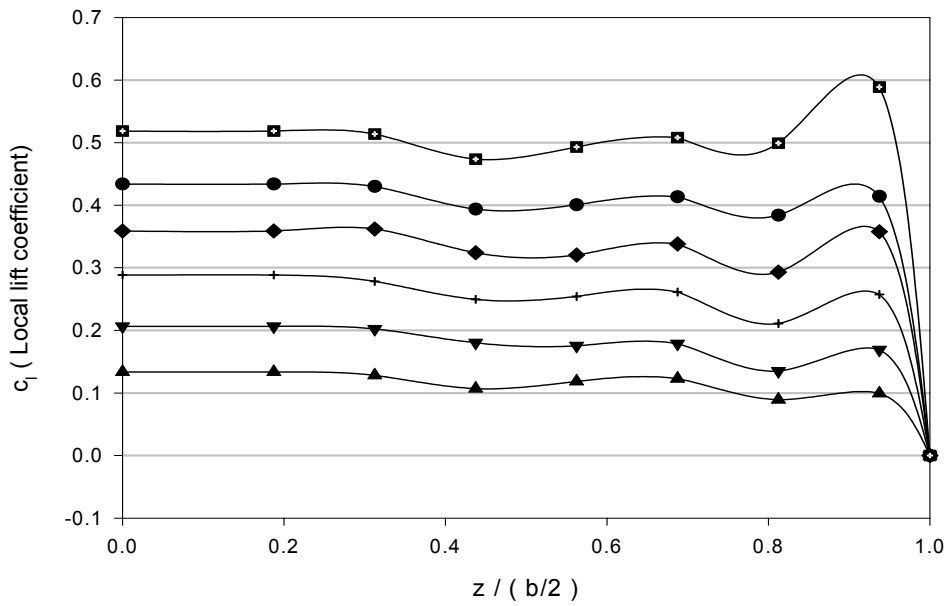
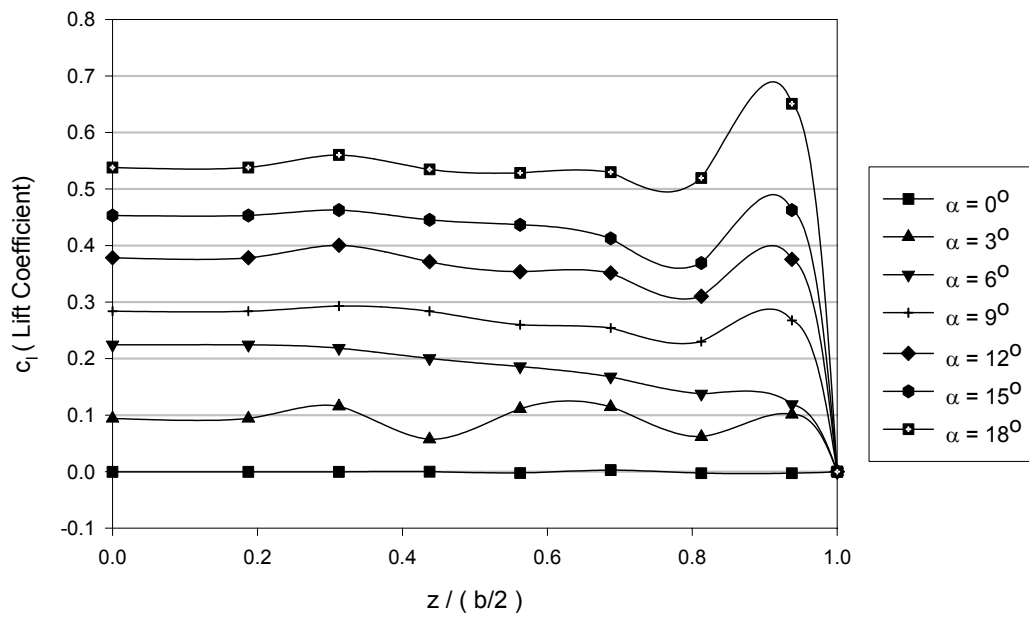


Figure 3.20 Local lift coefficient distribution for various angles of attacks, (a) $Re = 43615$, (b) $Re = 84122$

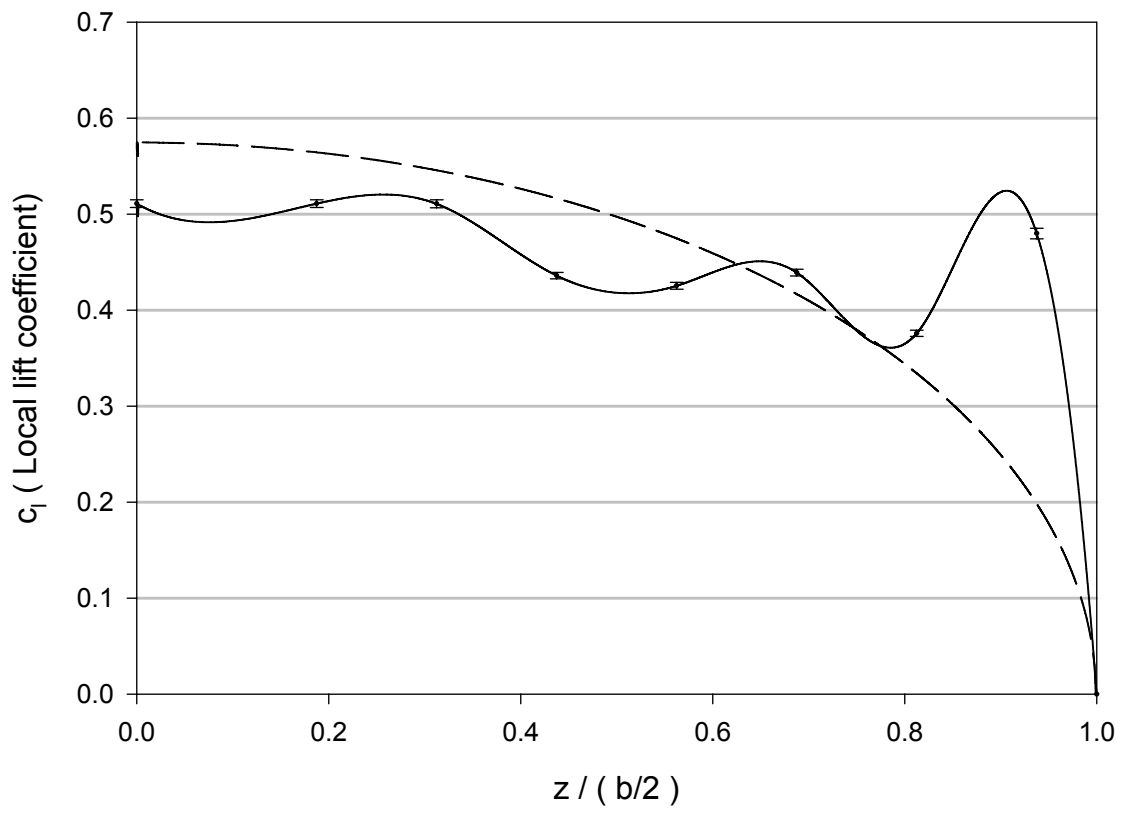


Figure 3.21 Local lift coefficient distribution for $Re = 30218$ at $\alpha = 15^\circ$, with error bars.

3.3 Fourier Coefficients

The Fourier coefficients introduced earlier in section 2.1 are important parameters for aerodynamic analysis. The span efficiency factor, which relates the induced drag with the lift on a wing, and the lift curve slope for a wing, both are a function of these Fourier coefficients. Applying the equations (11)-(15) in the Section 2.1 to the measured local lift coefficient data the Fourier coefficients were determined for full set of measurements.

$$c_l = \left(\int_0^1 (C_{pl} - C_{pu}) d\left(\frac{x}{c}\right) \right) \cos \alpha \quad (11)$$

$$L' = \frac{1}{2} \rho_\infty V_\infty^2 c(c_l) \quad (12)$$

$$\Gamma = \frac{L'}{\rho_\infty V_\infty} \quad (13)$$

$$\Gamma(\theta) = 2bV_\infty \sum_1^N A_n \sin n\theta \quad (14)$$

$$\theta = \cos^{-1} \left(-\frac{2z}{b} \right) \quad (15)$$

The equations are repeated here for the convenience. The Fourier coefficients are used to calculate the span efficiency factor and the lift curve slope from our pressure measurement for a rectangular wing, discussed in the next sections in details.

Equation (14) is solved as a system of simultaneous equations with ‘N’ unknowns, the unknown Fourier coefficients. The data for the spanwise lift distributions is known at only 7 locations along the span. To solve this system of linear equations we have plotted a spine fit curve through the measured data to determine local lifts at other intermediate locations. To solve equation (14), selective lift coefficient values locations along the span are used depending on the number of coefficients to be determined.

Glauert [26] suggests that the number of coefficients or the simultaneous equations considered depends on the accuracy of the solution expected. After a certain number of Fourier coefficients the value of successive coefficients decreases sharply in magnitude and small number of coefficients can fairly approximate the distribution. The analysis is based on this assumption and to analyze the number of coefficients to be considered, a test was carried out for the data at $Re = 43615$, $\alpha = 15^\circ$. The value of the span efficiency factor was calculated for varying number of coefficients using equation (20).

$$e = \frac{1}{\left[1 + \left(\sum_{n=2}^N n \left(\frac{A_n}{A_1} \right)^2 \right) \right]} \quad (20)$$

Fig 3.22a shows the change in calculated span efficiency factor with increase in the number of Fourier coefficients used for analysis. It can be clearly seen from this figure that the value of span efficiency factor remains fairly constant beyond $N = 10$. All the results described in the Section 3.4 and 3.5 are based on $N = 40$.

Fig 3.22b shows a plot of an assumed circulation distribution. This distribution is an artificial distribution obtained using pre-selected Fourier coefficients. Note that the artificial distribution was selected so that a peak occurred near the $z/(b/2) \sim 1$ similar to our measured lift distribution. The above-mentioned technique was used to determine the Fourier coefficients from this artificial distribution. The calculated results matched exactly with the expected results, thus confirming the validity of the procedure used for determining the Fourier coefficients. The procedure for calculating the span efficiency factor was applied for the elliptic lift distribution mentioned in Section 3.2. This was done to confirm as well establish the method used to calculate the span efficiency factors. As expected the span efficiency factor for the elliptical lift distribution was obtained to be

1 for all the Reynolds numbers. This ensured that the approach used for analysis of the lift distribution data to determine the Fourier coefficients was correct. A_n values for $Re = 43615$ and $Re = 84122$ at various angles of attack are shown in Appendix C.

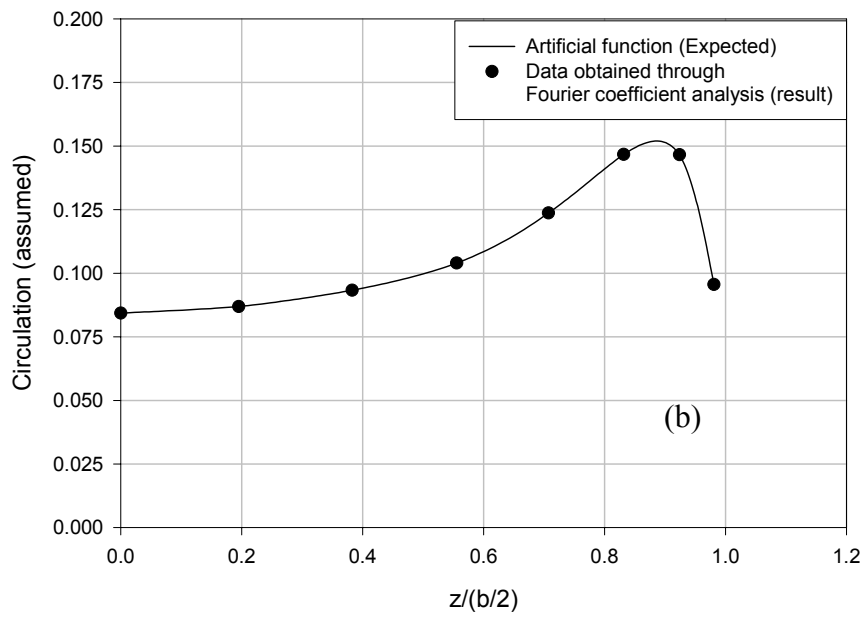
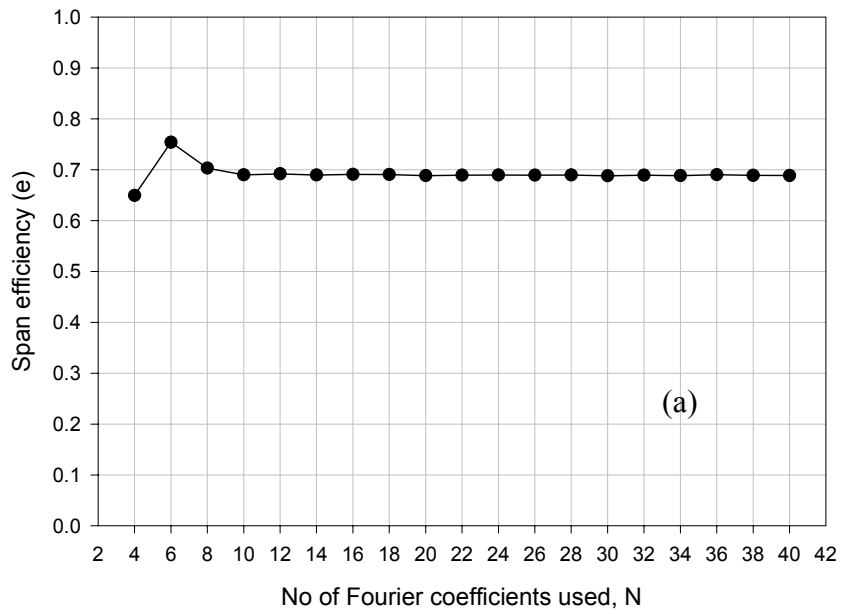


Figure 3.22 (a) Span efficiency factor vs No. of coefficients used for analysis.
 (b) Fourier coefficient calculation analysis confirmation plot

3.4 Span efficiency factor

Fig 3.23 shows the span efficiency factor plotted for various Reynolds numbers. As explained earlier in Section 2.1 the span efficiency can be calculated based on the measured lift distribution. The span efficiency factor is important for aerodynamic analysis because it affects the induced drag generated on the wing. The span efficiency factor is related with the induced drag through equation (20). The higher the span efficiency factor, the lower the induced drag.

The measured lift distribution was used to determine the Fourier coefficients for various Reynolds numbers at $\alpha = 6^\circ$ and $\alpha = 15^\circ$. These Fourier coefficients were used to calculate the span efficiency factor through equation (20) as:

$$e = \frac{1}{\left[1 + \left(\sum_2^N n \left(\frac{A_n}{A_1} \right)^2 \right) \right]} \quad (20)$$

We observe in Fig 3.23 that for both the angles of attack the span efficiency factor remains fairly constant for $Re < 45000$. For $Re \approx 45000$ the span efficiency factor suddenly increases for $\alpha = 15^\circ$. This can be associated with the reduction in peaked lift region in Fig 3.17 b. Comparing Figs 3.17-3.18 with the span efficiency factors obtained in Fig 3.23 we observe that as the deviation from the elliptic lift distribution increases the value of span efficiency factor reduces. The value of span efficiency factor for $Re = 30218$ and $Re = 84122$ are roughly same for $\alpha = 15^\circ$, but is higher for $Re = 49345$. Comparing this with Fig 3.17 we observe that the lift distributions for Fig 3.17a and Fig 3.17 c are similar, with more deviation from the elliptic curve than in Fig 3.17 b. This results in the variation in span efficiency factor demonstrated in Fig 3.23. This can be also observed for $\alpha = 6^\circ$ by comparing this with Figs 3.18 a-c. The span efficiency factor

is higher for $Re = 49345$ where the measured lift distributions are fairly close to the elliptic lift distribution. The further reduction in span efficiency factor for $Re = 84122$ at both the angles of attack in Fig 3.23 can be associated with large deviation from the elliptic distribution in Fig 3.17c and Fig 3.18c.

It can be seen in Fig 3.23 that value of the span efficiency ‘e’ roughly lies in the range of $0.6 < e < 0.95$. Torres and Mueller [17] have observed that the span efficiency factor for small aspect ratio wings is approximately $0.6-0.7$. They have carried out tests for $AR = 0.5, 1$ and 2 wings with various planform shapes at two Re 's, $Re = 7 \times 10^4$ and $Re = 10 \times 10^4$. All the models used by them were thin flat-plates. Our experimental results are found to be consistent with their results in the range of Reynolds numbers common between the two studies.

Fig 3.24 demonstrates the span efficiency factor for two Reynolds numbers at various angles of attack. It is observed that the span efficiency factor remains fairly constant for all angles of attack for $Re = 84122$. The dramatic drop in span efficiency factor for $\alpha = 3^\circ$ at $Re = 43615$ is due to a severely wavy (scalloped) lift distribution (see Fig 3.25). This distribution causes the lift distribution to deviate enormously from the elliptic lift distribution and the sudden drop in span efficiency factor occurs. The physical reasons for this ‘waviness’ of the lift distribution in Fig 3.25 are not understood at present and require further study. As seen in Fig 3.25b the measured lift distribution is fairly close to the elliptic distribution, which results in increase in the span efficiency factor in Fig 3.24 to near $e = 1$ at $\alpha = 3^\circ$. The lift peak near the wing tip is also less prominent for this Reynolds number-angle of attack combination.

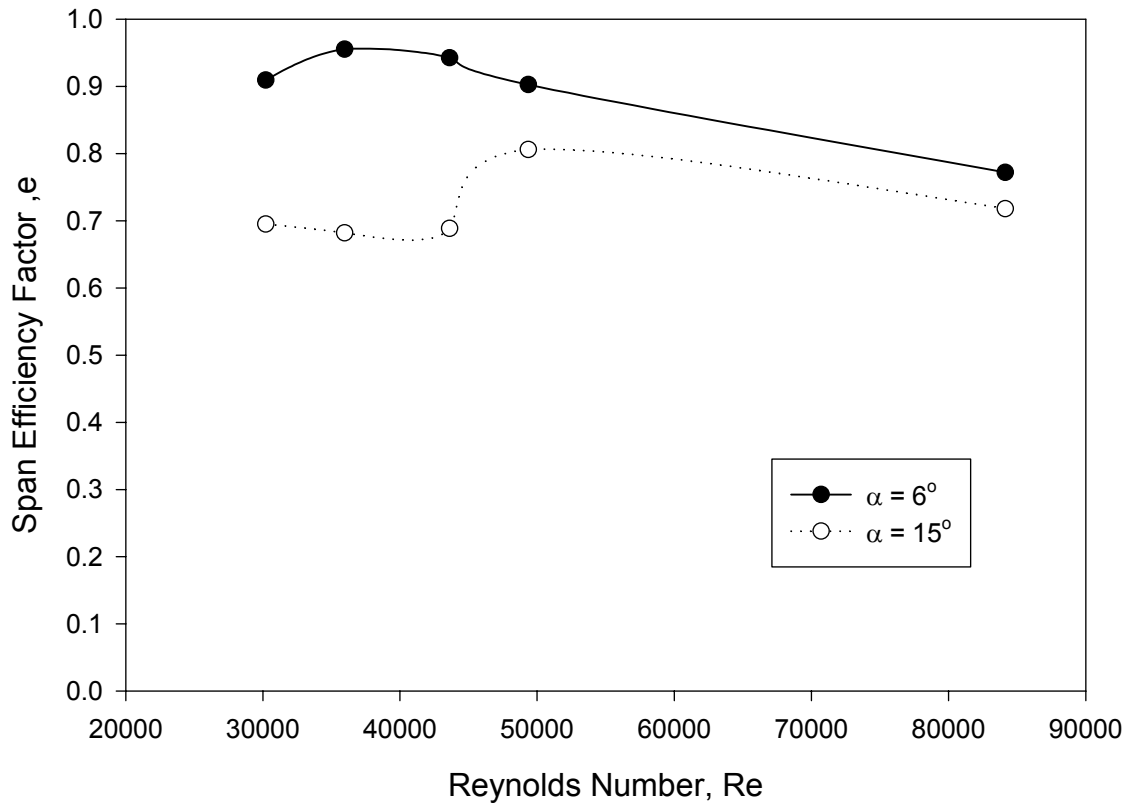


Figure 3.23 Variation of span efficiency factor with Reynolds number
 $e = 1$ for elliptic wing
 $e = 0.9969$ for AR =1 rectangular wing

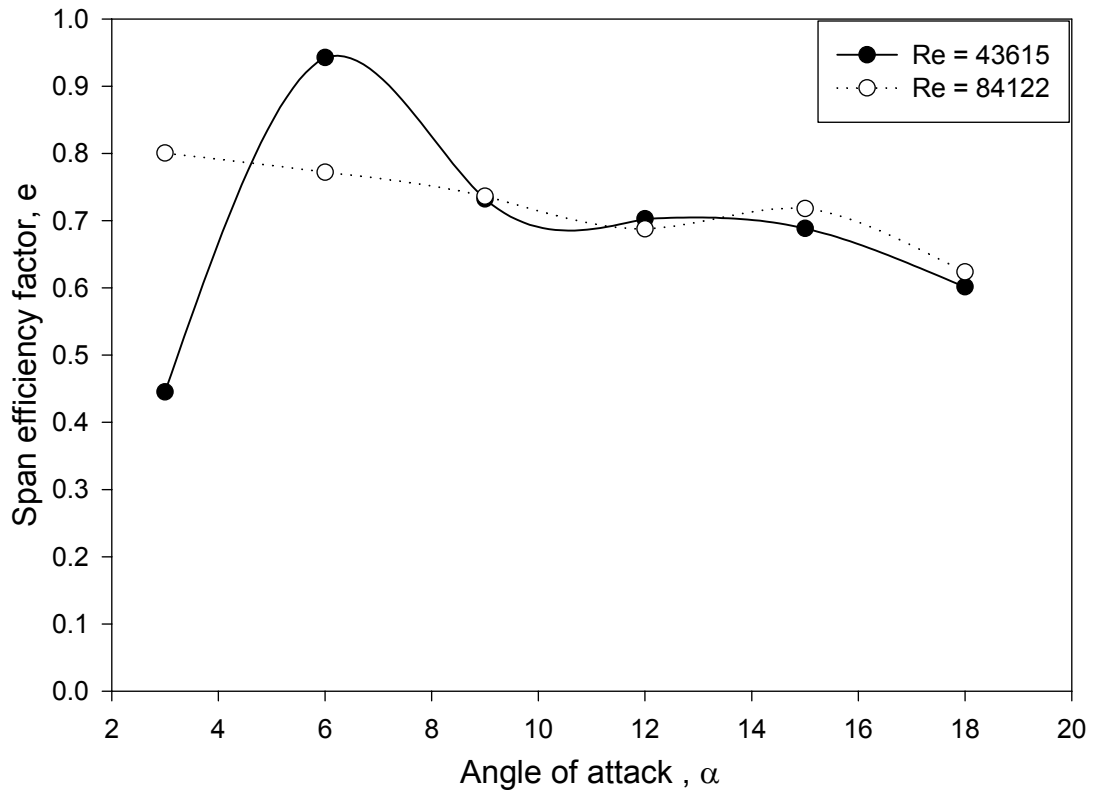


Figure 3.24 Variation of span efficiency factor with angle of attack

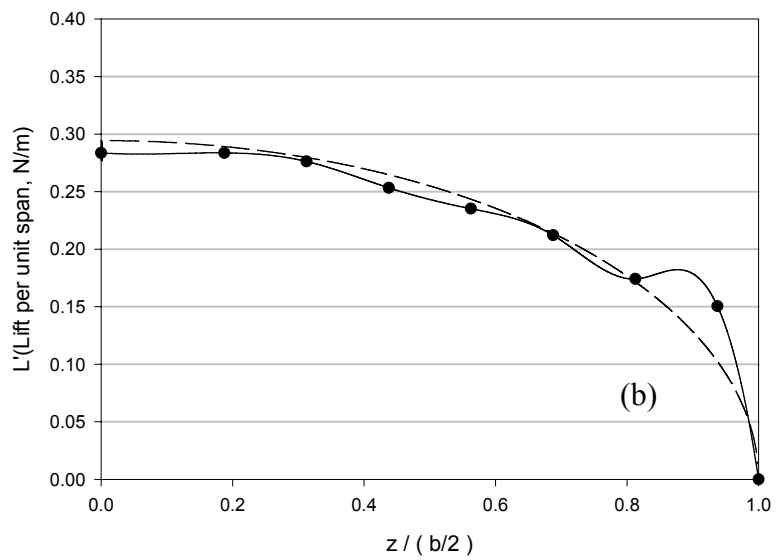
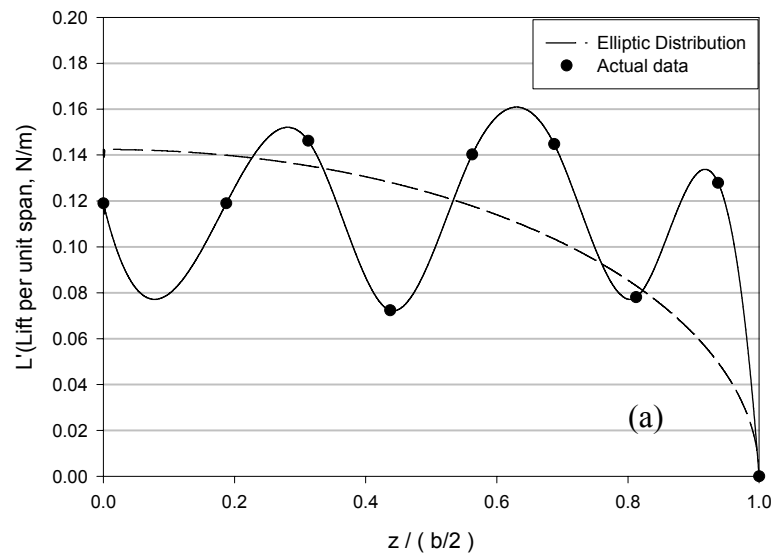


Fig 3.25 Spanwise lift distribution for $Re = 43615$; (a) $\alpha = 3^\circ$, (b) $\alpha = 6^\circ$

3.5 Lift coefficient curve vs angle of attack

Figs. 3.26 and 3.27 plot the measured lift coefficients (from pressure measurements) vs angle of attack for $Re = 43615$ and $Re = 84122$. The integration of area under the curve for spanwise lift coefficient plots yields the total lift coefficient at each angle of attack. This is calculated for all the measured angles and a plot of lift coefficient versus angle of attack curve is obtained.

Figs 3.26 and 3.27 also plot the predicted lift coefficient curves for an elliptic wing with $AR = 1$ as well as a theoretical slope for $AR = 1$ wing with rectangular planform shape. The lift curve slope for elliptic wing was calculated based on equation (21). The theoretical slope for a wing with rectangular planform is based on equation (22). The equation for the general planform shape wing includes the factor ' τ ' which is based on the first coefficient in the Fourier series discussed earlier. This slope was determined by calculation of τ from A_1 obtained from the lift distribution for a rectangular wing. Figs 3.26 and 3.27 also show the linear regression fit through the measured data. This was done to calculate the slope of the measured lift coefficient curve.

The lift curve slope for an elliptic wing is higher than obtained for the measured data. This is consistent with the theory that the lift curve slope for a wing with planform shape other than elliptic would be less than that for an elliptic wing. This lift curve for the elliptic wing is based on equation (21) and not on the lift coefficients obtained from the elliptic lift distributions used earlier for comparison with the measured local lift distributions in Fig. 3.17, 3.18 for example. This is done because a lift curve obtained from the assumed elliptical lift distributions (in Fig. 3.17 and 3.18) would match exactly with those obtained from pressure measurements as the elliptical lift distributions

were obtained by maintaining the same total lift coefficients (or area under the curves). The Figs 3.26 and 3.27 also show the lift curve for an $AR = 1$ rectangular wing. This lift curve is slightly lower than that of the elliptic but also higher than that obtained from the pressure data as discussed previously. The deviation of the measured lift values from the elliptic lift values increases with increasing angle of attack.

It is also seen from these figures that the wing has not stalled up to $\alpha = 18^\circ$ indicating that the angle of attack for stall for low AR wings at low Reynolds numbers is much higher than for larger AR wings at high Reynolds numbers. Torres & Mueller [17] have also observed that for $AR = 1$ wing at $Re = 7 \times 10^4$ and $Re = 10 \times 10^4$ the wing does not stall until as high as $\alpha = 25^\circ$.

Fig. 3.26 also shows the lift curve slope obtained from lift measurements using the force balance set-up explained earlier in section 2.2. The measurements were carried out for $0^\circ \leq \alpha \leq 14^\circ$. The low weight of the wing and frame results in vibrations of the frame at higher angles of attack and high Reynolds numbers. This limits the maximum angle of attack at which measurements can be taken. The lift curve slope obtained from the force balance measurements is found to be slightly higher than that obtained by the pressure measurement tests. We observe in Fig. 3.27 that this deviation is more for $Re = 84122$. However in both the figures it can be observed that the actual data points obtained through lift measurements lie close to that obtained by the pressure measurements. The slope for these lift measurements is obtained by a linear regression fit through the data. This might result in the difference between the slopes obtained from the pressure measurements and the lift measurements. The last two data points in Fig 3.27 plotted from the lift measurements for $\alpha = 11.8^\circ$ and $\alpha = 14^\circ$, are drastically different from the

lift curve obtained from pressure measurements. These values were obtained with the set-up experiencing the large vibrations mentioned earlier. These values are not considered when calculating the lift curve slope for force balance measurement curve.

This difference in the slopes might also be associated with the errors in the lift coefficient calculation from the pressure data as well as the error in lift readings in the weighing balance set-up. The overall agreement between lift coefficient curves obtained from the pressure and force balance measurements provides validation of the results from the pressure measurement technique.

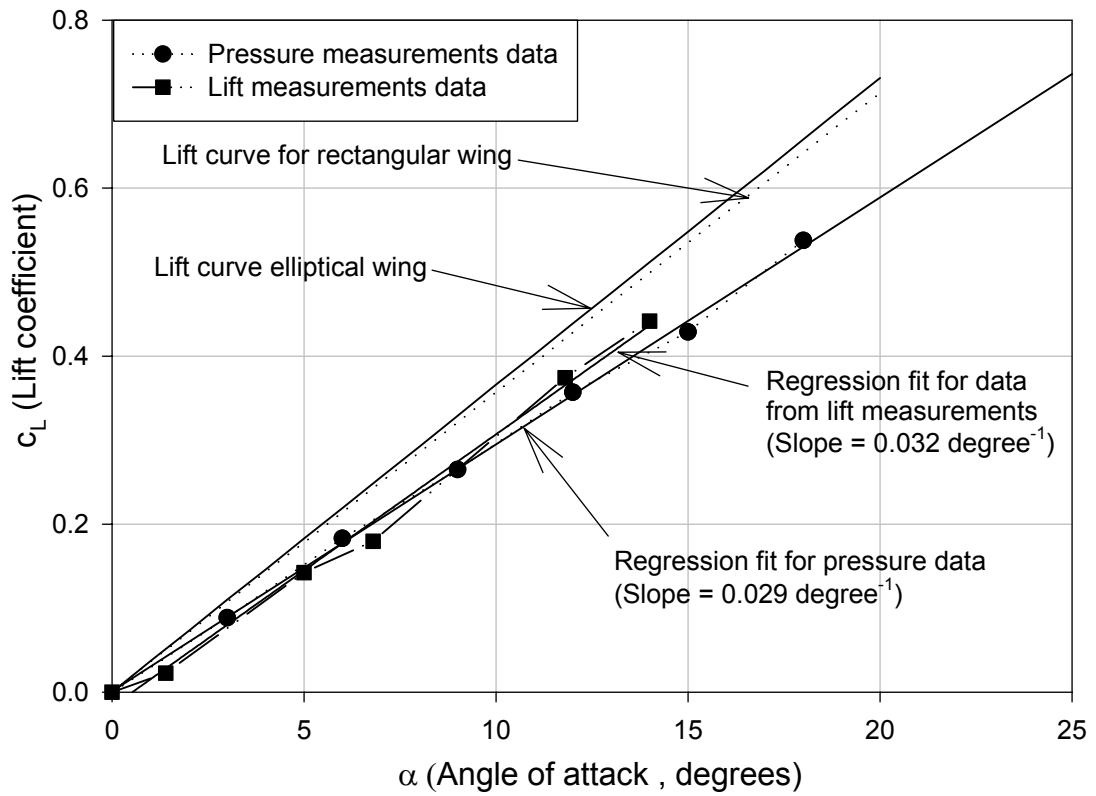


Figure 3.26 Lift vs angle of attack curve at $Re = 43615$

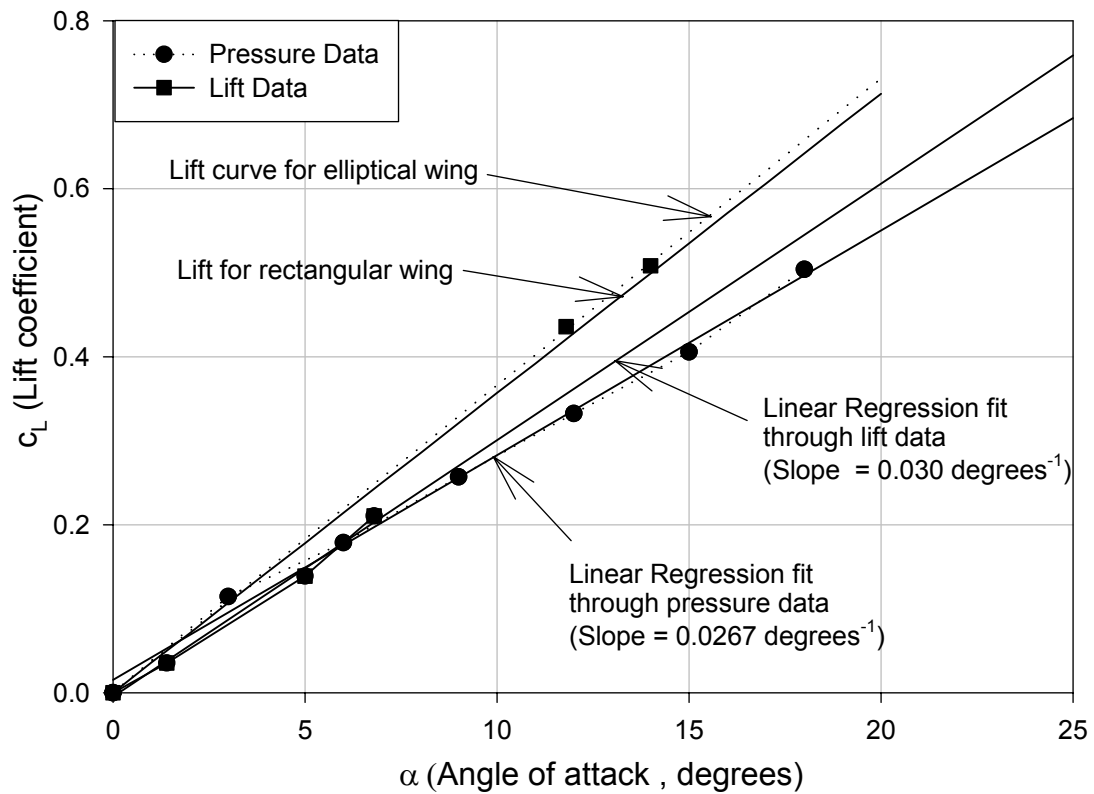


Figure 3.27 Lift vs angle of attack curve at $Re = 84122$
 Lift curve slope for lift data based on data for $0^\circ < \alpha < 8^\circ$ due to experimental uncertainty
 at higher angles of attack

3.6 Induced drag coefficients

Fig. 3.28a shows the induced drag coefficient for various Reynolds numbers at varying angles of attack. The plot shows induced drag coefficients obtained from pressure measurements at two Reynolds numbers and for a rectangular wing with $AR = 1$ predicted by the Prandtl's lifting line theory. All the 'measured' induced drag coefficients are based on equation (19) where ' C_L ' values are from the pressure measurements and ' e ' values are from the Fourier coefficient analysis. The induced drag coefficients for the rectangular wing with $AR = 1$ are using equations (19) and (21). The measured induced drag coefficients show a quadratic trend with α (or C_L , since α is proportional to C_L).

Comparing the curves for $Re = 43615$ and $Re = 84122$ with that obtained for the Rectangular wing, we observe that their values match fairly well. The closeness of values of the induced drag coefficient for rectangular wing with those calculated for $Re = 43615$ (for e.g. $\alpha = 9^\circ$ and $\alpha = 12^\circ$), can be explained on the basis of the relation between the C_L and e values from Fig. 3.24 and 3.26. The values for C_L 's from the pressure measurements is approximately 16% less than those predicted for a rectangular wing with $AR = 1$ and the span efficiency factors are approximately 30% less than the ' e ' value for the rectangular wing. As an effect of equation (19) this reduction in C_L 's is nullified by the reduction in e values and the induced drag coefficients from the pressure measurements and those predicted for rectangular wing match closely. However this match may not always occur for all flow cases.

Fig. 3.28 b shows the comparison between induced drag coefficients at $Re = 84122$ with the total drag coefficients obtained by Torres and Mueller [17] in their study on a Rectangular wing with $AR = 1$ at $Re = 70000$. This is just a qualitative comparison

to demonstrate the correctness in the variation of measured induced drag coefficients. Although this comparison is at two different Reynolds numbers, the similarity between trends followed by the measured induced drag coefficient with those observed by Torres and Mueller help the observations made with the pressure measurement technique.

Fig 3.9 shows the induced drag coefficients at $\alpha = 6^\circ$ and $\alpha = 15^\circ$ at various Reynolds numbers. From the curve for $\alpha = 6^\circ$ we observe that the induced drag coefficient remains fairly constant in the full range of Reynolds number under consideration, indicating that induced drag coefficient at low angle of attack is approximately same over a wide range of Reynolds number. Whereas for $\alpha = 15^\circ$ we observe that this induced drag coefficient varies drastically around $Re = 45,000$. It remains fairly constant for $Re \leq 43615$ but decreases sharply after that. This increase in the induced drag coefficients by up to 50% may have implications in MAV design as MAV's become smaller and smaller, thus reducing Reynolds numbers into the range $Re < 45000$.

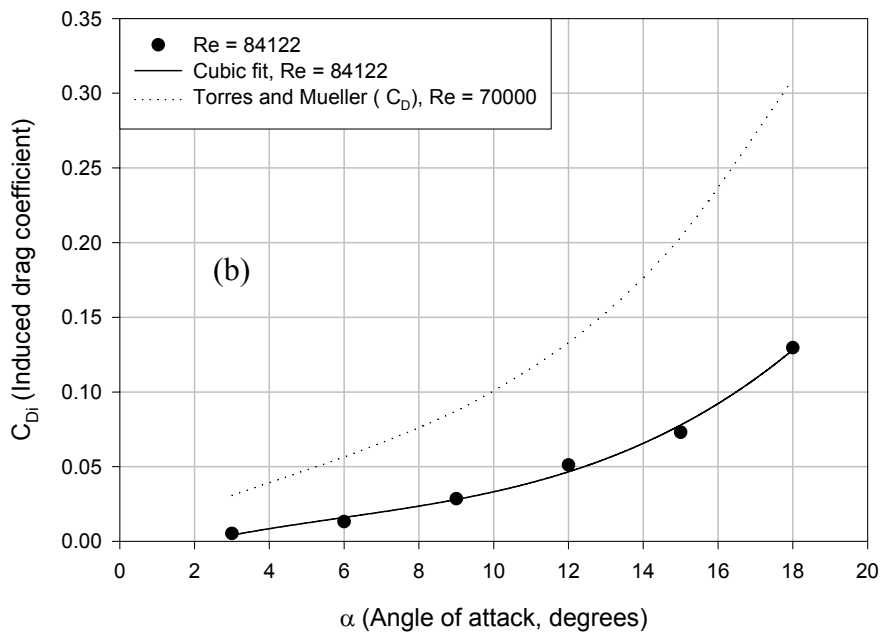
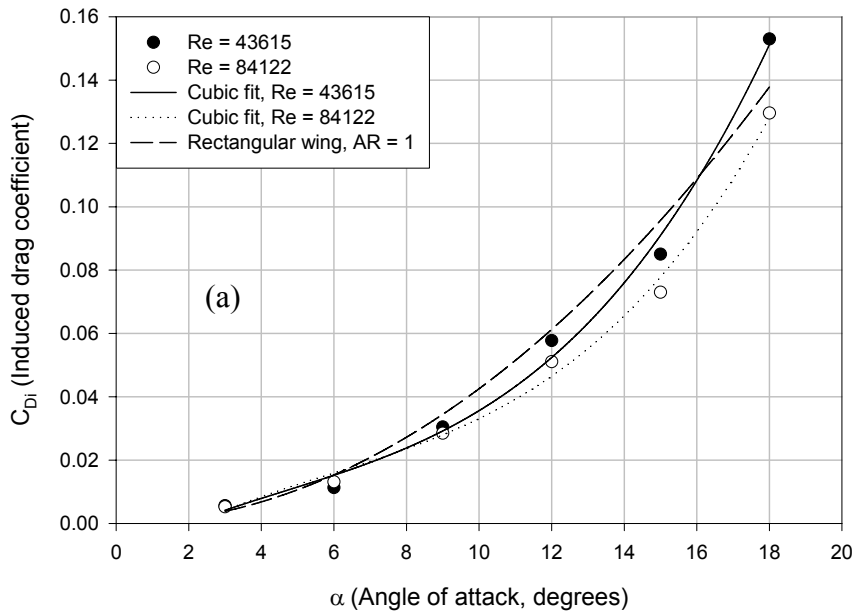


Fig. 3.28 Induced drag coefficients (a) With varying α
 (b) Comparison with Torres and Mueller data

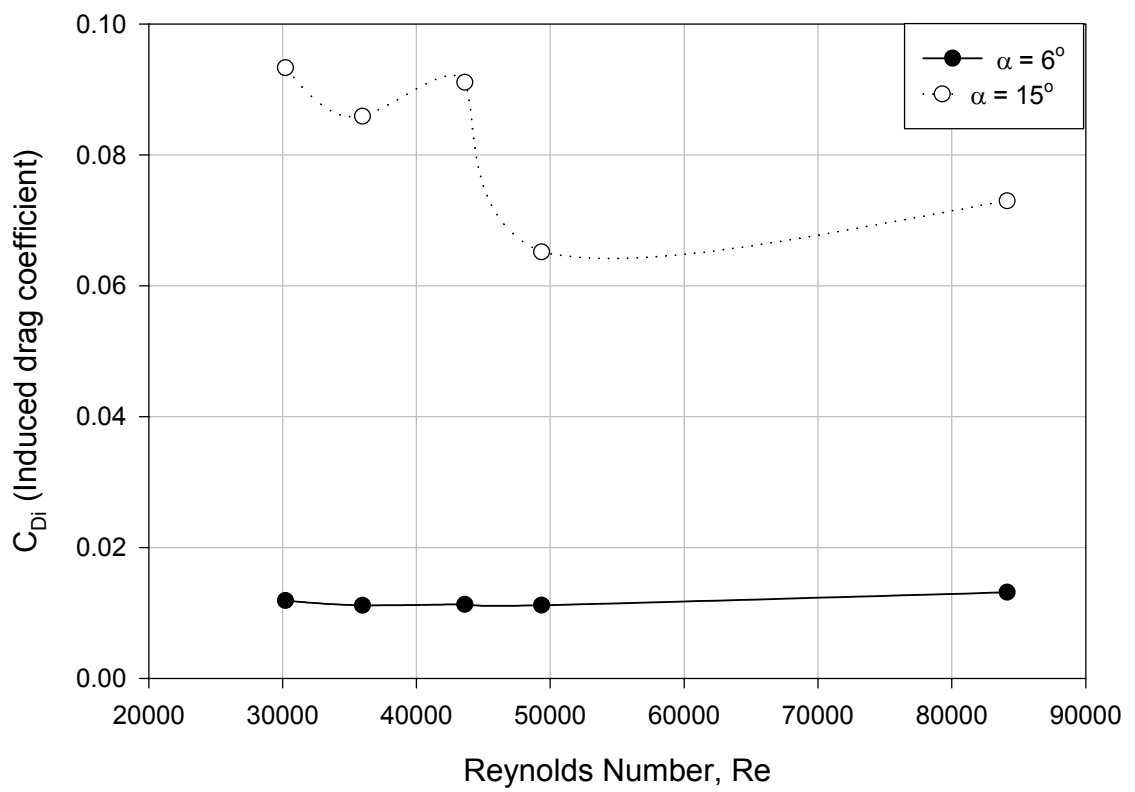


Fig. 3.29 Induced drag coefficients with varying Reynolds number

4. Conclusion

An experimental research for a low AR wing at low Reynolds number was carried out. The model wing with NACA 0012 airfoil shape, $AR = 1$, $c = 0.2032\text{ m}$ was used. Tests were carried out in the Reynolds number range $3 \times 10^4 < Re < 8.5 \times 10^4$. Tests included pressure measurements at various span wise locations to obtain a coefficient of pressure distribution along the chord length. Integration of the pressure coefficient data provided the local lift coefficients at various spanwise locations. Lift coefficients thus obtained were further analyzed to obtain the span efficiency factors for various Reynolds number-angle of attack combinations. The lift curve slopes at two Reynolds numbers were determined.

The pressure distributions obtained show a large reduction in pressure on the upper surface of the wing near the wing tip. The separation phenomenon, common to low Reynolds number flows, was clearly observed at angles of attack above 6° . The separation bubble formed on the upper surface of the wing was found to produce a plateau region in the pressure coefficient plots. This plateau region disappeared for the pressure coefficient plot near the wing tip indicating that no separation was present at the wing tip. This observations match favorably with the flow visualization obtained by Torres and Mueller [17] in their research carried on low AR wings at low Reynolds numbers. The separation plateau was found to increase in size with increasing angle of attack, consistent with classic separation theory.

The pressure distributions were integrated over the chord length to obtain the local lift coefficients at various spanwise locations. The spanwise distributions prominently showed a peaked lift distribution near the wing tip. This increase in lift was found at

$z/(b/2) \approx 0.9$ in the local lift distribution plots. This result is consistent with the observation made by Torres and Mueller [17] and Desabrais and Johari [20] in their research. Torres and Mueller suggest that the wing tip vortices energize the flow and result in low-pressure cells on the upper surface of the wing. Desabrais and Johari have observed the location of core of the wing tip vortices at approximately this location. We surmise that the high velocity core region induces this low-pressure region on the upper surface near the wing tip.

The local lift distributions were compared with appropriate elliptical lift distribution. This elliptical lift distribution was obtained by maintaining the total lift coefficient for this distribution same as that obtained for the lift distributions obtained from the pressure distributions. The elliptical distribution was used for two principal reasons. First, the elliptical lift distribution generates the lowest induced drag, ensuring optimum aerodynamic performance for a wing. Secondly the lift distribution on a rectangular planform wing approaches elliptic lift distribution as AR goes to zero. For the $AR = 1$ wing used in the present study value of span efficiency was obtained to be $e = 0.9969$, so that the elliptic lift distribution approximates the lift distribution on a rectangular wing planform very well. Hence accordingly elliptic lift distribution was used for comparison.

The span efficiency factor was obtained from the local lift distributions. A Fourier sine series approximation was used to find the Fourier coefficients based on the lift distributions. These Fourier coefficients were used to obtain the span efficiency factors at various Reynolds numbers and angles of attack. The variation of span efficiency factor indicated that any deviation of the measured lift distributions from the elliptic lift distribution resulted in a decrease in the span efficiency factor. The span efficiency for

elliptic distribution was found to be 1. The span efficiency factor was found to be in the range $0.6 < e < 0.9$, which matches with the range of span efficiency factors obtained by Torres and Mueller [17]. These results are also consistent with finite wing theory, which shows that lift distribution deviating from the elliptic distribution have span efficiency factors less than 1. The variation of span efficiency factor with Reynolds number and angles of attack was found to be consistent with the details of lift distribution curves. The presences of a peaked lift region near the wing tip on a low AR wing at low Reynolds number contributes significantly to the observed reduction in span efficiency factors and hence increase in the induced drag.

The lift curve was plotted for two different Reynolds numbers. Results obtained were close to that predicted by the theory, although not exact. The theoretical lift curve slope for the elliptic wing is higher than that for the $AR = 1$ rectangular wing. Both these slopes were found to be higher than the lift curve slope obtained from the measured spanwise pressure coefficients. The lift curve slope for pressure data and force balance data was approximately $(dC_L/d\alpha) \sim 0.03$ per degree. The predicted slope for a Rectangular wing with $AR = 1$ was $(dC_L/d\alpha) \sim 0.035$. The lift curve obtained from the pressure data has a lower slope because of the deviation of the lift distributions from the elliptic lift distributions. To obtain an overall physical validation of the pressure measurements and integration approach, lift measurements were carried out on another $AR = 1$, NACA 0012 wing using a force balance set-up. Although data over full range of Reynolds numbers and angles of attack was not obtained the lift coefficients determined using the force balance closely match with those obtained from the pressure measurements

Main general Conclusions:

For low AR wings in the $3 \times 10^4 \leq Re \leq 8.5 \times 10^4$ range:

- Measured local lift distributions deviate significantly from the elliptic lift distributions predicted by finite wing theory.
- As a result we conclude that finite wing theory cannot accurately predict
 - Total lift coefficient, c_L
 - Span efficiency factor, e
 - Induced drag coefficient, C_{di}
- Measurement of local lift distributions is necessary to accurately predict these aerodynamic performance parameters through
 - Integration of local c_l distributions to obtain c_L
 - Determination of Fourier coefficients, A_n 's, to obtain the span efficiency factor, e , hence the induced drag coefficient C_{di} .

5. Suggestions for Future Work

The peaked lift near the wing tip needs to be understood in more detail. More detailed physical mechanisms that determine how the wing tip vortices ‘energize’ the boundary layer need to be described. The pressure coefficients can also be used to obtain the quarter chord moment coefficients, the location of center of pressure and other aerodynamic parameters based on pressure distributions. So the basic idea of pressure measurements can be extended to obtain various parameters important for the aerodynamic performance of a wing.

The deviation of the lift distributions from those obtained for the elliptical lift distributions suggest possible modifications to the wing planform shape in order to obtain an elliptic lift distribution. Based on local lift distributions obtained in this thesis, modifications could be made to a rectangular planform wing so as to reduce lift in the areas of peaked lift and increase it in the central span region, where the measured lift is lower than the optimal elliptic distribution. Fig 5.1 b suggests possible changes to a wing chord distribution to obtain an elliptic lift distribution. Other ways of achieving the same result is by adding wash-out in regions of lower lift and introducing wash-in where the lift is higher than the elliptic lift distribution.

Yuan [19] during his study on thin flat plates in the low Reynolds number range has observed a peaked lift distribution, approximately at $z/(b/2) = 0.6$. If the chord length is reduced in this region of peaked lift to reduce the lift to an elliptic lift distribution, the reduced chord will appear as a notch in the thin wing (flat plate). This resembles to trailing edge notches observed on bird wings such as seagulls, pheasants, approximately at the same location where Yuan [19] has observed the peaked lift region. The method of

pressure measurements should be extended to thin flat plates to confirm these peaked lift distributions.

Determination of an optimal wing planform shape could help in improving MAV lift-drag ratios and the overall performance. Pressure measurements, with set-up similar to discussed in this research, at higher Reynolds numbers would determine the Reynolds number range where the deviation from the elliptic lift distributions disappear. Overall, further study of local lift distributions is recommended for effective design of the Micro air vehicles in the future.

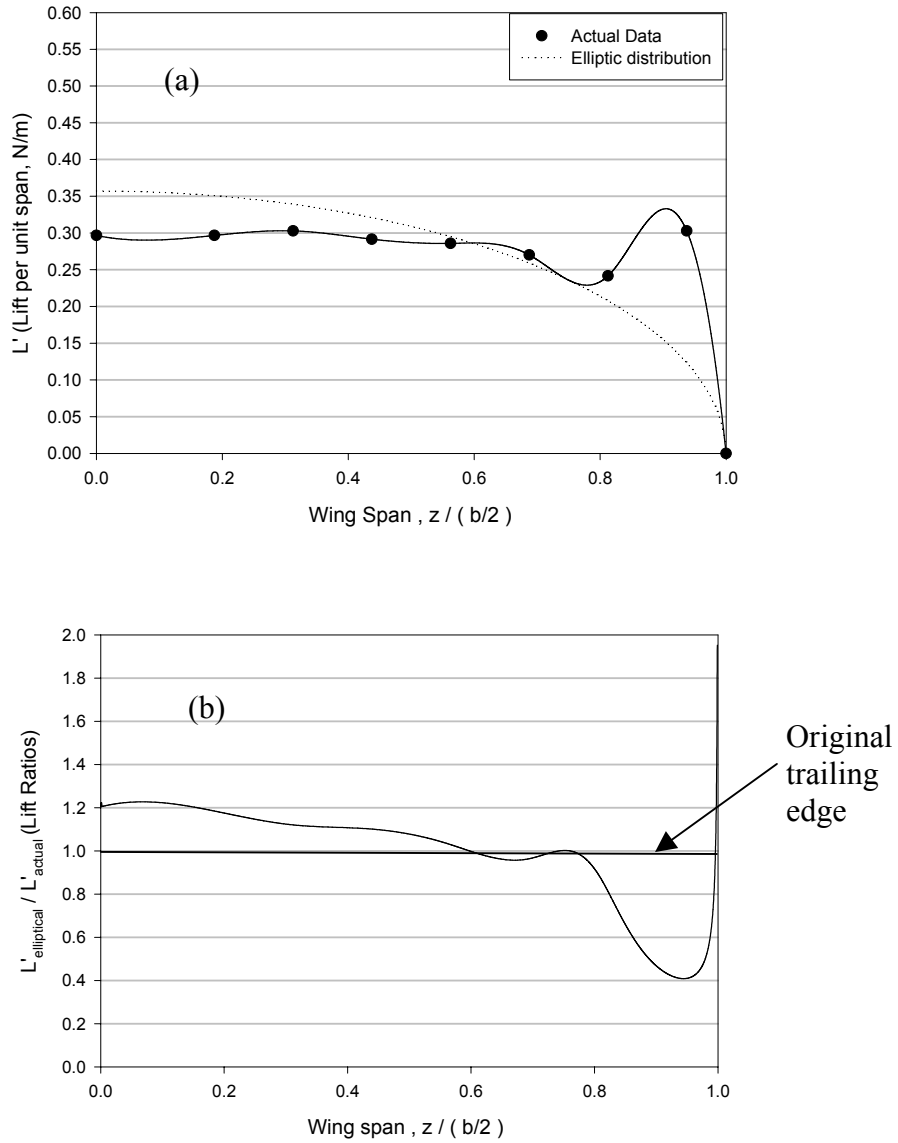


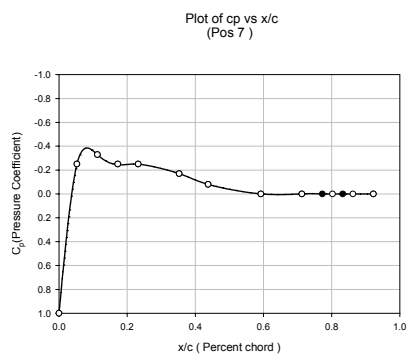
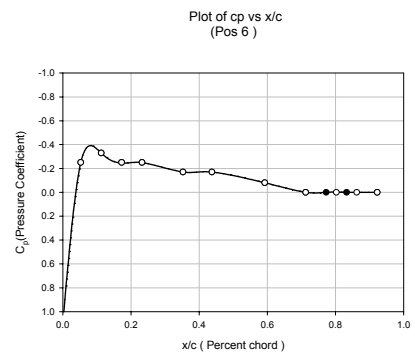
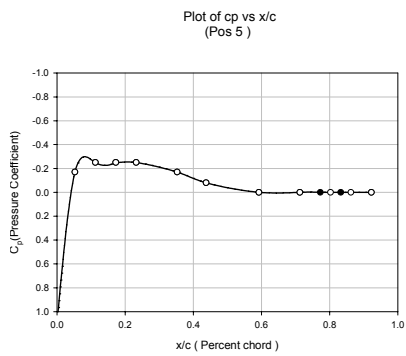
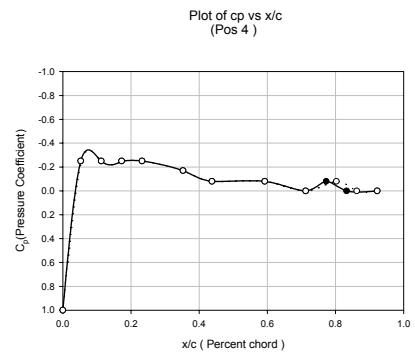
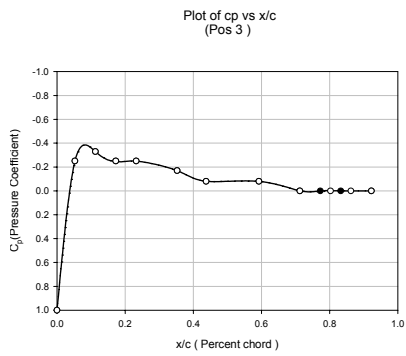
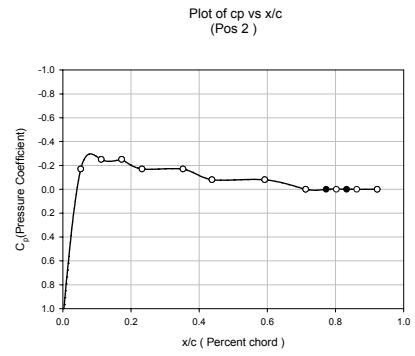
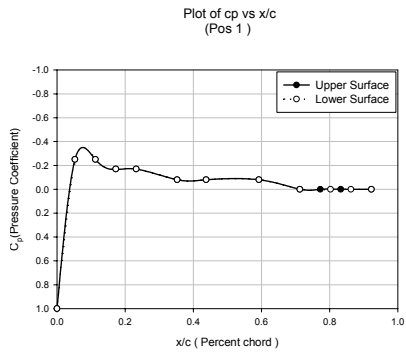
Fig. 5.1 (a) Comparison of measured lift distributions to elliptic lift distributions at $Re = 43615$, $\alpha = 15$; (b) Adjusted chord distributions.

References:

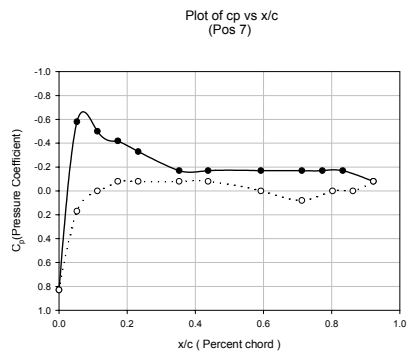
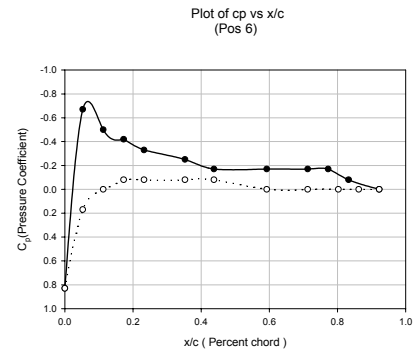
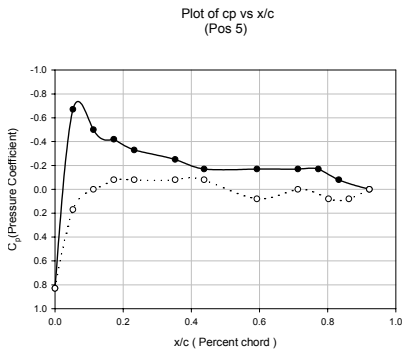
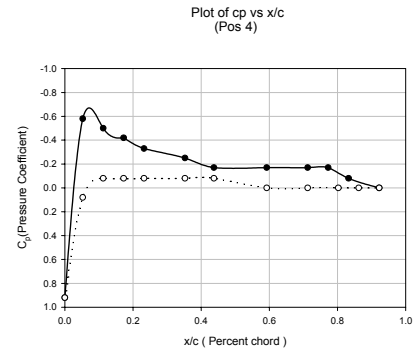
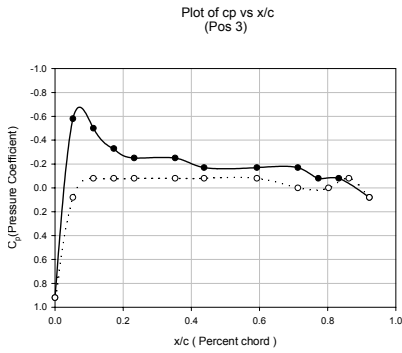
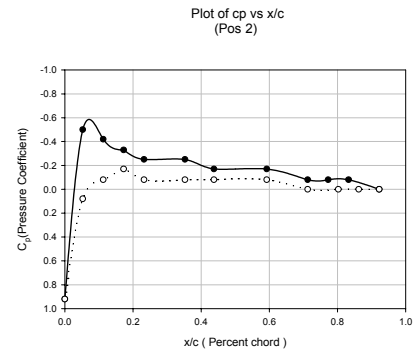
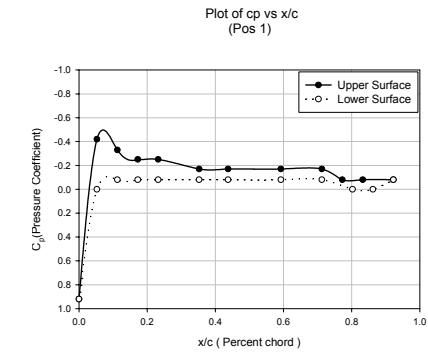
- [1] Kunz, P. J. and Kroo, I., "Analysis and design of Aerofoils for use at ultra low Reynolds numbers", *Progress in Astronautics and Aeronautics*, (edited by Thomas J. Mueller), Vol. 195, pp. 35-60, 2001.
- [2] Selig, M. et al. "Systematic airfoil design studies at Low Reynolds numbers," *Progress in Astronautics and Aeronautics*, (edited by Thomas J. Mueller), Vol. 195, pp. 143-167, 2001.
- [3] Mönntinen et. al. "Adaptive unstructured meshes for solving the Navier-Stokes equations for Low-Chord-Reynolds-Number flows", *Progress in Astronautics and Aeronautics*, (edited by Thomas J. Mueller), Vol. 195, pp. 61-80, 2001.
- [4] Carmichael, B. H., "Low Reynolds number airfoil survey", Volume 1, NASA Contractor Report 165803, November 1981.
- [5] Gad-el-Hak, M., "Micro-air-vehicles: Can they be controlled better", *Journal of Aircraft*, Vol 38, No 3, pp. 419 – 429, June 2001.
- [6] McCullough, G.B. and Gault, D.E., "Examples of three representative types of airfoil-section stall at low speed", NACA TN 2502, Sept. 1951.
- [7] Broeren, A.P. and Bragg, M.B., "Unsteady stalling characteristics of thin airfoils at low reynolds number", *Progress in Astronautics and Aeronautics*, (edited by Thomas J. Mueller), Vol. 195, pp. 191 – 213, 2001.
- [8] Polhamus, E.C. "Predictions of vortex-lift characteristics by a leading-edge suction analogy," *Journal of Aircraft*, Vol. 8, pp. 193-199, 1971.
- [9] Rajan, S.C. and Shashidhar, S. "Exact leading-term solution for low aspect ratio wings," *Journal of Aircraft*, Vol. 34, pp. 571-573, 1997.
- [10] Polhamus, E.C. "A concept of the vortex lift of sharp-edge delta wings based on a leading-edge-suction analogy," *NASA TN D-3767*, 1966.
- [11] Schlichting, H., *Aerodynamics of the airplane*, Mc-Graw-Hill International Book company, pp. 143-161, 1979.
- [12] Hoerner, S.F., Fluid Dynamic Drag, Hoerner Fluid Dynamics, Brick Town, NJ, pp. 7.16-7.21, 1965.
- [13] Hoerner, S.F. and Borst, H.V., Fluid Dynamic Lift, Hoerner Fluid Dynamics, Brick Town, NJ, pp. 17.1-17.15, 1975.

- [14] Mangler, “Induced Drag analysis in small aspect ratios”, Yearbook D.Lufo, p.I 139, 1939
- [15] Weinig, “Induced drag analysis in small aspect ratios”, Lufo, 405, 1936 and 434, 1937.
- [16] Pelletier, A. and Mueller, T.J., “Low Reynolds number aerodynamics of low-aspect-ratio, thin/flat/cambered-plate wings”, *J. of Aircraft*, Vol. 37, No.5, Sept.2000.
- [17] Torres, G. and Mueller, T.J. “Aerodynamic characteristics of low aspect ratio wings at low Reynolds number,” *Progress in Astronautics and Aeronautics*, (edited by Thomas J. Mueller), Vol. 195, pp. 115-141, 2001.
- [18] Johari, H. and Durgin, W.W. “Direct measurement of circulation using ultrasound,” *Experiments in Fluids*, Vol. 36, pp. 2195-2203, 1998.
- [19] Yuan, J. “Circulation methods in unsteady and three-dimensional flows”, Ph.D. Thesis, Worcester Polytechnic Institute, 2002.
- [20] Desabrais, K.J. and Johari, H. “Direct circulation measurements of a tip vortex,” *AIAA Journal*, Vol. 38, pp. 2189-2191, 2000.
- [21] Drovetski, S. “Influence of the trailing-edge notch on flight performance of galliforms,” *The Auk*, Vol. 113, pp. 802-810, 1996
- [22] Popp, K. “Experimental investigation of Reynolds number and scale effects on parachute inflation”, M.S. Thesis, Worcester Polytechnic Institute, 2000.
- [23] Cimbala et. al. “Importance of fresh air in manometer tubing”, *AIAA Journal*, Vol. 30, No. 1, pp 279-280, 1992.
- [24] White, F. M. Fluid Mechanics, McGraw Hill, 2003
- [25] Anderson, J. D, Jr., Fundamentals of Aerodynamics, McGraw Hill, 2001
- [26] Glauert, H., The Elements of Airfoil and Airscrew Theory, The University Press, 1948
- [27] Katz, J. and Plotkin, A., Low Speed Aerodynamics, from Wing Theory to Panel Methods, McGraw Hill, 1991,pp 524-527.

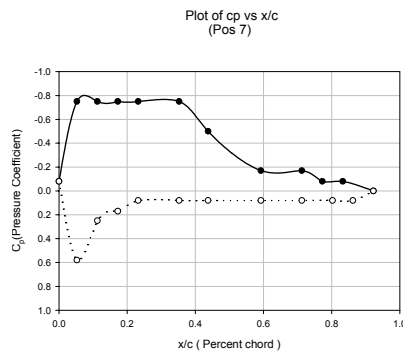
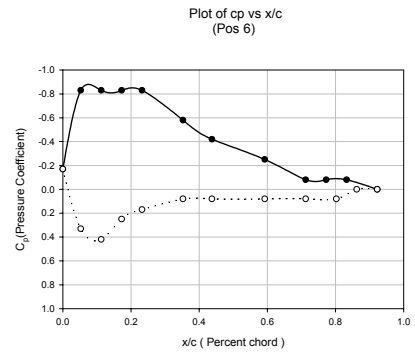
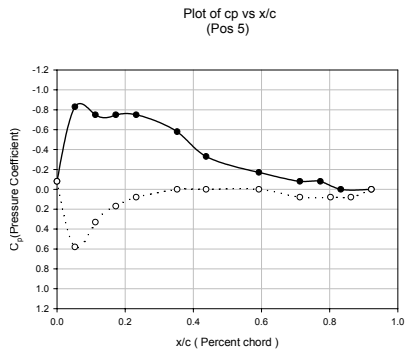
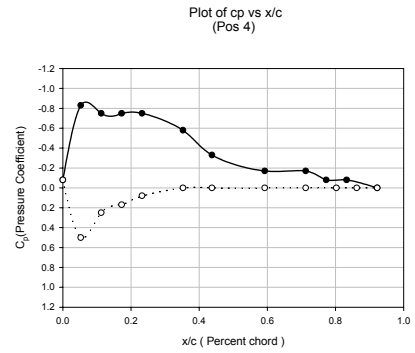
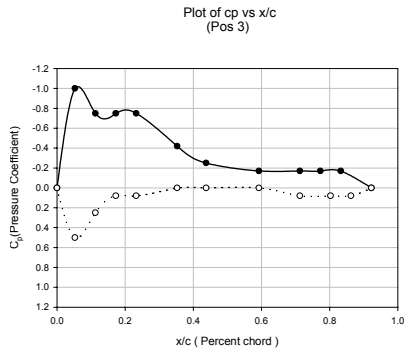
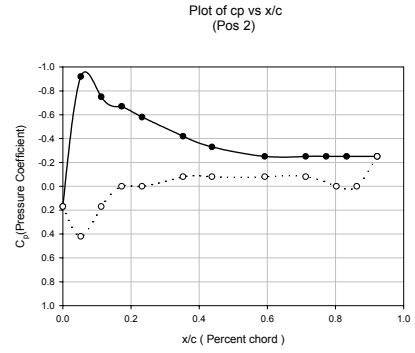
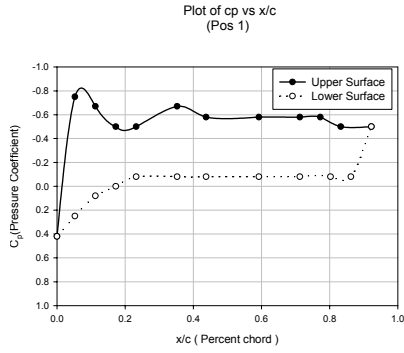
APPENDIX A



Plots for $Re = 30218$, $\alpha = 0^\circ$

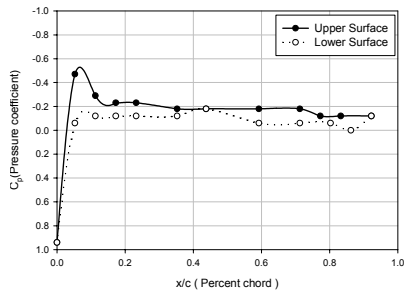


Plots for $Re = 30218$, $\alpha = 6^\circ$

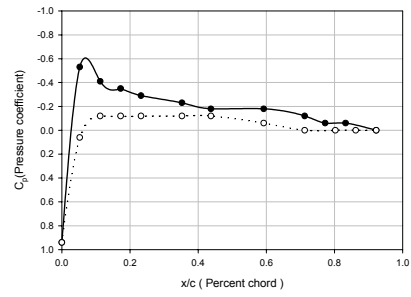


Plots for $Re = 30218$, $\alpha = 15^\circ$

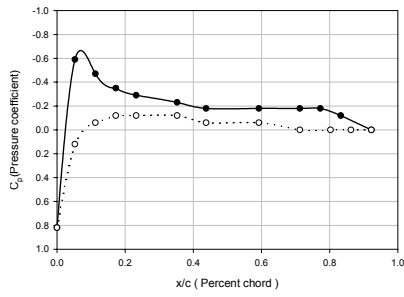
Plot of c_p vs x/c
(Pos 1)



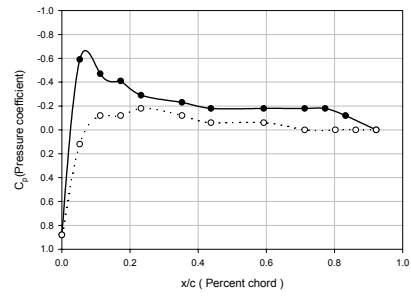
Plot of c_p vs x/c
(Pos 2)



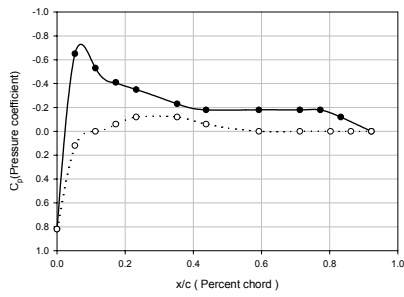
Plot of c_p vs x/c
(Pos 3)



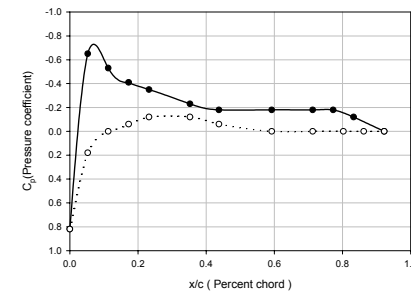
Plot of c_p vs x/c
(Pos 4)



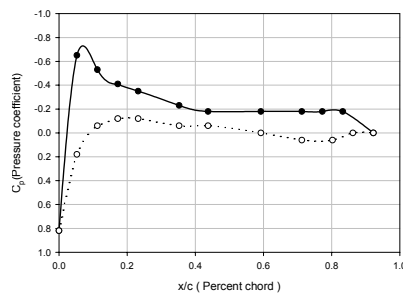
Plot of c_p vs x/c
(Pos 5)



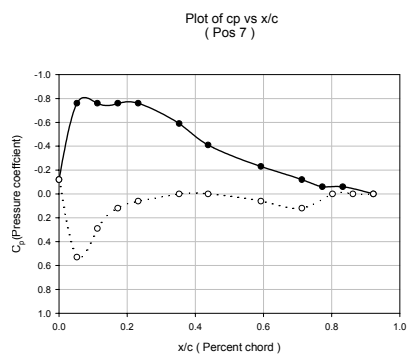
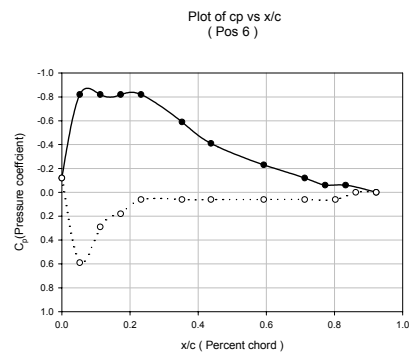
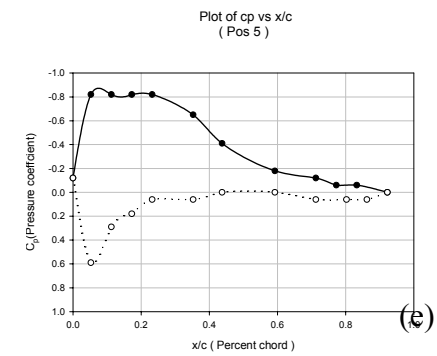
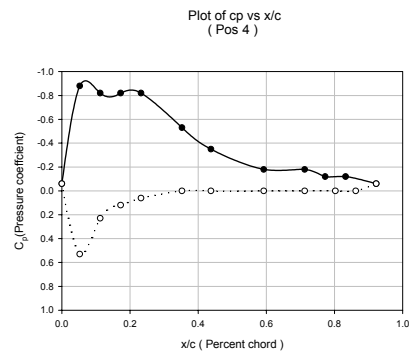
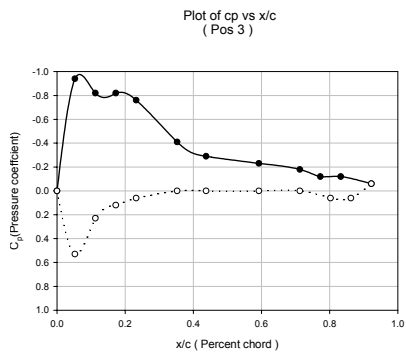
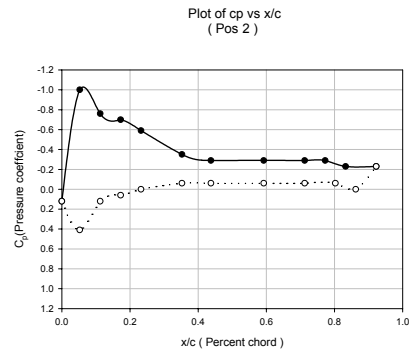
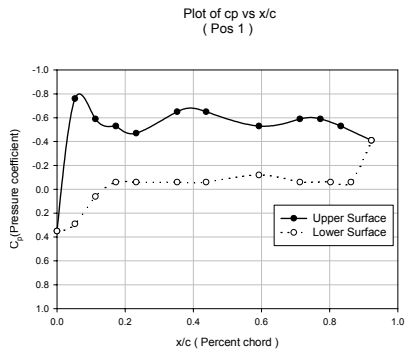
Plot of c_p vs x/c
(Pos 6)



Plot of c_p vs x/c
(At $Re = 30000$, $\alpha = 6^\circ$, Pos 7)

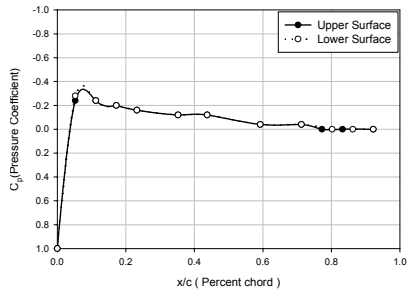


Plots for $Re = 35966$, $\alpha = 6^\circ$

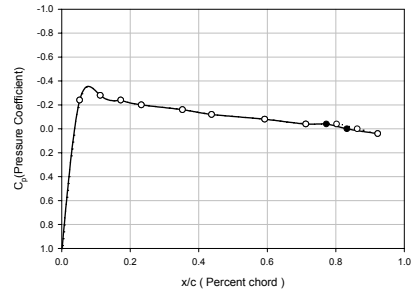


Plots for $Re = 35966$, $\alpha = 15^\circ$

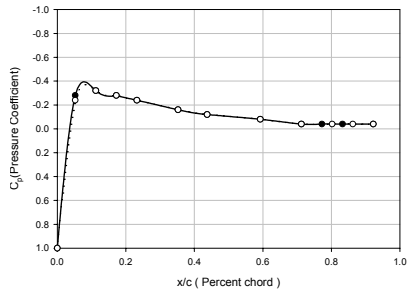
Plot of cp vs x/c
(Pos 1)



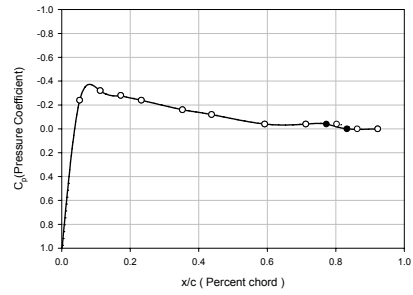
Plot of cp vs x/c
(Pos 2)



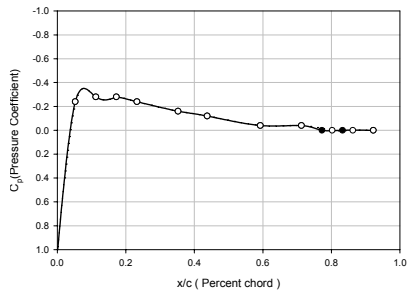
Plot of cp vs x/c
(Pos 3)



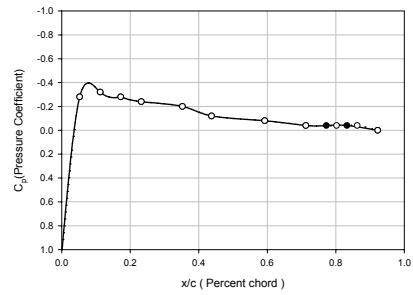
Plot of cp vs x/c
(Pos 4)



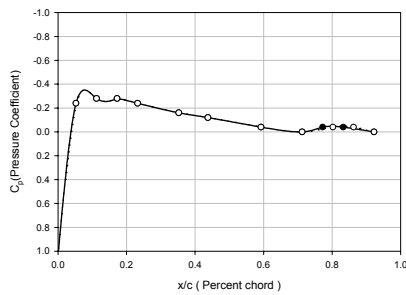
Plot of cp vs x/c
(Pos 5)



Plot of cp vs x/c
(Pos 6)

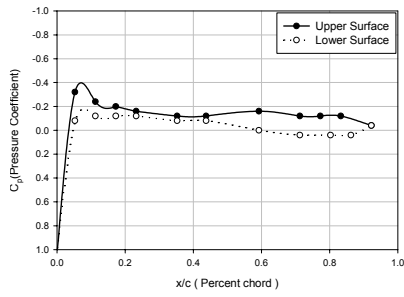


Plot of cp vs x/c
(Pos 7)

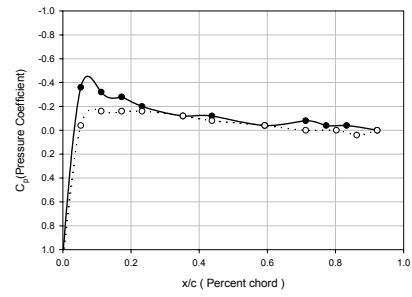


Plots for $Re = 43615$, $\alpha = 0^\circ$

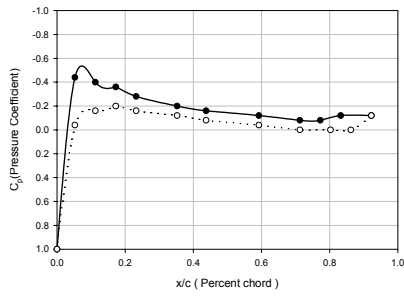
Plot of c_p vs x/c
(Pos 1)



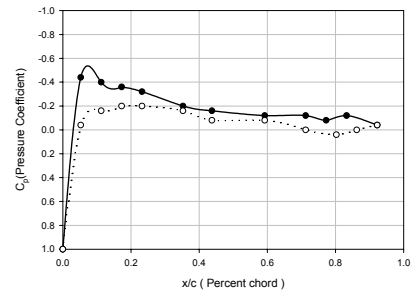
Plot of c_p vs x/c
(Pos 2)



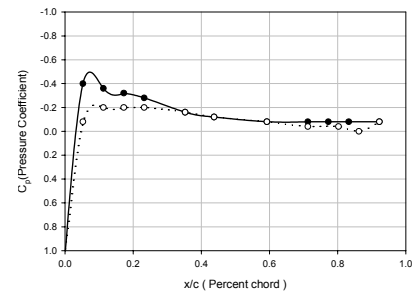
Plot of c_p vs x/c
(Pos 3)



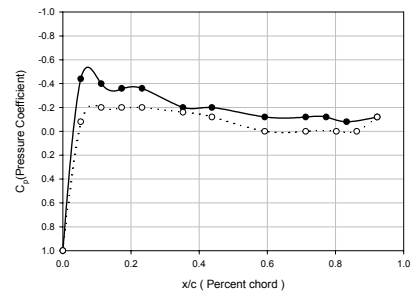
Plot of c_p vs x/c
(Pos 4)



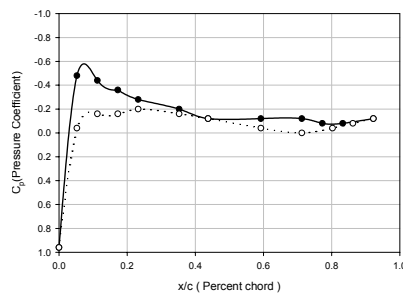
Plot of c_p vs x/c
(Pos 5)



Plot of c_p vs x/c
(Pos 6)

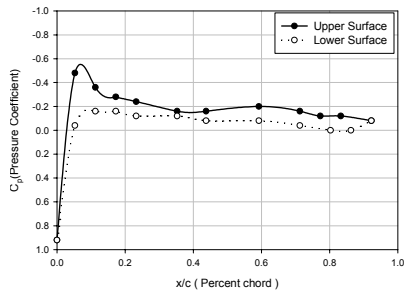


Plot of c_p vs x/c
(Pos 7)

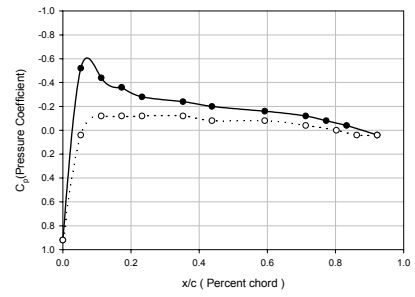


Plots for $Re = 43615$, $\alpha = 3^\circ$

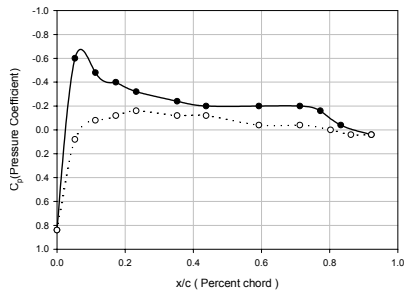
Plot of cp vs x/c
(Pos 1)



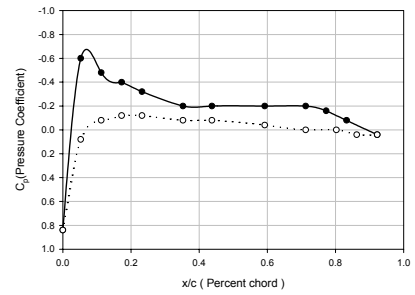
Plot of cp vs x/c
(Pos 2)



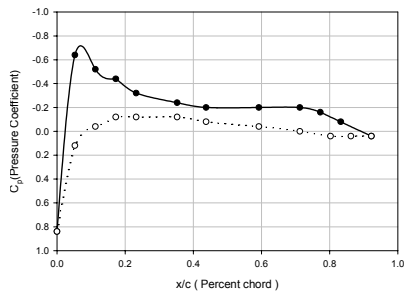
Plot of cp vs x/c
(Pos 3)



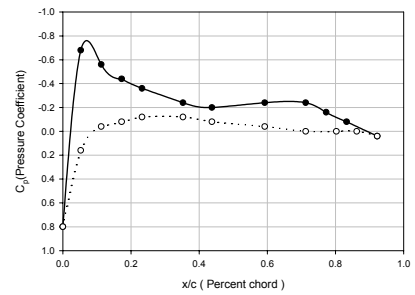
Plot of cp vs x/c
(Pos 4)



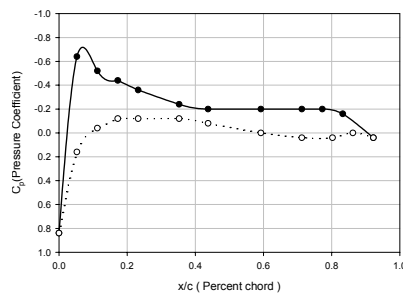
Plot of cp vs x/c
(Pos 5)



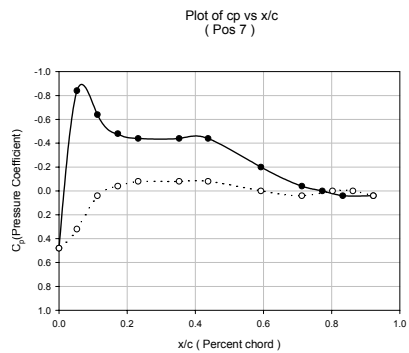
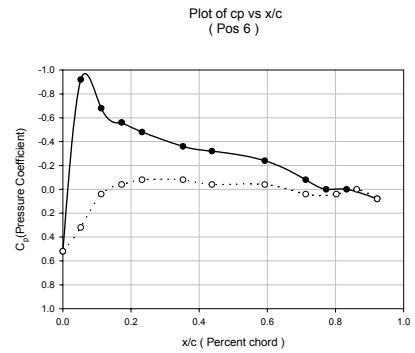
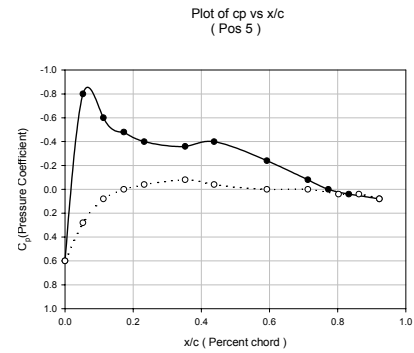
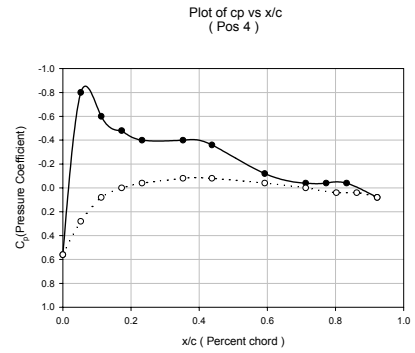
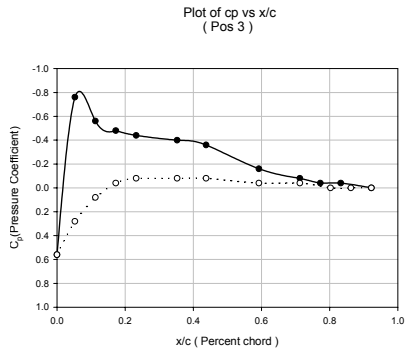
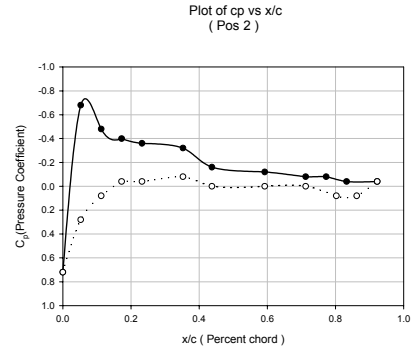
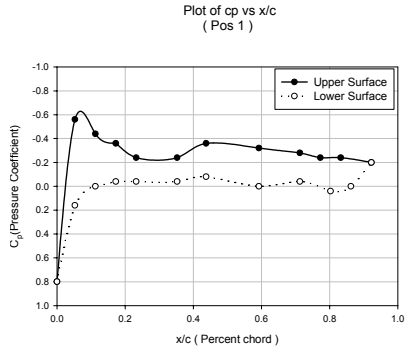
Plot of cp vs x/c
(At Re = 36000, alpha 6 , Pos 6)



Plot of cp vs x/c
(Pos 7)

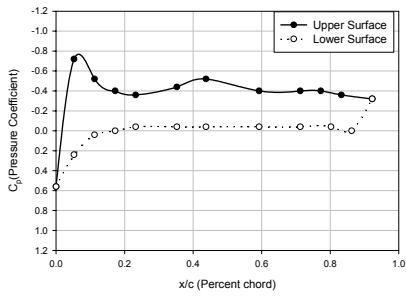


Plots for $Re = 43615$, $\alpha = 6^\circ$

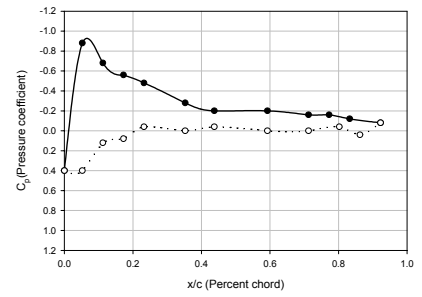


Plots for $Re = 43615$, $\alpha = 9^\circ$

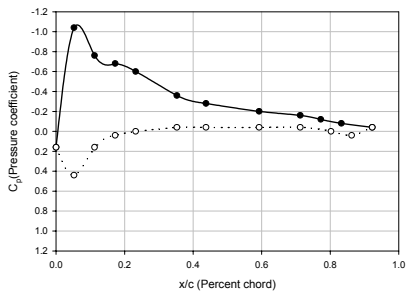
Plot of c_p vs x/c
(Pos 1)



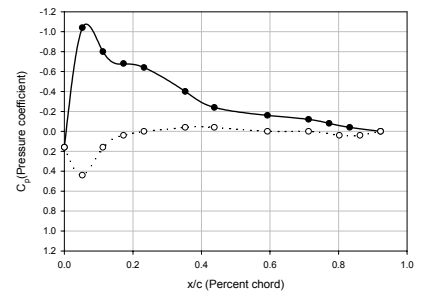
Plot of c_p vs x/c
(Pos 2)



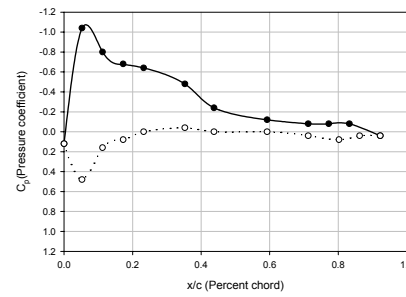
Plot of c_p vs x/c
(Pos 3)



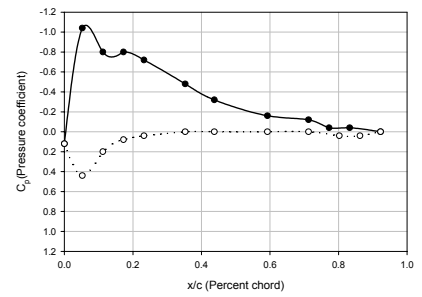
Plot of c_p vs x/c
(Pos 4)



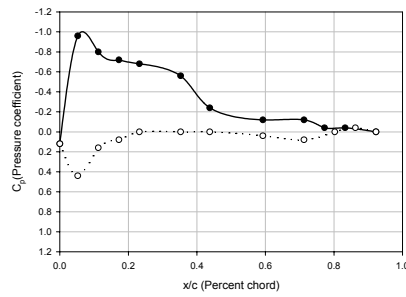
Plot of c_p vs x/c
(Pos 5)



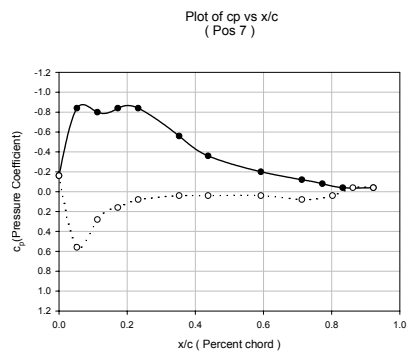
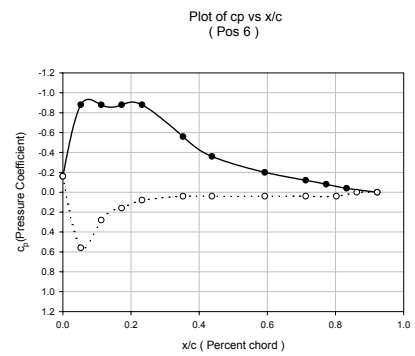
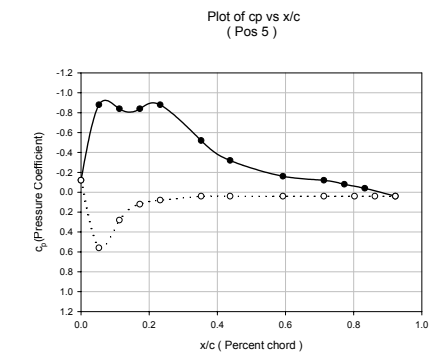
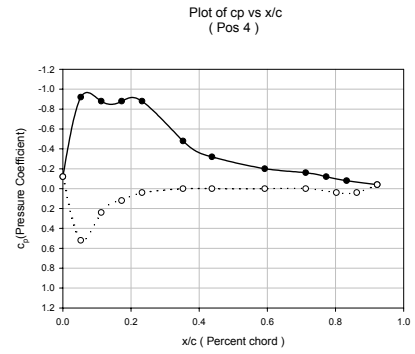
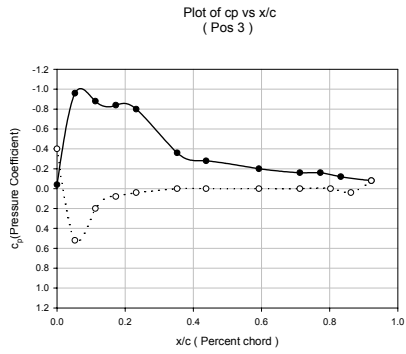
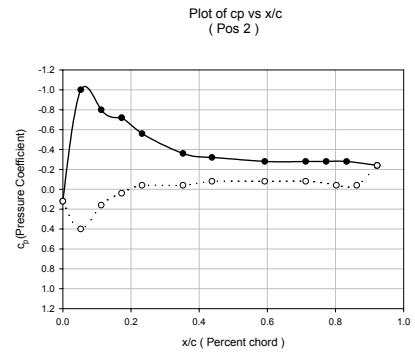
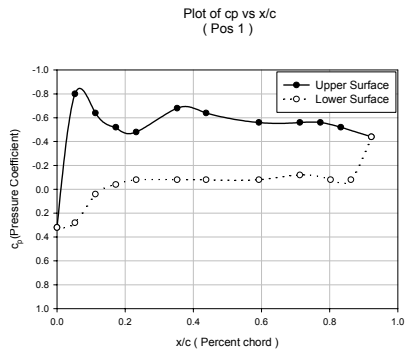
Plot of c_p vs x/c
(Pos 6)



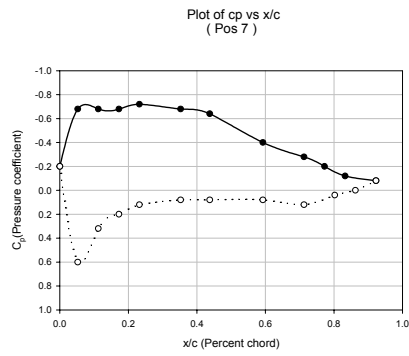
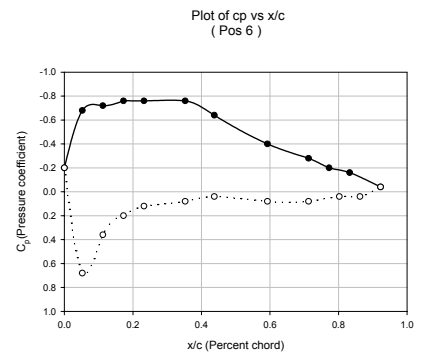
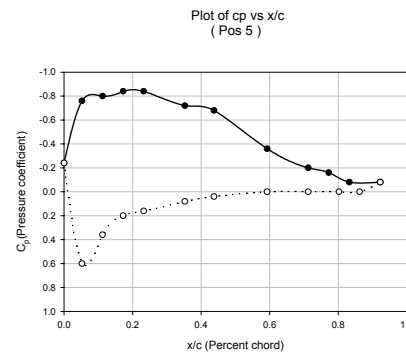
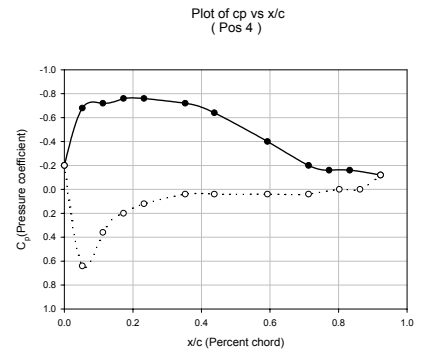
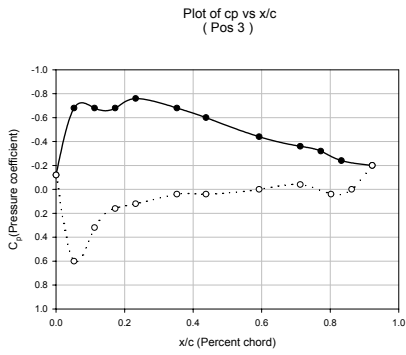
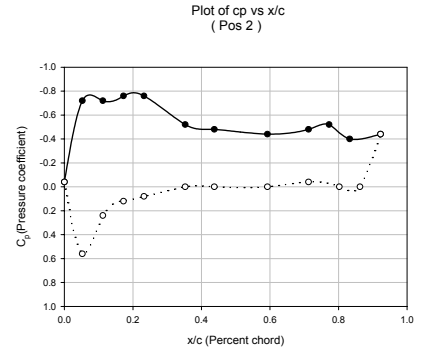
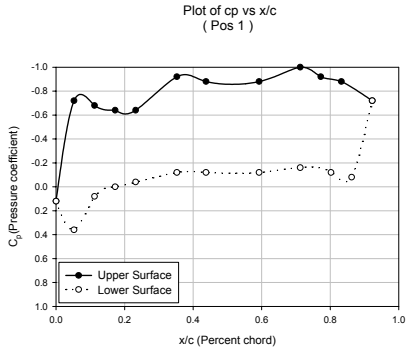
Plot of c_p vs x/c
(Pos 7)



Plots for $Re = 43615$, $\alpha = 12^\circ$

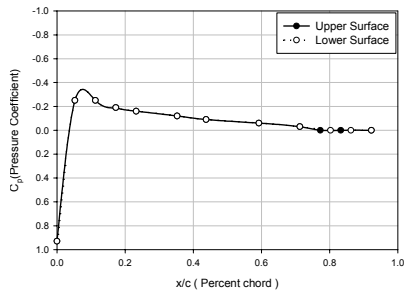


Plots for $Re = 43615, \alpha = 15^\circ$

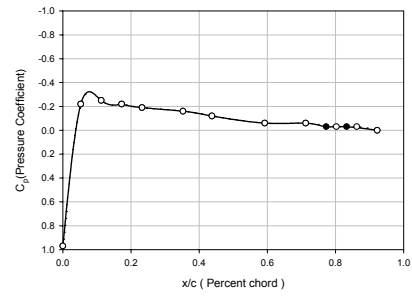


Plots for $Re = 43615$, $\alpha = 18^\circ$

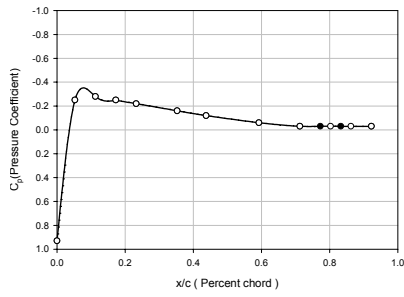
Plot of cp vs x/c
(Pos 1)



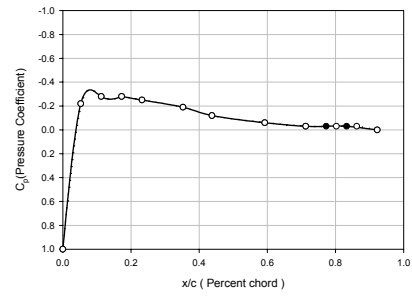
Plot of cp vs x/c
(Pos 2)



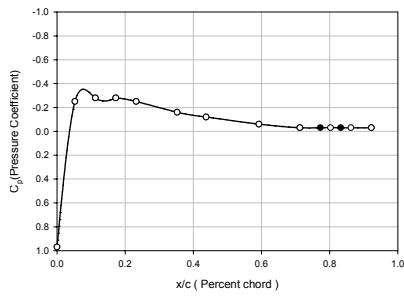
Plot of cp vs x/c
(Pos 3)



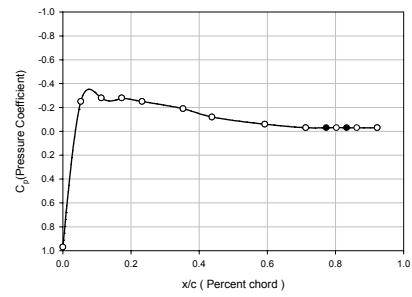
Plot of cp vs x/c
(Pos 4)



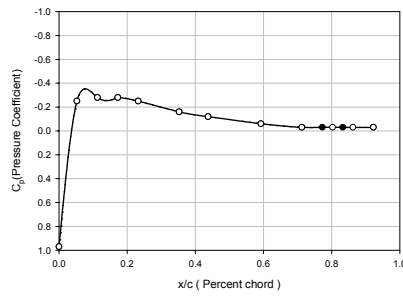
Plot of cp vs x/c
(Pos 5)



Plot of cp vs x/c
(Pos 6)

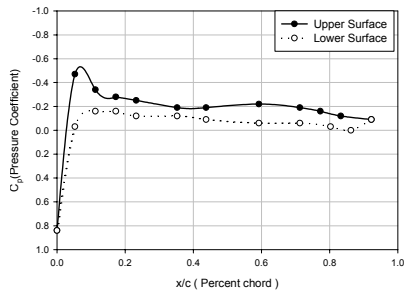


Plot of cp vs x/c
(Pos 7)

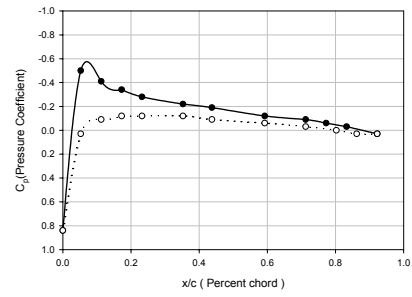


Plots for $Re = 49345$, $\alpha = 0^\circ$

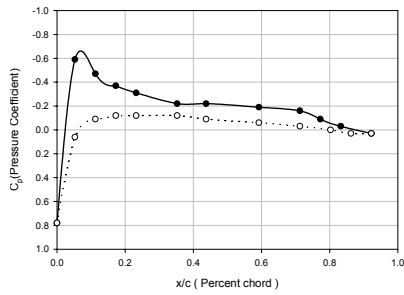
Plot of c_p vs x/c
(Pos 1)



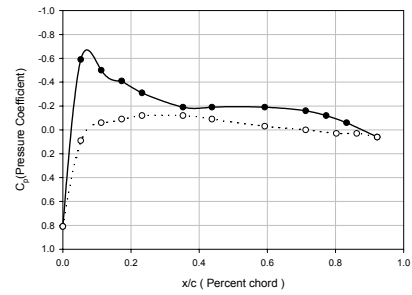
Plot of c_p vs x/c
(Pos 2)



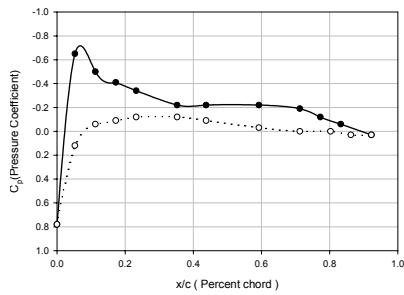
Plot of c_p vs x/c
(Pos 3)



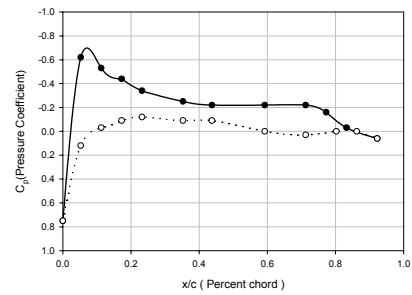
Plot of c_p vs x/c
(Pos 4)



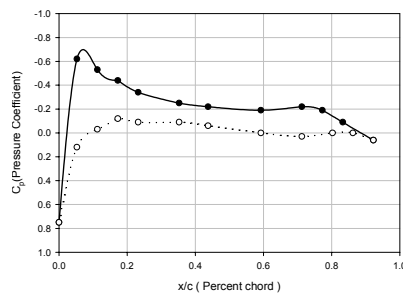
Plot of c_p vs x/c
(Pos 5)



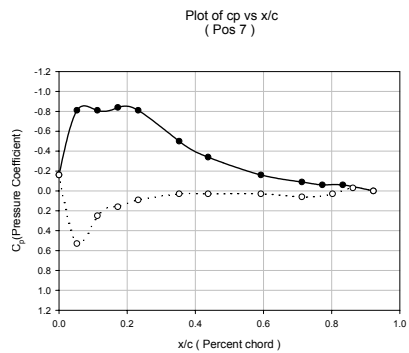
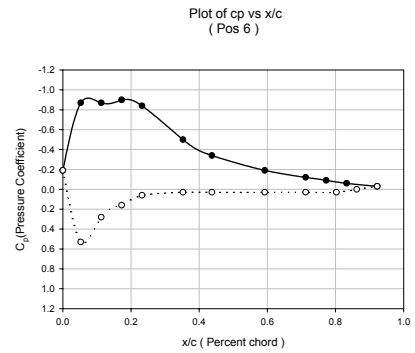
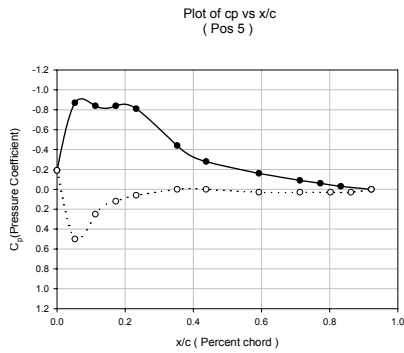
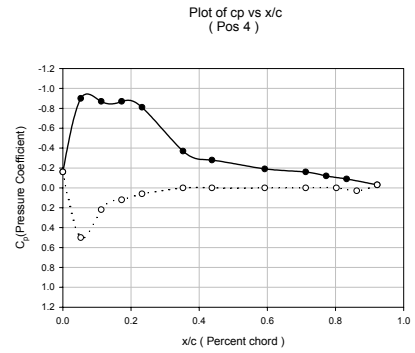
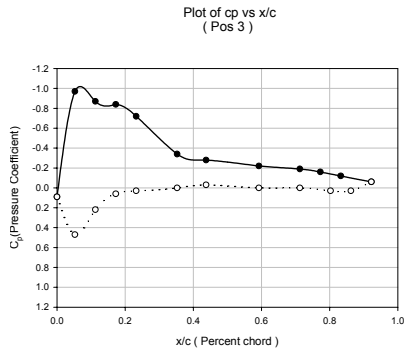
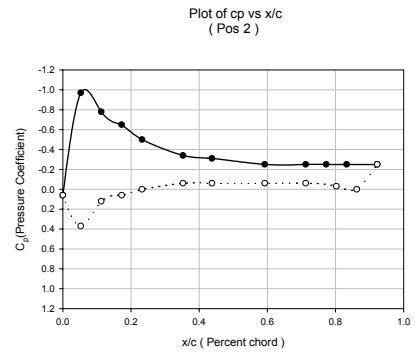
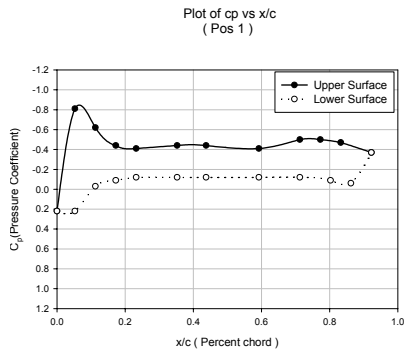
Plot of c_p vs x/c
(Pos 6)



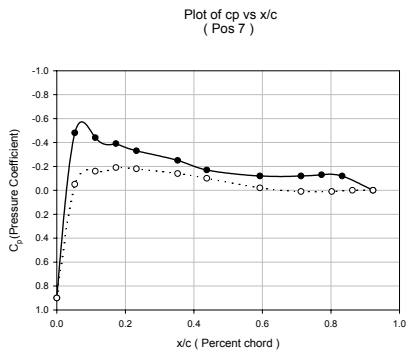
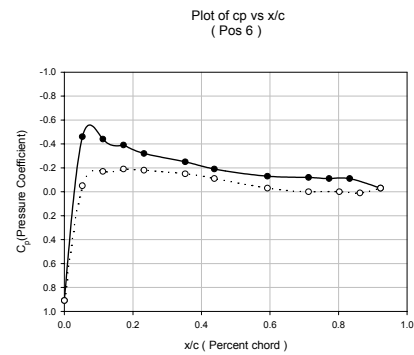
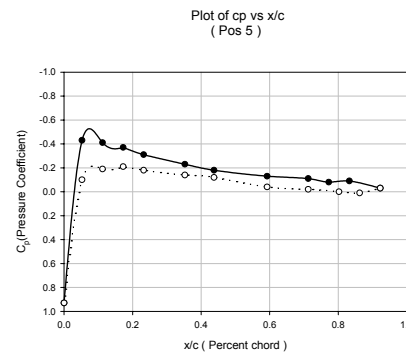
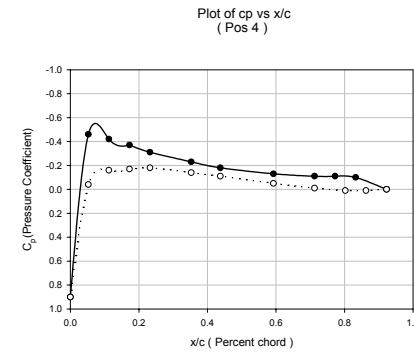
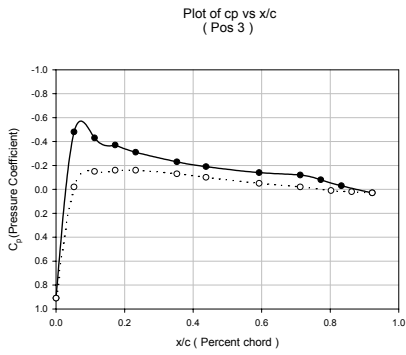
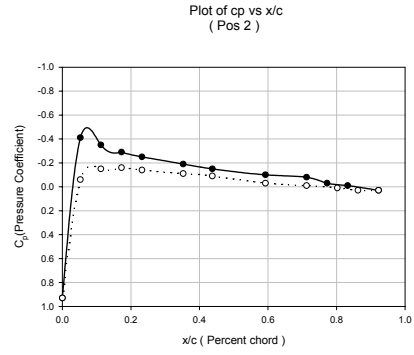
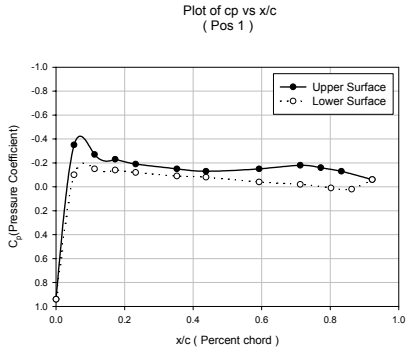
Plot of c_p vs x/c
(Pos 7)



Plots for $Re = 49345$, $\alpha = 6^\circ$

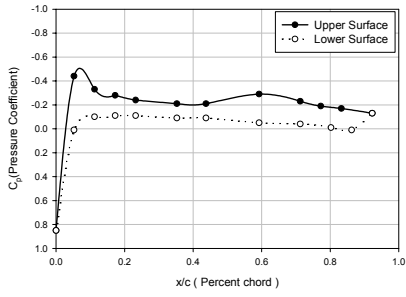


Plots for $Re = 49345$, $\alpha = 15^\circ$

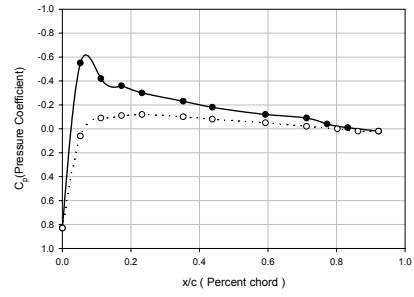


Plots for $Re = 84122$, $\alpha = 3^\circ$

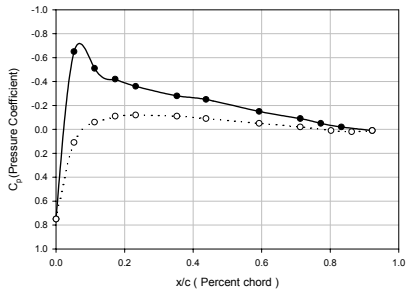
Plot of cp vs x/c
(Pos 1)



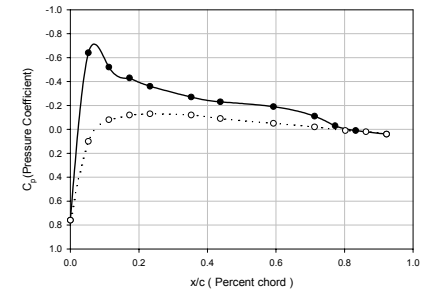
Plot of cp vs x/c
(Pos 2)



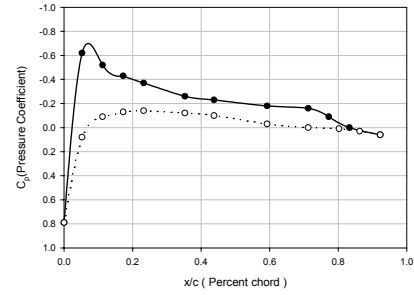
Plot of cp vs x/c
(Pos 3)



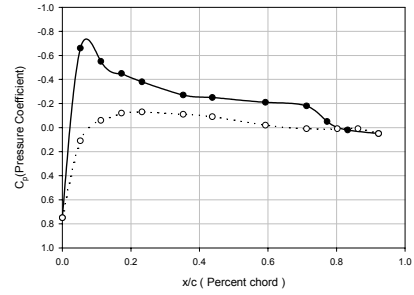
Plot of cp vs x/c
(Pos 4)



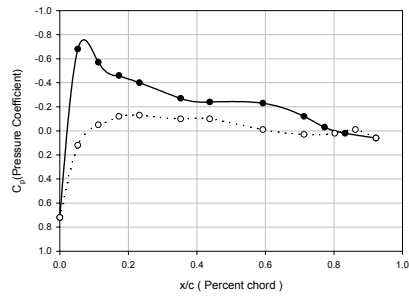
Plot of cp vs x/c
(Pos 5)



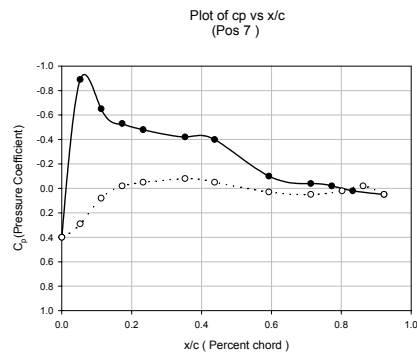
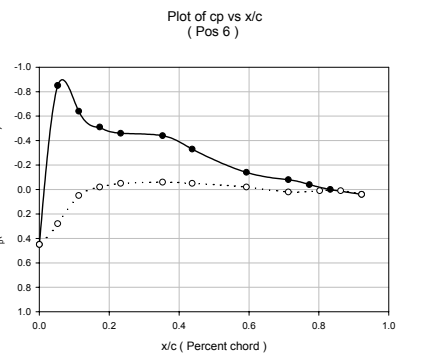
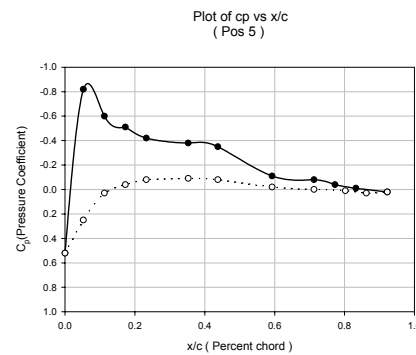
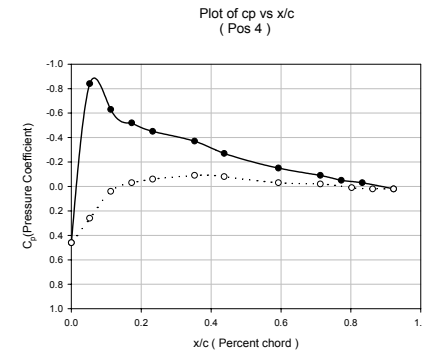
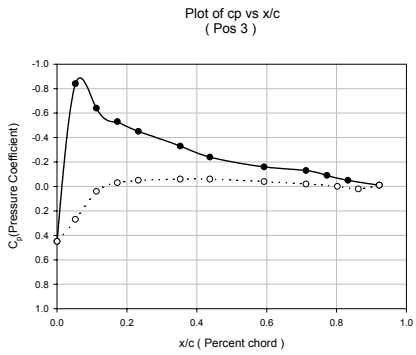
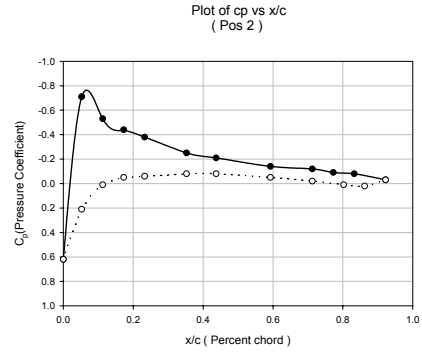
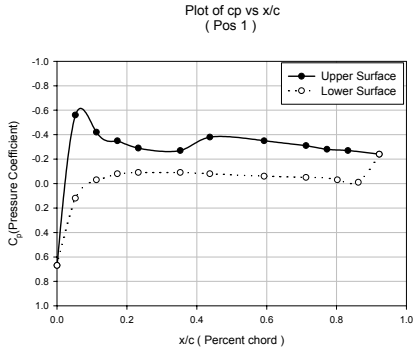
Plot of cp vs x/c
(Pos 6)



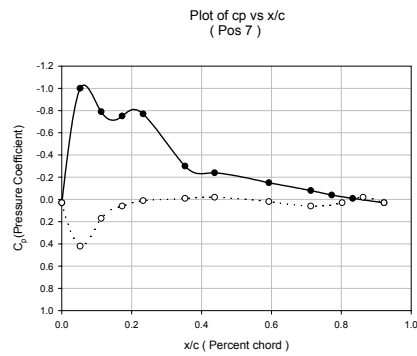
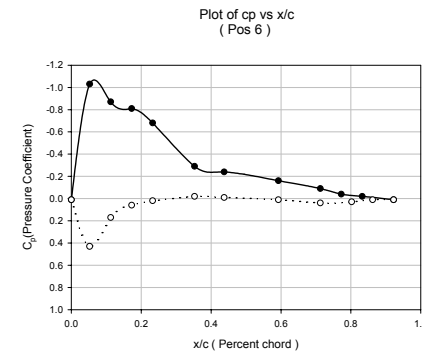
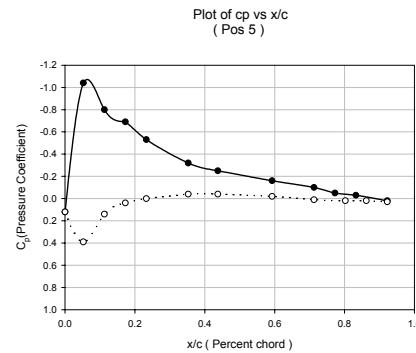
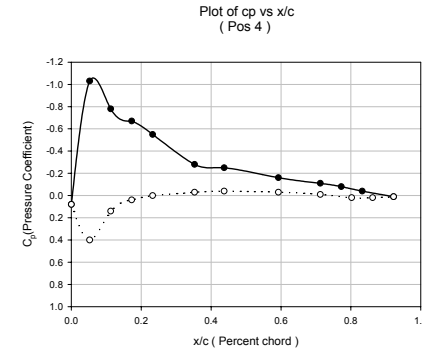
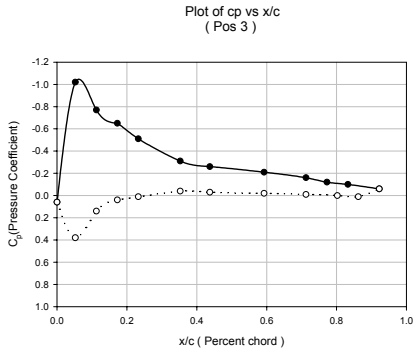
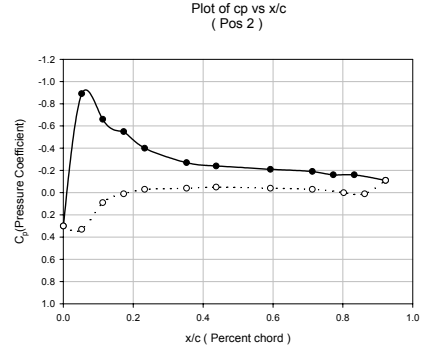
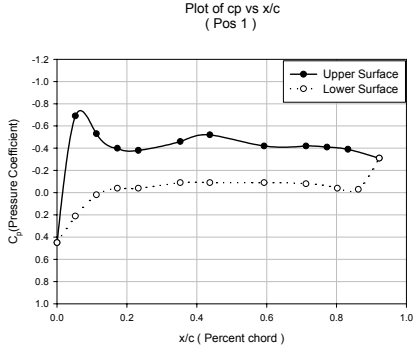
Plot of cp vs x/c
(Pos 7)



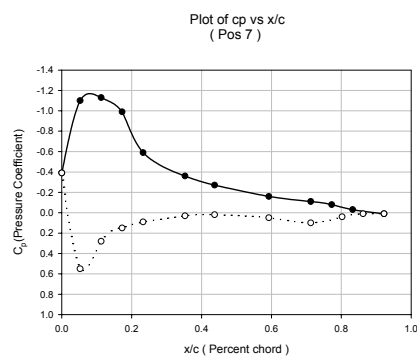
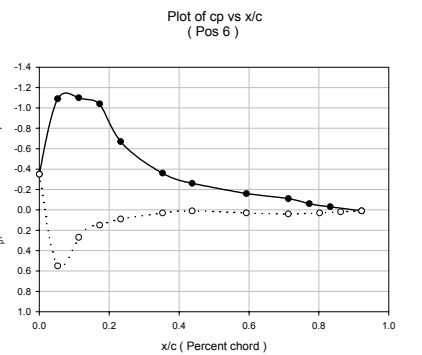
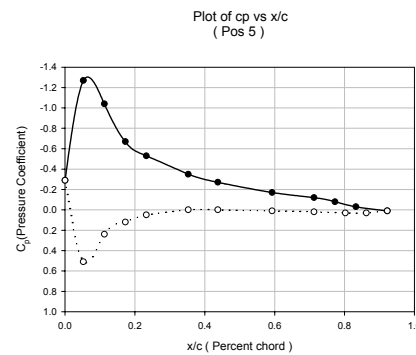
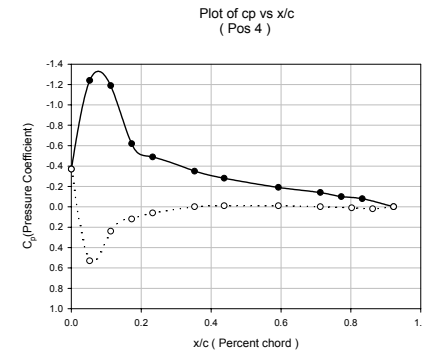
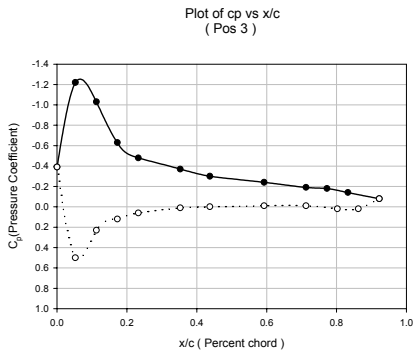
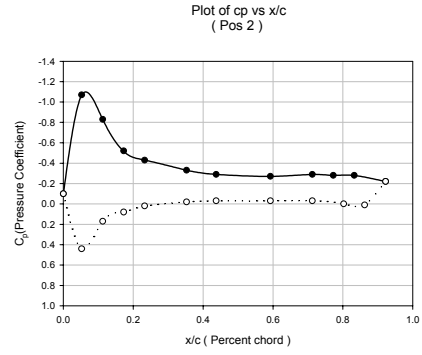
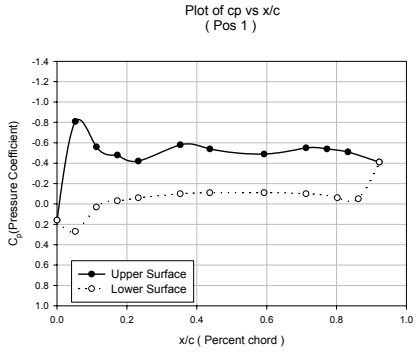
Plots for $Re = 84122$, $\alpha = 6^\circ$



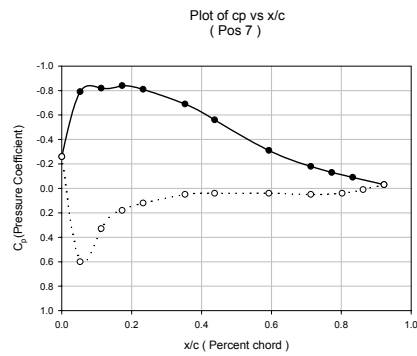
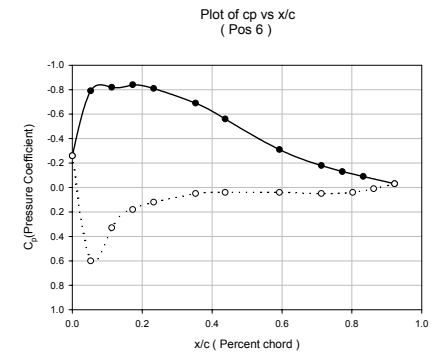
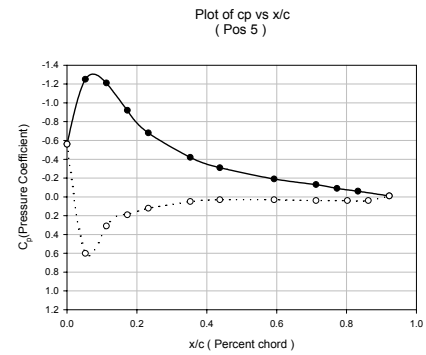
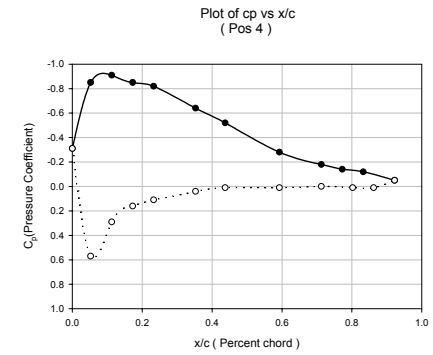
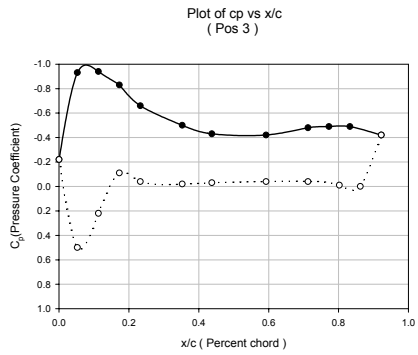
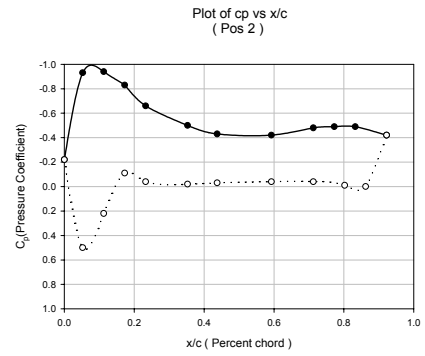
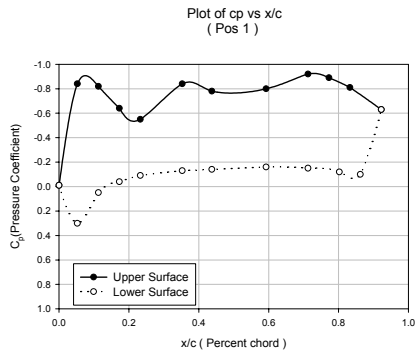
Plots for $Re = 84122$, $\alpha = 9^\circ$



Plots for $Re = 84122$, $\alpha = 12^\circ$



Plots for $Re = 84122$, $\alpha = 15^\circ$



Plots for $Re = 84122$, $\alpha = 18^\circ$

APPENDIX B

MATLAB CODES

%Program to calculate local lift coefficient by integrating cp vs x/c curve%

```

clear all;
clc;
clf;
h=0.0001;% X co-ordinate resolution
n=(0.9225/h)+1;% Range of matrices
s=1;% Maximum range of y co ordinate, where x axes has to be shifted
cpu= input('Enter the upper cp matrix')% Cp Data for upper surface
cpl= input('Enter the lower cp matrix')% Cp Data for lower surface
xu=[0.0,0.0525,0.1125,0.1725,0.2325,0.3525,0.4375,0.5925,0.7125,0.7725,0.8325,
0.9225];% x/c co-ordinates for upper surface
xl=[0.0,0.0525,0.1125,0.1725,0.2325,0.3525,0.4375,0.5925,0.7125,0.8025,0.8625,
0.9225];% x/c co-ordinates for lower surface
X=[0:h:0.9225];% Spline for x co ordinate
YU=spline(xu,cpu,X);% Spline for upper surface
YL=spline(xl,cpl,X);% Spline for lower surface
plot(X,YU,X,YL)% To plot cp vs x/c curve
YU1=s+YU;
YL1=s+YL;
% Calculation of Coefficient of Lift by integrating Cp vs x/c
%%%%%%%%%%%%%%%%%%%%%%%%%%%%%%%%%%%%%%%%%%%%%%%%%%%%%%%%%%%%%%%%%%%%%%%%
intsec(1)=X(1);
j=2;
for i=2:n-1;
    if (YU1(i)>YL1(i) & YL1(i+1)>YU1(i+1)) | (YU1(i)==YL1(i)) | (YU1(i)<YL1(i) &
YL1(i+1)<YU1(i+1))
        intsec(j)=X(i);
        j=j+1;
    end
end
r=j;
intsec(r)=X(n);
for j=1:r-1
    k=j;
    X1=[intsec(j):h:intsec(j+1)];
    YU2=spline(xu,cpu,X1);
    YL2=spline(xl,cpl,X1);
    area1(k)=trapz(X1,YU2);%area integral- upper surface
    area2(k)=trapz(X1,YL2);%area integral- lower surface
    area3(k)=(area1(k)-area2(k));
    j=j+1;
end
cl=sum(area3)%Lift Coefficient

```

```

%Program to plot lift coefficient against percent wing span for measured data and elliptic distribution%
clear all;
clc;
clf;
h=0.001;% X co-ordinate accuracy
b1=(8*25.4)/1000;% Wing Span
b2=1;%normalised wing span
c=(8*25.4)/1000;% chord length
S=(64*((25.4/1000)^2));% Wing area
rho=1.2;%air density
x=[1,0.9375,0.8125,0.6875,0.5625,0.4375,0.3125,0.1875,0];% Z/(b/2) for the wing
cl= input('Enter the cl(coefficient of lift) matrix')% Cl Data
v= input('Enter the free stream velocity')% free stream velocity
X=[0:h:1];% Spline for x co ordinate
Y=spline(x,cl,X);% Spline for upper surface
plot(X,Y)% To plot cl vs Z/(b/2) curve
hold on;
area=trapz(X,Y);% To calculate the area under the curve, i.e. the total lift
ymax= (4*area/pi);%to calculate the maximum lift at the root
n=(1/h)+1;
b(1)=0;
y(1)=ymax;%Minor axis of the elliptical lift distribution
j=(1/h);
for i=2:n% To plot the elliptical lift distribution for the same amount of lift

    b(i)=(h*(i-1));
    y(i)=sqrt((ymax^2)*(1-(b(i)^2)));
    i=i+1;
end
for k=1:j% For getting the ratios of the two lift coefficients
    ch(k)=y(k)/Y(k);
    k=k+1;
end
xc(1)=0;
for r=2:j % x co-ordinate for the plot of ratios
    xc(r)=(r-1)*h;
    r=r+1;
end
plot(b,y)
hold off;
figure(2)
plot(xc,ch)
CL=area

```

```

%Program to Calculate the Fourier Coefficients and span efficiency factor based on the measured lift distribution and elliptic distribution%
clear all;
clc;
clf;
format short;
h=0.001;% X co-ordinate accuracy
x=[1,0.9375,0.8125,0.6875,0.5625,0.4375,0.3125,0.1875,0];% Z/(b/2) for the wing
cl= input('Enter the cl(coefficient of lift) matrix');% Cl Data
%v= input('Enter the free stream velocity')% free stream velocity
X=[0:h:1];% Spline for x co ordinate
Y=spline(x,cl,X);% Spline for upper surface
figure(1)
plot(X,Y)% To plot cl vs Z/(b/2) curve
hold on;
area=trapz(X,Y);% To calculate the area under the curve, i.e. the total lift
ymax= (4*area/pi);%to calculate the maximum lift at the root
CL=area
n=(1/h)+1;
j=(1/h);
for i=1:n% To plot the elliptical lift distribution for the same amount of lift
    b(i)=(h*(i-1));
    y(i)=sqrt((ymax^2)*(1-(b(i)^2)));
    b1(i)=-b(i);
    i=i+1;
end
plot(b,y)
hold off;
for k=1:j% For getting the ratios of the two lift coefficients
    ch(k)=y(k)/Y(k);
    xc(k)=(k-1)*h;
    k=k+1;
end
%%%%%%%%%%%%%%%%%%%%%%%%%%%%%%%%%%%%%%%%%%%%%%%%%%%%%%%%%%%%%%%%%%%%%%%%
nn=40;
for i=1:nn
    theta(i)=((i)/nn)*(pi/2);
end
for j=1:nn
    xx(j)=cos(theta(j));
end
for ii=1:nn
for jj=1:n
    if abs(b(jj)-xx(ii))<0.0005
        kk(ii)=jj;
    end
end
end
for i=1:length(kk)
    m=kk(i);
    gamma(i)=(1/4)*Y(m);
end
for p=1:length(kk)
    for s=1:length(kk)
        R(p,s)=sin((2*s-1)*theta(p));
    end
end
Aact=R\gamma';
Aact(1:3);
for i=1:length(kk)
    deltas1(i)=(2*i-1)*(((Aact(i)/Aact(1)))^2);
end

```

```

end
delta1=sum(deltas1);
eact=(delta1)^(-1)
%%%%%%%%%For elliptic distribution
for i=1:length(kk)
    m=kk(i);
    gamma2(i)=(1/4)*y(m);
end
Aellip=R\gamma2';
Aellip(1:3);
for i=1:length(kk)
    deltas2(i)=(2*i-1)*((Aellip(i)/Aellip(1))^2);
end
delta2=sum(deltas2);
eellip=(delta2)^(-1)

```

APPENDIX C

For $\alpha = 15^\circ$

An	Re = 30218	Re = 35966	Re = 43615	Re = 49345	Re = 84122
A1	0.1437	0.1363	0.1413	0.1293	0.1292
A2	0.0323	0.0355	0.0358	0.0273	0.0339
A3	0.0232	0.0163	0.0194	0.0093	0.0165
A4	0.0061	0.0091	0.0086	0.0025	0.0018
A5	-0.0054	-0.0067	-0.0059	-0.005	-0.005
A6	-0.0082	-0.009	-0.011	-0.0054	-0.0074
A7	-0.0116	-0.0085	-0.0088	-0.0071	-0.0079
A8	-0.0008	-0.002	-0.0009	-0.0002	-0.0005
A9	0.0028	0.0027	0.0019	0.0015	0.0014
A10	-0.0013	-0.0008	-0.0008	-0.0013	-0.0008
A11	-0.001	-0.0013	-0.0012	-0.0001	-0.0008
A12	-0.0011	-0.0008	-0.0008	-0.001	-0.0007
A13	0.0004	0.0004	0.0002	0.0003	0.0002
A14	-0.0001	-0.0002	0	-0.0001	0
A15	0	0.0001	0	0.0001	0
A16	-0.0002	-0.0002	-0.0001	-0.0002	-0.0001
A17	0.0001	0.0001	0	0.0002	0
A18	-0.0002	-0.0002	-0.0001	-0.0003	-0.0001
A19	0.0002	0.0001	0.0001	0.0002	0.0001
A20	-0.0002	-0.0002	-0.0001	-0.0002	-0.0001
A21	0	0	0	0.0001	0
A22	-0.0003	-0.0003	-0.0002	-0.0002	-0.0002
A23	0	0	-0.0001	0	-0.0001
A24	-0.0001	-0.0001	-0.0001	-0.0001	-0.0001
A25	0.0001	0.0001	0	0.0001	0
A26	-0.0001	-0.0001	-0.0001	-0.0001	-0.0001
A27	0.0001	0.0001	0	0.0001	0
A28	0	-0.0001	0	-0.0001	0
A29	0.0002	0.0002	0.0001	0.0002	0.0001
A30	0	0	0.0001	0	0
A31	0.0002	0.0001	0.0001	0.0002	0.0001
A32	0	0	0	-0.0001	0
A33	0.0001	0.0001	0	0.0001	0
A34	-0.0001	-0.0001	0	-0.0001	0
A35	0.0001	0.0001	0.0001	0.0001	0.0001
A36	0	0	0	-0.0001	0
A37	0.0001	0.0001	0.0001	0.0001	0.0001
A38	0	0	0	-0.0001	0
A39	0.0001	0.0001	0	0.0001	0
A40	-0.0001	-0.0001	0	-0.0001	0

For $\alpha = 6^\circ$

An	Re = 30218	Re = 35966	Re = 43615	Re = 49345	Re = 84122
A1	0.0586	0.0583	0.0582	0.0567	0.0569
A2	0.0042	0.0018	0.0036	0.0036	0.0098
A3	0.0023	0.0024	0.003	0.0045	0.0069
A4	0.002	-0.0014	0.0006	0.0018	0.0023
A5	-0.0024	-0.0012	-0.0016	-0.0012	-0.0009
A6	-0.0034	-0.0009	-0.0019	-0.0026	-0.0031
A7	0.0002	-0.0011	-0.002	-0.0024	-0.0044
A8	-0.0011	-0.0013	-0.0001	-0.0005	-0.0004
A9	0	0.0006	0.0003	0.0006	0.0011
A10	0.0006	0.0006	-0.0002	0	-0.0003
A11	-0.001	-0.0011	-0.0002	-0.0006	-0.0006
A12	0.0003	0.0003	-0.0002	-0.0001	-0.0003
A13	-0.0001	0	0	0	0.0001
A14	0	0	0	0	0
A15	0	-0.0001	0	0	0
A16	0.0001	0.0001	0	0	0
A17	-0.0001	-0.0001	0	-0.0001	0
A18	0.0001	0.0001	0	0	-0.0001
A19	-0.0001	-0.0001	0	0	0
A20	0.0001	0.0001	0	0	0
A21	-0.0001	-0.0001	0	0	0
A22	0	0	0	0	-0.0001
A23	-0.0001	-0.0001	0	0	0
A24	0	0	0	0	0
A25	-0.0001	-0.0001	0	0	0
A26	0.0001	0.0001	0	0	0
A27	-0.0001	-0.0001	0	0	0
A28	0.0001	0.0001	0	0	0
A29	0	0	0	0	0
A30	0.0001	0.0001	0	0	0
A31	0	0	0	0	0
A32	0.0001	0.0001	0	0	0
A33	0	0	0	0	0
A34	0	0	0	0	0
A35	0	0	0	0	0
A36	0	0	0	0	0
A37	0	0	0	0	0
A38	0.0001	0.0001	0	0	0
A39	0	0	0	0	0
A40	0	0	0	0	0

APPENDIX D

Sample error calculations:

The error calculation in the pressure coefficients is based on RSS (Root sum of squares) type uncertainty. A sample calculation and a sample table for errors in pressure coefficient for $Re = 30218$ and $\alpha = 15^\circ$ is shown here.

Error in Pressure coefficient:

For a specific pressure coefficient, C_p and a dynamic pressure, q we have

$$C_p = \frac{\Delta P}{q}$$

where $\Delta P = P - P_s$

where P = pressure being measured (upper or lower surface pressure)

P_s = static pressure

q = dynamic pressure

$$\delta C_p = \sqrt{\left(\left(\frac{\partial C_p}{\partial (\Delta P)} \right) \cdot \delta(\Delta P) \right)^2 + \left(\left(\frac{\partial C_p}{\partial (q)} \right) \cdot \delta(q) \right)^2}$$

Here $\delta(\Delta P) = \delta(q) = 0.0005$, which is the accuracy of pressure transducer. The table on following page demonstrates a sample set of error calculated in pressure coefficients.

So for a particular pressure measurement we can obtain the error in pressure coefficient.

The error in pressure coefficient calculation introduces error in the local lift coefficient calculation. This was based on the RSS type uncertainty as well. The error in c_l is then given as:

$$\delta c_l = \sum (\delta C_{pu} - \delta C_{pl})$$

So by knowing the error in C_p we can obtain the error in local lift coefficient. The code for this calculation was done in MATLAB.

Error in pressure coefficients for $Re = 30218$ and $\alpha = 15^\circ$:

Error calculation in pressure coefficients					
Upper Surface			Lower Surface		
Port #	$C_{p,u}$	Error in C_{pu}	Port #	$C_{p,l}$	Error in C_{pl}
1	-0.08	0.042	1	-0.08	0.042
2	-0.75	0.052	13	0.58	0.048
3	-0.75	0.052	14	0.25	0.043
4	-0.75	0.052	15	0.17	0.042
5	-0.75	0.052	16	0.08	0.042
6	-0.75	0.052	17	0.08	0.042
7	-0.50	0.047	18	0.08	0.042
8	-0.17	0.042	19	0.08	0.042
9	-0.17	0.042	20	0.08	0.042
10	-0.08	0.042	21	0.08	0.042
11	-0.08	0.042	22	0.08	0.042
12	0.00	0.042	23	0.00	0.042